Novel Structures and Applications of Leaky Thin-Ridge Silicon Waveguides

A thesis submitted in fulfilment of the requirements for the degree of

Doctor of Philosophy

Kiplimo Yego

School of Electrical and Computer Engineering

College of Science, Engineering and Health

RMIT University

January 2016

To my loving wife Bianca and our son Dante.

Declaration

I certify that except where due acknowledgement has been made, the work is that of the author alone; the work has not been submitted previously, in whole or in part, to qualify for any other academic award; the content of the thesis/project is the result of work which has been carried out since the official commencement date of the approved research program; any editorial work, paid or unpaid, carried out by a third party is acknowledged; and, ethics procedures and guidelines have been followed.

Kiplimo Yego.
22^{nd} January 2016

Acknowledgements

Firstly, I would like to thank my supervisor Professor Arnan Mitchell for the trust you had in me while undertaking my PhD. Your wisdom, support and motivation over the years have guided me through the hardest and also most rewarding times of this research project. I will be forever grateful. I would also like to thank my second supervisor Dr. Thach Nguyen for, among many things, your continuous diligence and patience in attending to my persistent inquiries.

My dear wife Bianca. You deserve more than I could ever give for your support through this PhD journey that I undertook. Your unceasing support has been my pillar of strength and you deserve so much praise. Thank you for courageously bearing our son Dante in the midst of this hectic period and still remaining unwavering in your patience and support.

I would like to thank my father Joel Yego for starting me on this journey and instilling in me a desire for knowledge and teaching me its value. I thank my mother Joyce Yego for her prayers and encouragement as well as my siblings Kipchirchir, Jeanette and Volita.

To my friends and fellow students with whom we shared our common struggles, I say thank you. You deserve mention Shiva, Guanghui, Berrak, Andreas, Peter, Michael, Anthony, Geeth, Eike, Naser, Tristan, Mahyar and Philipp.

Last but not least I would also like to thank some academics, namely Associate Professor James Scott, Dr. Lam Bui and Professor Michael Austin, who spared some of their precious time during the course of my PhD to lend me their expertise.

Abstract

The ability to utilize signals at optical frequencies, as opposed to say microwave frequencies, provides much more bandwidth and signal transmission speed to meet the increasing telecommunication demands in today's world. The ability to integrate optical circuits in the same manner as in electronic integrated circuits means that optical devices can be miniaturized and can even complement today's complex electronic circuits and devices. Silicon nanophotonics is a highly attractive platform for emerging integrated optical solutions in areas including optical signal transmission, signal processing, optical sensing and optical computing. This is primarily because the silicon platform is compatible with CMOS fabrication processes, which through significant investment have developed and matured over many years to serve the electronics industry. Transitioning into an optical platform that can exploit this vast electronics manufacturing industry is viable particularly for enabling low cost mass manufacturing of integrated photonic circuits. High refractive index contrast silicon waveguide platforms such as silicon-on-insulator (SOI) enable strong confinement of light in sub-micron waveguides as well as the sharp bending of waveguides with minimal loss. The SOI platform has therefore attracted research interest into the development of compact integrated silicon photonic circuits.

Thin-ridge SOI waveguides are particularly promising because they minimize signal transmission loss by significantly reducing the waveguide etch-depth and therefore reducing scattering losses due to sidewall roughness. However, a consequence of the reduced etch-depth is the possibility for TM guided modes to couple to highly coherent TE

radiation in the adjacent slab. This TM-TE coupling phenomenon, named lateral leakage radiation, is the subject of this thesis. The main aim of this thesis is to investigate the possible exploitation of this inherent coupling relationship between TM and TE polarizations. The novel structures presented herein could have potential applications which include optical biosensing, polarization rotation and resonant optical filtering.

The main contributions of this research work include first and foremost the discovery of a resonant coupling effect in thin-ridge waveguides when illuminated by TE slab beam. It is shown through simulation that a resonant TM mode in a thin-ridge waveguide is excited when a TE slab beam is incident upon it at a phase-matched angle of propagation. This resonance effect has a canonical Lorentzian response and the quality-factor can be controlled by adjusting the waveguide dimensions. It is also shown that several such resonator waveguides can be cascaded in a coupled resonator topology to realize higher order Chebyshev filter responses. Another contribution in this thesis is that a holographic-based grating structure exploiting the TM-TE coupling in thin-ridge waveguides can be used to efficiently convert a Gaussian TE slab beam into a collimated TM slab beam. It is shown that an apodized grating is the most suitable design for achieving this goal. Lastly, it is also shown through simulation that the lateral leakage effect can be utilized as a biosensor to measure refractive index changes at the surface of a thin-ridge waveguide caused by the deposition of biomolecules. A tapered thin-ridge waveguide in tandem with a planar lens structure is proposed as a potential sensor topology for evanescent field biosensing.

In summary, it has been shown that lateral leakage in thin ridge waveguides can be enhanced using unique waveguide structures and exploited for integrated optical applications.

Contents

List of Figures

Chapter 1

Introduction

Today, researchers are not only interested in finding new types of photonic devices but also ensuring that these devices can be integrated into photonic circuits on chips that will drive the next generation of opto-electronic technologies [1]. This requires the miniaturization of photonic devices for optical signal transmission and processing allowing compact integration of several photonic and electronic devices for advanced system functionality. Silicon has been identified as a promising platform for integrating photonic circuits primarily because this is the same platform that the electronics CMOS (complimentary metal oxide semiconductor) industry utilizes for manufacturing electronic circuits [2]. Since silicon is a CMOS compatible platform, it is envisioned that existing mature CMOS technologies can be harnessed for the mass manufacture of low cost but advanced opto-electronic circuits.

Photonic devices are comprised primarily of optical waveguides. Optical waveguides are the backbone of photonic circuits as they provide the conduits for optical signal transmission and processing. Several types of silicon optical waveguides exist exhibiting different traits that make them advantageous for various purposes. One example is the silicon-on-insulator (SOI) nanowire waveguide which is in the order of 450nm width by 260nm height [3]. It has been shown that the high index contrast of the SOI platform enables light to propagate around tight bends with minimal bending loss enabling the fabrication of densely integrated photonic circuits [2]. Another type of waveguide is the rib-waveguide. Although mode confinement is decreased compared to strip waveguides, they can

provide electrical access to the optical modes through the slab waveguide for example by doping the silicon. This technique has been utilized for example to design Raman lasers in silicon rib waveguides [4]. Another example is the slot waveguide which has proved useful due to the field enhancement in the slot region which has been exploited for example in non-linear optics [5] as well as for enhancing light-matter interactions [6]. A photonic crystal (PhC) waveguide is yet another type of waveguide introduced as a defect in a photonic crystal lattice. It can have extremely small sub-wavelength lateral dimensions [7]. Consequently extremely tight mode confinement can be obtained resulting in increased field intensities within the defect waveguide. This makes PhC waveguides useful for various applications including non-linear optics and optical sensing that benefit from enhanced light matter interactions [8]. Another recent addition to the family of waveguides is the coupled resonator optical waveguide (CROW) which is formed by coupling several optical resonators together such as ring resonators, disk resonators and even photonic crystal cavities [9]. Depending on the energy storage capacity of the resonators in a CROW, also known as the quality-factor, the optical field intensity in the resonators can increase dramatically and the propagation delay through the CROW can also rise. CROWS have been utilized for optical sensing, non-linear optics, delay lines, optical filtering and optical switching [9]. This list illustrates how each type of waveguide topology has unique characteristics that makes it advantageous for various applications over other types of waveguides.

Another recent type of waveguide is the silicon-on-insulator (SOI) thin-ridge waveguide. A thin-ridge waveguide is similar to a strip or rib waveguide except that the etch depth reached when fabricating the thin-ridge waveguide is very shallow in the order of 15nm for a 220nm thick silicon slab [10]. The design of thin-ridge waveguides was primarily motivated by the fact that fabrication of silicon waveguides in the current state of the art is not error-free. A major drawback of strip and rib waveguides, which are deeply etched, is that the sidewall roughness that occurs during fabrication leads to inaccuracies in the waveguide dimensions resulting in scattering losses [4]. One approach to tackling this problem has been to design integrated optical devices with tolerance to fabrication errors taken into account [11]. Thin-ridge SOI waveguides tackle this problem of

scattering loss by removing a significant portion of the waveguide walls that lead to the problem of sidewall roughness in the first place. This removes a significant portion of the scattering losses that can occur in thin-ridge waveguides thus decreasing the overall propagation losses for TE and TM guided modes in thin-ridge waveguides [12]. However, it was discovered that the propagation loss for the TM guided mode is strongly dependent on the waveguide dimensions and can vary significantly [10]. This loss phenomenon was identified as being caused by coupling from the guided TM mode to a highly coherent TE slab mode and it came to be referred to as lateral leakage radiation. Interestingly, very little work has been found that tries to exploit this lateral leakage radiation behaviour [13, 14]. It is believed that research opportunities could lie here and it could prove to be a worthwhile endeavour. The mechanisms that lead to this lateral leakage radiation will be described in the following background. This background is crucial since the core subject of this thesis is to explore ways of exploiting this lateral leakage radiation phenomenon for practical purposes.

1.1 Background of lateral leakage radiation in thin-ridge SOI waveguides

In 2007, Webster et. al. [10] characterized the propagation losses of a thin-ridge waveguide that was fabricated using a thermal oxidation process to enhance the smoothness of the side walls to reduce sidewall scattering losses. The waveguide core thickness was 205nm while the ridge height was only 15nm. Vertically, this waveguide structure only supports a single slab mode at a wavelength of 1550nm. The loss measurements that they obtained showed the transmission losses for the fundamental TE and TM modes as a function of the waveguide width. They observed low TE propagation losses of about 0.7dB/cm, which remained relatively steady across the changing waveguide widths. This was attributed to the decreased side-wall roughness that mitigates scattering losses. However, a peculiar phenomenon was observed in the TM mode propagation loss. It was observed that the TM propagation loss was significantly higher than that of the TE mode. However, at specific waveguide widths around 0.72μm and 1.44μm, the TM mode

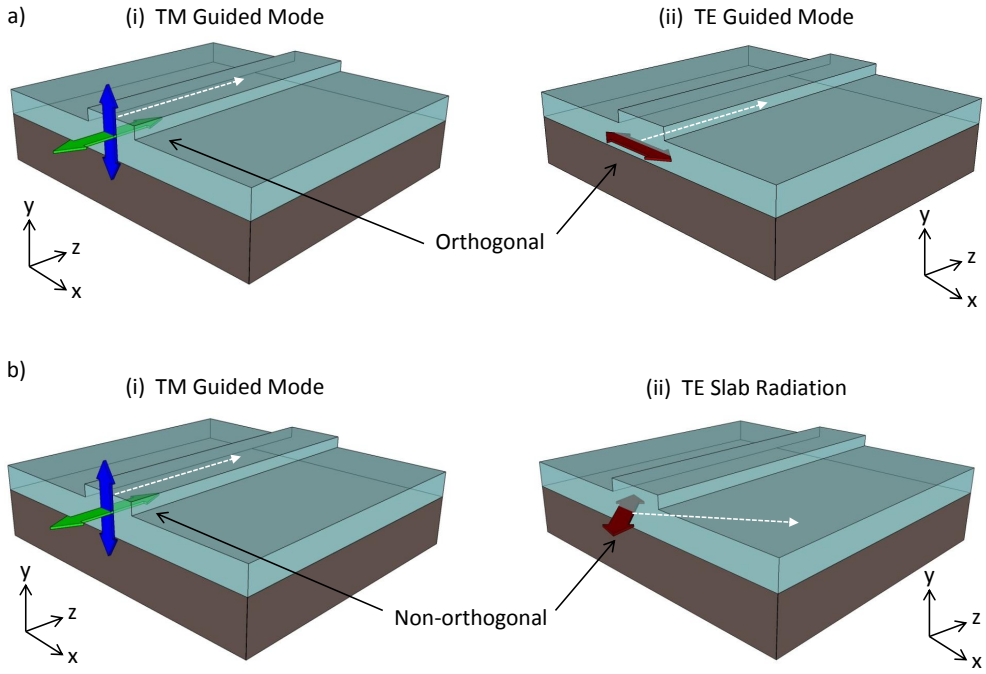

Figure 1.1: (a) Shows the orthogonality between the TM guided mode and TE guided mode electric field polarizations. (b) Shows the non-orthogonality between the TM guided mode and the TE slab radiation mode electric field polarizations.

loss decreased significantly to the point of equalling the propagation loss of the TE mode. There was certainly a strong dependence of the TM mode loss on the waveguide width.

A phenomenological approach was used in [10] to account for this cyclic change in the TM mode propagation losses. This approach looked at the mode coupling conditions that can exist between the various modes in the waveguide structure to account for the lost power in the TM mode. These are namely mode non-orthogonality, phase matching and the perturbation where the coupling occurs. To understand this loss phenomenon, it is necessary to look at these factors in greater detail to understand why this phenomenon is observed specifically in thin-ridge waveguides and why it is strongly width dependent.

1.1.1 Mode non-orthogonality

In addition to the TE and TM guided modes that propagate in a thin-ridge waveguide, there are also slab modes that can propagate unbounded within the slab regions adjacent to the waveguide. The TM guided mode of the waveguide is always orthogonal to the TE guided mode. This is depicted in Figure 1.1 (a) (i) and (ii) which depicts the electric field components of the TM guided mode and TE guided mode respectively. It should be noted that the TM guided mode has a significant longitudinal electric field component which is parallel to the z-axis of the waveguide. The TM mode also has a vertically oriented electric field component which is shown to be parallel to the y-axis. However, the TE guided mode has a predominantly lateral electric field component along the x-axis and has a very small electric field component in the z-axis.

One can also compare the TM guided mode to the TE slab modes which are unbounded in the surrounding slab region. Figures 1.1 (b) (i) and (ii) respectively illustrate the electric field components of the TM guided mode and a TE slab mode which propagates at an angle to the waveguide z-axis. This TE slab mode is bound vertically into a discrete mode with a specific propagation constant, however, the wave is not bound laterally and is free to propagate at any angle to the z-axis. Thus, the depiction in Figure 1.1 (b) (ii) is simply one of the many possible directions that the TE slab mode can propagate in. Remember that the TM guided mode has a significant longitudinal electric field component in the z-axis. If the TE slab mode is propagating at an angle to the z-axis as illustrated in Figure 1.1 (b) (ii), its electric field that is transverse to the direction of propagation of the wave will have a significant projection onto the z-axis. Therefore, it is possible for the TM guided mode to be non-orthogonal relative to TE slab modes propagating at an angle to the waveguide.

1.1.2 Phase matching

For coupling to occur between two propagating modes, it is imperative for them to be phase-matched. This means that their phase-velocities, or propagation constants, or effective indices are equivalent in a particular direction of propagation. It was shown in [10] and explained in Section 1.1.1 that the TM guided mode

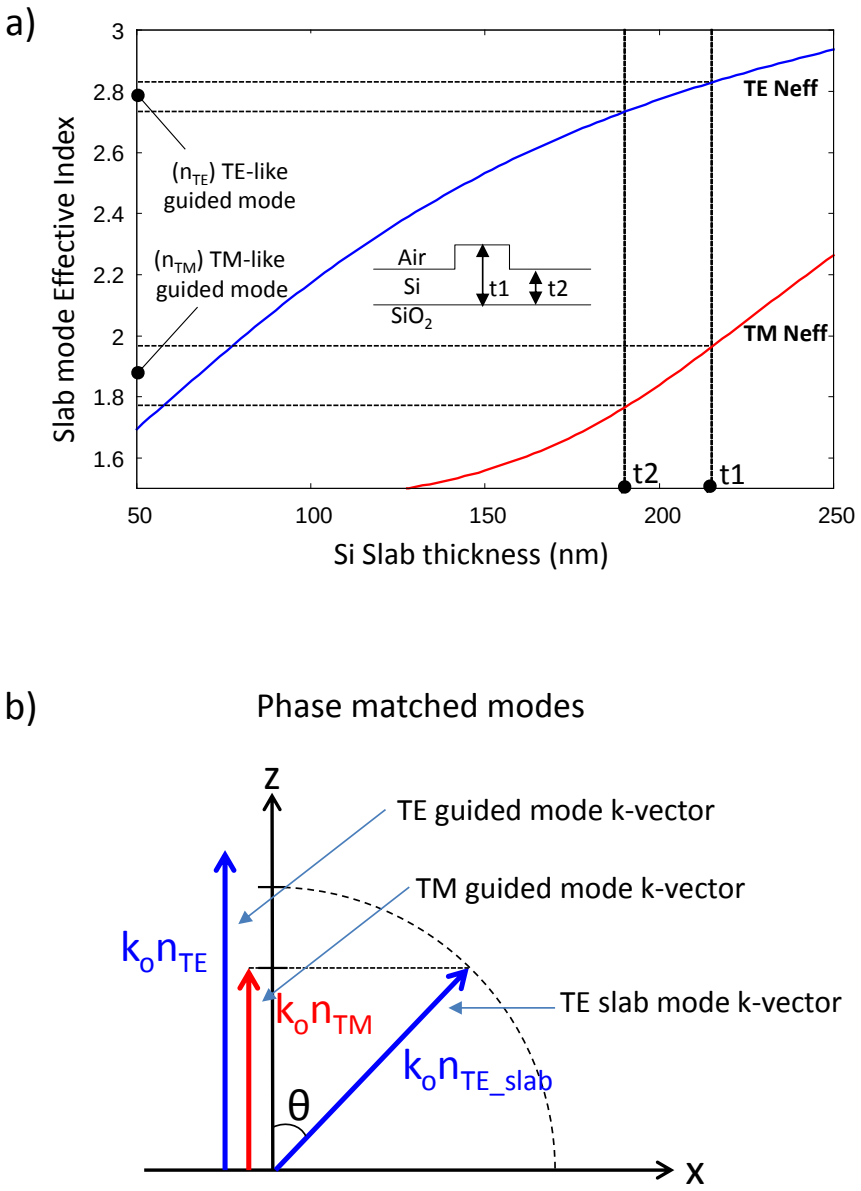

Figure 1.2: (a) Plot of the slab waveguide thickness against the slab mode effective index for both the TM and TE polarizations at a wavelength of 1550nm. (Inset: Silicon (n=3.4797) thin-ridge waveguide cross-section with a silica (n=1.444) bottom cladding and Air (n=1) top cladding). (b) The k-vector comparison between the guided TE mode, guided TM mode and a TE slab mode phase matched to the guided TM mode in the z-axis.

and TE radiation can be non-orthogonal. It was also shown in [10] how the TM guided mode and TE radiation can be phase matched. To explain this possibility it is necessary to consider the effective index of the TM guided mode relative to TE slab modes which can have an infinite number of propagation directions in the slab.

It is possible to predict any phase matching that may occur between the guided and radiated modes by evaluating the slab mode effective indices as was done in [10]. The slab mode effective indices can be evaluated for the TE and TM slab modes as a function of the silicon slab thickness. Figure 1.2 (a) shows the evaluated slab mode effective index as a function of the slab waveguide thickness for both the TE and TM polarizations. The slab thickness of the core region in the thin-ridge waveguide shown in the inset figure is labelled as t1 which is equal to 205nm as used in [10]. The slab thickness of the slab region adjacent to the thin-ridge waveguide is labelled as t2 which is equal to 190nm as used in [10]. As illustrated in Figure 1.2 (a), the guided TM mode effective index must reside between the effective indices of the TM slab modes which are guided by slabs of thicknesses t1 and t2. Similarly, the guided TE mode effective index must reside between the effective indices of the TE slab mode at t1 and t2.

However, the TE slab modes propagating in the slab region of thickness t1 would have an effective index which is higher than the effective index of the guided TM mode. Figure 1.2 (b) illustrates a comparison between the propagation constants of the TE and TM modes in the waveguide structure. In the z-axis direction, the TE guided mode and also a TE slab mode propagating in the z-axis direction would both have a larger propagation constant in comparison to the TM guided mode. Unlike the TE guided mode, the TE slab modes have freedom of propagation direction in the x-z plane. Consequently, there exists a TE slab mode whose angle of propagation relative to the z-axis, gives it an equal phase velocity to the guided TM mode in the z-axis. This is illustrated in Figure 1.2 (b) as a TE slab mode propagating at an angle θ to the z-axis. As such, the TM guided mode is not only phase matched to this particular TE slab mode in the z-axis direction but is also non-orthogonal to it as was discussed in Section 1.1.1.

1.1.3 Perturbation

As described in [10, 15], coupling between the TM guided wave and TE slab mode occurs at the waveguide walls which act as a refractive index perturbation between the core and slab regions of the waveguide. This coupling process between the TM guided wave and the TE slab radiation is depicted in Figure 1.3 similar to the depiction in [10]. At each waveguide wall, the TM mode couples to TE slab radiation propagating in both directions at an angle to the waveguide wall. In Figure 1.3 the reflected TE slab waves at the waveguide walls have been neglected for simplicity of the image as well as the fact that they would be insignificant due to the small index change across the 15nm thick waveguide wall. The transmitted TE slab radiation generated on each side of the waveguide is composed of two co-propagating TE slab modes generated from both waveguide walls. This occurrence therefore also predicts that the result of the superposition between the two co-propagating TE slab modes on either side of the waveguide is dependent on the relative phase between the two modes. If the phase of one TE slab mode generated at one waveguide wall is in-phase with the TE slab mode generated from the adjacent waveguide wall, then the TE radiation will be maximum. On the other hand, when the TE slab mode from one wall is out-of-phase with the TE slab mode from the adjacent wall, then the two radiating beams will interfere destructively resulting in net zero TE slab radiation.

Based on Figure 1.3, and as highlighted in [10], the phase between the TE slab modes generated from either waveguide wall is dependent on the waveguide width or the separation between the waveguide walls. Therefore, at particular waveguide widths, the TE radiation from both waveguide walls can be out-of-phase and interfere destructively resulting in zero TE slab radiation. Similarly, at a different waveguide width where the TE slab modes generated at the waveguide walls interfere constructively, the TE slab radiation can reach a maximum. This therefore explains the strong dependence of the TM mode loss on the waveguide width shown in [10].

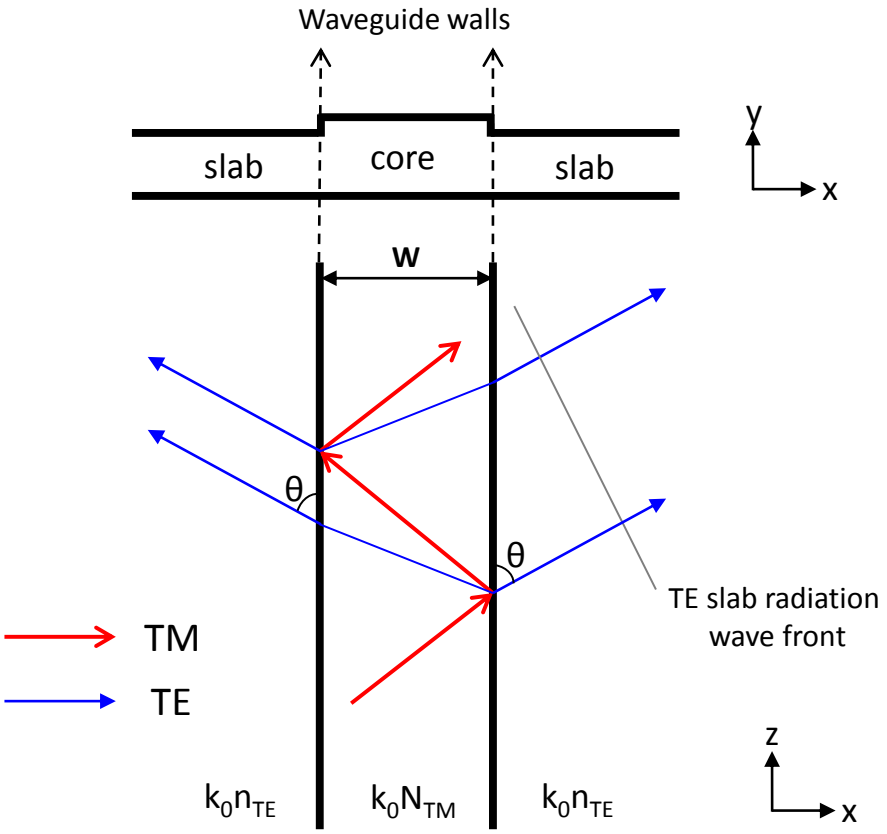

Figure 1.3: TM to TE mode coupling occurs at the waveguide walls which act as perturbations. TE slab modes are generated from both waveguide walls, in both directions and propagating at an angle θ to the waveguide. The phase between the co-propagating TE slab modes determines the TE radiation loss from the TM guided mode.

1.1.4 Simulation of lateral leakage radiation

To simulate and illustrate this lateral leakage behaviour of a TM thin-ridge waveguide, a mode matching simulation technique was used in [15] for a waveguide with a core thickness of 205nm and an etch depth of 15nm. The numerical tool used in [15] was obtained for the investigations of this thesis and the simulations were repeated to illustrate the TM mode loss dependence on the waveguide width. Figure 1.4 (a) shows the TM mode loss in the thin-ridge waveguide as a function of the waveguide width. It is clear from the results of Figure 1.4 (a) that the TM

mode loss changes significantly with the waveguide width.

For example, at a waveguide width of 1μm, it is observed that the TM mode loss is at a maximum position. Figure 1.4 (b), (c) and (d) shows the x, y and z electric field components respectively of the guided TM mode in this 1μm waveguide. The y-directed electric field component (Ey) indicates that the guided mode is radiating into TE polarized radiation propagating laterally in the slab waveguide. Therefore at this waveguide width the TE radiation generated from both waveguide walls interferes constructively resulting in maximum lateral leakage radiation experienced by the TM mode.

On the other hand, a waveguide width of 1.43μm is observed to have the lowest TM mode loss. Figure 1.4 (e), (f) and (g) shows the x, y and z electric field components respectively of the guided TM mode in this 1.43μm waveguide. A comparison between Figure 1.4 (c) and (f) indicates that the electric field of the TM mode in the 1.43μm waveguide is confined and does not radiate into the TE polarization. This therefore represents the waveguide width at which the TE radiation generated at both waveguide walls is out-of-phase and results in destructive interference.

These results show very low propagation losses at about 0.72μm and 1.43μm which agrees with the observed measurements made in [10]. The fact that the results of Figure 1.4 compare well with the results presented in [10] provides confidence that the numerical tool obtained for these studies can be used effectively to replicate the results of that previous work and thus could now be used to pursue the novel investigations contained in the remainder of this thesis. Figure 1.4 also provides an insightful illustration of the lateral leakage loss behaviour which can be predicted for thin-ridge waveguides.

1.1.5 Summary and outlook

The presence of this TE polarized lateral leakage radiation phenomenon in a thin-ridge waveguide raises questions about the possible exploitation of this particular behaviour. What distinguishes lateral leakage radiation from other common radiation losses is the fact that the guided TM mode radiates into a highly coherent TE slab mode since it propagates at a very specific angle to the waveguide. There-

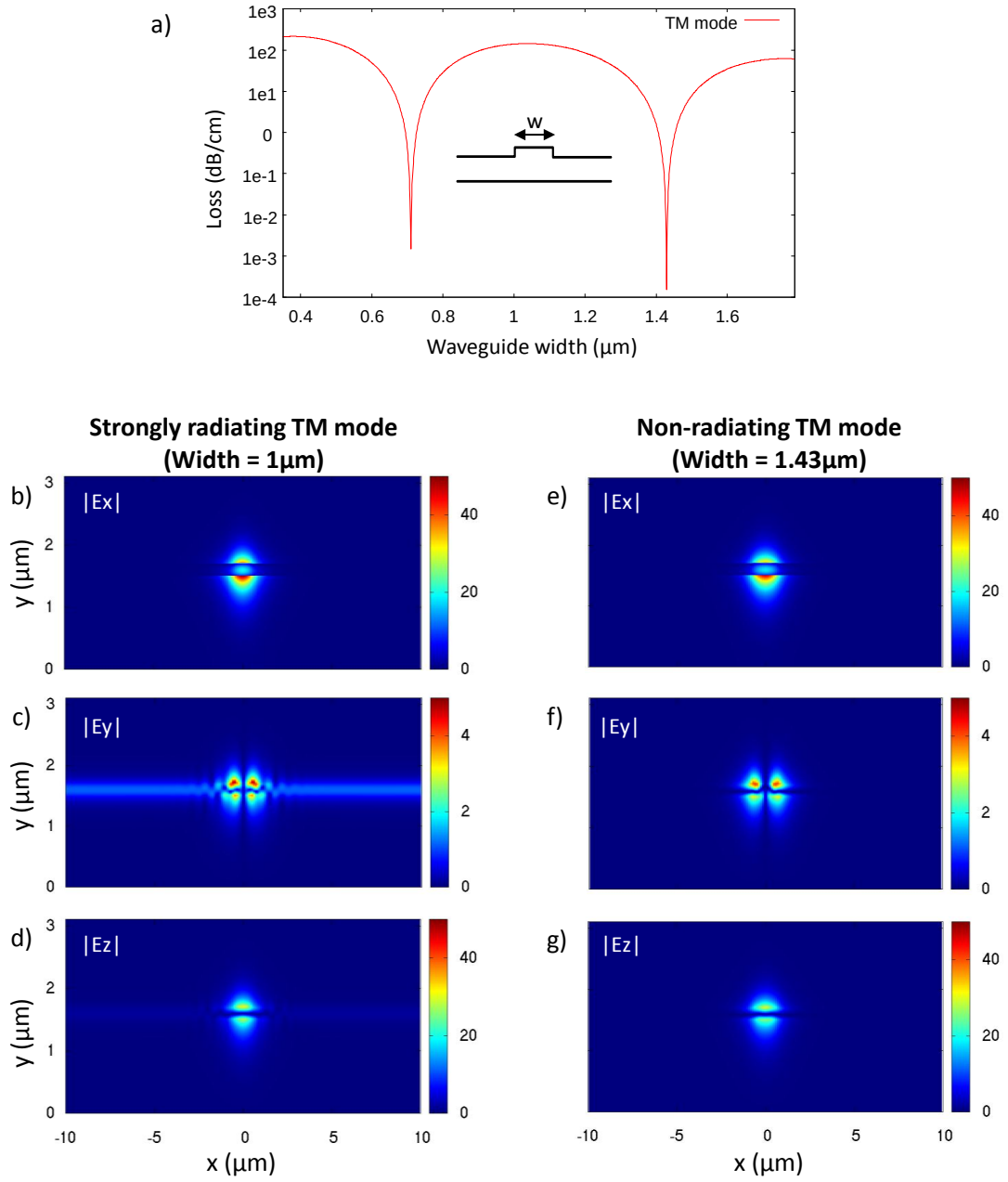

Figure 1.4: (a) The guided TM mode loss as a function of the waveguide width. (b),(c) and (d) shows the magnitude of the TM mode electric field for a strongly radiating waveguide of 1μm width. (e),(f) and (g) shows the magnitude of the TM mode electric field for a non-radiating waveguide of 1.43μm width.

fore, unlike incoherent radiation losses due to scattering, it is feasible that the coherent TE slab mode could be recovered in its entirety. If the optical power and information in the TE slab mode can be recovered, then it would be possible to exploit the lateral leakage phenomenon in an application where the TM-TE coupling relationship is perturbed to a measurable degree.

One possible application that arises in a thin ridge waveguide relates to the strong evanescent field of the guided TM mode due to the high index contrast of the silicon waveguide. The strong TM mode evanescence is evident in the simulated electric field results in Figure 1.4 (c). A strong evanescent field generally translates into a higher susceptibility to perturbations at the waveguide surface. Therefore, one could ask the question - would this lateral leakage radiation be affected by external perturbations of the evanescent field? Another observation made was that the lateral leakage effect involves coupling between a TM guided and TE slab mode which are usually orthogonal polarizations. Given their intrinsically coupled state in the thin-ridge waveguide, one could ask - is it possible to exploit this TM-TE coupling of the lateral leakage effect for polarization conversion purposes? These are some of the questions that will be explored later in this thesis. Three specific application areas formed the basis for the work in this thesis; namely biosensing, polarization conversion and optical filtering. Each chapter focusing on a specific application begins with a detailed introduction and literature review of the application area under question.

1.2 Thesis outline

In Chapter 2, the goal is to investigate whether it is possible for the lateral leakage effect in thin-ridge waveguides to be exploited for evanescent field sensing. Particularly sensing targeted towards biological materials. Firstly, the state of the art in integrated optical biosensing is explored to identify important characteristics of optical biosensors and how the thin-ridge waveguide may be advantageous for this purpose. It has been shown that thin-ridge waveguides can provide a low scattering loss silicon waveguide platform which is identified as a challenge faced by biosensors based on deeply etched silicon waveguides. Through simulation, the effect of a nanoscale film of material - representing a layer of antibodies or

other biomolecules deposited on the surface of a thin-ridge waveguide is studied with respect to how it influences the lateral leakage effect. A potential sensor topology based on a thin-ridge waveguide taper and a planar lens structure is proposed which could enable the observation of changes to the lateral leakage radiation caused by biomolecular deposition.

Chapter 3 focuses on investigating the potential application of the lateral leakage effect for efficient polarization conversion based on its intrinsic TM-TE coupling behaviour. A study of polarization converters looks to identify the types of polarization converters that exist and opportunities that thin-ridge waveguide structures may exploit. It is found that polarization conversion in high index SOI waveguide is not trivial and existing structures can be quite complex and of varying effectiveness. The lateral leakage effect in thin-ridge waveguides provides a simple mode-coupling mechanism that could be exploited for polarization conversion. The challenges of polarization conversion using thin-ridge waveguide structures is also explored in the form of a discussion. It is proposed that a holographic approach can be utilized to devise a structure resembling a grating pattern which could efficiently convert a TE polarized beam into the TM polarization. A binary approximation of this grating pattern for TE to TM beam conversion is simulated using the eigenmode expansion method. Various optimizations to the binary grating pattern are investigated to help achieve efficient polarization conversion from an incident TE beam to a TM beam.

The study of Chapter 4 is based on a serendipitous discovery encountered while researching grating based polarization converters in Chapter 3 where significant TE field reflection occurred when a TE beam was incident on the grating. Chapter 4 proposes that this may be due to resonant coupling from the TE polarization to the TM polarization and then back again into a reflected TE polarization; and asks the question - if it is indeed a resonance effect, what opportunities could this avail? The chapter begins by exploring existing optical resonator applications and it is found that optical filtering for applications such as wavelength division multiplexing is an important field to which resonators have been applied. The state of the art in integrated optical filtering is investigated to identify the important features of filters as well as opportunities for improvement. Coupled resonator optical waveguides (CROWs) in SOI are found to have

sharp spectral filtering characteristics while being physically compact. However, fabrication errors in deeply etched silicon CROWs adversely affect their spectral filtering characteristics. It is concluded that the low scattering loss thin-ridge waveguides could therefore have an impact here. To investigate if the observed reflection in Chapter 3 is indeed due to a resonance effect, only a single waveguide is utilized instead of a grating, and a TE slab mode is launched towards it at an angle where it is phase matched to the guided TM mode. The wavelength dependence of this proposed resonance effect is also studied. For a typical resonator, it is known that the quality factor (Q) of the resonator can be manipulated by adjusting the coupling into and out of the resonant cavity. If the analogy between the thin-ridge and a typical resonator holds, then factors affecting the lateral leakage effect should influence the Q of the thin-ridge waveguide resonance. Factors investigated include the waveguide width and the waveguide height. The next section of the chapter explores the possibilities and challenges of designing coupled resonator filters using thin-ridge waveguide resonators. An example of a third order and fifth order Chebyshev filter based on thin-ridge waveguides are synthesized and simulated.

Chapter 5 of the thesis is the conclusion which summarizes the key findings of the research work presented in this thesis and proposes new interesting research directions. One key finding is the ability to efficiently rotate the polarization of an incident TE beam into a TM beam using thin ridge waveguide grating structures. Based on these findings, it is proposed that this grating structure could be investigated for polarization splitting and rotation for TE-TM or TM-TE conversion. A second discovery is the resonance effect that thin-ridge waveguides exhibit when a TE field is incident on the waveguide at a phase matched angle of propagation. This led to the ability to utilize thin-ridge waveguides of varying Q-factors to synthesize coupled resonator structures which exhibit improved spectral filtering characteristics. In addition to optical filtering, these resonators could also potentially be exploited for optical sensing, non-linear optics, optical delay lines as well as optical switching.

1.3 Research publications

It is my belief and I understand it is also the belief of my supervisors that the findings of this thesis represents several highly significant advancements in the field of integrated photonics. This is underscored by the patent application submitted with respect to this work as shown in the patents list below. Due to this patent process, it has been necessary to postpone publication of much of this this work. However, since the patent has been submitted almost simultaneously with the submission of this thesis, it will now be possible to pursue publication of this work in appropriately high profile outlets.

The following publications and publication drafts have been produced:

Patents:

- Australian Provisional Patent Application No. 2015901035, in the name of RMIT University WM Ref: P40221AUP1.

Journal papers:

- One manuscript on the work presented in Chapter 3 on polarization conversion has been written and is awaiting submission. The manuscript is shown in Appendix B.

Conferences:

- Kiplimo Yego, Thach G. Nguyen, and Arnan Mitchell. "Evanescent wave sensors utilizing laterally radiating thin-ridge silicon-on-insulator waveguide tapers." In *2014 OptoElectronics and Communication Conference, OECC 2014 and Australian Conference on Optical Fibre Technology, ACOFT 2014,* pages 577-579, 2014. [16]

- Kiplimo Yego, Thach G. Nguyen, and Arnan Mitchell. "Utilization of Coherent Lateral Leakage Radiation from Thin-Ridge SOI Waveguides for Integrated Optical Evanescent Biosensing." In *JSAP-OSA Joint Symposia 2012, The 73rd Japan Society of Applied Physics Autumn Meeting,* 11p-G2-13, 2012. [17]

Chapter 2

Evanescent wave biosensing using lateral leakage radiation in thin-ridge waveguides

2.1 Introduction

Chapter 1 looked at the advantages and motivations for the use of the silicon-on-insulator (SOI) platform for the development of integrated optical devices. Various types of SOI waveguide structures were introduced as well as some of their unique advantages and applications. Thin-ridge waveguides on the SOI platform were identified as having a significant advantage of low scattering losses due to the small ridge height unlike deeply etched silicon waveguides. However, it was also explained that while the TE mode does propagate with low loss the TM mode of the thin-ridge waveguide suffers from a significant width dependent loss caused by the TM mode coupling to a TE slab mode propagating at a specific angle to the waveguide. This TM-TE coupling occurs at both thin-ridge waveguide walls and in both directions, and has hence become known as lateral leakage. This TM-TE coupling explained the width dependency of the lateral leakage loss because the coherent TE slab modes generated at both waveguide

walls interfere with each other. If the optical path length between the waveguide walls (the waveguide width) enables the TE slab modes to be out of phase, they would interfere destructively and no lateral leakage radiation would be observed. Similarly, they can be in-phase resulting in maximum lateral leakage radiation

This review of the lateral leakage phenomenon raised some interesting questions. Does it mean that the TM mode is not useful in thin-ridge waveguides because it is lossy? It was proposed in the introduction that, in fact, the TM mode may be useful because the coherent nature of the TE radiation makes it recoverable unlike randomly radiated light. Therefore, one could ask - what potential exploitation or application could be gained from this lateral leakage effect? One feature that was identified is that the TM mode in a thin-ridge waveguide is strongly evanescent while the TE slab mode to which it is coupled is not. This opens up the possibility for exploiting this difference in evanescence for applications that rely on strong interactions with the evanescent field of a waveguide. Another identified characteristic of the lateral leakage phenomenon is the coupling that occurs between the TM guided mode and TE slab mode. This raised the question on whether it is possible to utilize this effect for polarization conversion. These were the possible exploitations that were identified in the introduction. The focus of this chapter will be the first question: Is it possible to exploit the different evanescent field strengths of the coupled TM guided and TE slab modes in thin-ridge waveguides for applications that rely on strong interactions with the evanescent field of a waveguide?

Before trying to explore whether it is possible to use the evanescent field of the thin-ridge waveguide, it will be valuable to review existing technologies exploiting the evanescent fields of waveguides. The evanescent fields of waveguides have been exploited for example in biomolecular sensing [18], in chemical sensing [19] as well as for integrated spectroscopy [20, 21]. Integrated spectroscopy is a more advanced application of evanescent field detection compared to general biomolecular and chemical mass sensing. It requires having a device [21] or devices [20] having a range of wavelength channels to be able to probe an analyte across a wide range of different excitation wavelengths. As a proof of principle, it is easier to look at the simpler sensing mechanisms such as biomolecular and chemical mass sensing. Biomolecular unlike chemical evanescent field sensors are used for de-

tecting molecules in a liquid [18] rather than gaseous environment [19]. This has made evanescent field sensors preferable for biosensing due to the practical ease of immobilizing biomolecules in a liquid environment onto the waveguide surface where it can strongly interact with the evanescent field. Biosensing could therefore be a suitable starting point for investigating the use of the strong evanescent fields in thin-ridge waveguides.

Fan et. al. [18] did a review of optical biosensors that traverse various platforms including surface plasmon resonator sensors, interferometric sensors, microsphere resonator sensors, ring resonator sensors optical fiber and photonic crystal sensors. They showed that integrated planar waveguide sensors were mostly outperformed in sensitivity by non-integrated sensors such as low loss silica microspheres. However, a motivation for utilizing planar waveguide structures has been identified as the extremely small foot print they can occupy enabling dense integration of sensor arrays as well as being easily combined with microfluidic systems for lab-on-a-chip applications. This bodes well for portable sensors that can be taken to the point-of-care rather than being confined in a laboratory due to bulky optical components.

For cheap and mass fabrication of integrated optical sensors, it has also been identified that the CMOS compatible silicon waveguide platform is well suited [22]. In 2006, Densmore et. al. published a seminal paper on silicon-on-insulator (SOI) based evanescent field sensing [3]. They compared the silicon waveguide to a wide range of other waveguide platforms including silicon nitride, polymer and silica waveguides to show the enhanced sensitivity of SOI waveguides for both affinity and bulk evanescent field sensing.

These advantages of optical biosensing in integrated silicon-on-insulator waveguides makes it an interesting proposal to consider the use of SOI thin-ridge waveguide structures for evanescent field biosensing. This chapter looks at two main questions pertaining to thin-ridge waveguide sensing. Firstly,is the lateral leakage effect in thin-ridge waveguides perturbed by biomolecular deposition on the waveguide surface and if so, how? Secondly, what sensor topology could be used to demonstrate this biosensing capability in thin-ridge waveguides? However, before delving into this investigation one must first ask, what are the characteristics of a good evanescent field biosensor? This question will be explored first by

investigating existing SOI evanescent field biosensors.

The following literature review will focus on the transduction mechanism of state of the art optical sensors. This refers to the mechanisms used for converting a binding signal, as a result of biomolecular deposition on the waveguide surface, into a measurable optical signal. There are other components to the front and back-end of the sensor such as the interpretation of the optical signal to extract the relevant binding signal. However, it is assumed that these components external to the transduction process are common across the various types of optical sensors and hence are omitted in this literature review.

2.2 Review of SOI evanescent field biosensors

Silicon-on-insulator evanescent field biosensors can be categorized according to the type of sensor topology used or according to the type of waveguide used. If the goal is to investigate thin-ridge waveguides as a platform for biosensing, then the question one first needs to ask is what are the important features of a waveguide biosensor? Secondly, what properties of a thin-ridge waveguide makes it unique and therefore potentially advantageous for waveguide based biosensing? Consequently, to answer these questions, a good perspective may be look at the existing biosensors from the point of view of the type of waveguide used. These include nanowire waveguides, slot waveguides, photonic crystal waveguides and ridge waveguides.

2.2.1 Nanowire waveguide biosensors

In 2006, Densmore et. al. published a significant paper on SOI based evanescent field sensing [3]. They compared the SOI waveguide to other waveguide platforms including silicon nitride, polymer and silica waveguides. Their results showed that TM guiding SOI waveguides were significantly more sensitive to surface refractive index changes due to the strong evanescent field. As a proof of concept, the nanowire waveguide was used in a Mach-Zehnder interferometer (MZI) topology to form a refractive index sensor. One arm of the MZI formed the sensing arm while the other formed the reference arm. The sensing arm was left exposed

to the environment while the non-sensing portions of the MZI, including the reference arm, was covered by a polymer. Fluids of different concentrations were then introduced over the sensing arm. This caused a shift in the phase between the sensing arm and the reference arm. A phase shift versus superstrate index change relative to deionized water was measured as $300(2\pi)$ per refractive index unit (RIU^{-1}).

Using the same nanowire waveguide, the same group improved on the MZI topology whereby the length of the two arms in the interferometer was increased by folding them into spiral paths [23]. The spiral-path increased the interaction length between the analyte and the light in the waveguide and was therefore expected to enhance sensitivity. However, from the recorded measurements, the improvement in phase shift change due to increased fluid concentrations was measured at $460(2\pi)$ RIU^{-1} which was only slightly better than that observed previously [3].

Another waveguide sensor topology based on the nanowire waveguide was proposed in [24] where a Bragg grating structure was fabricated directly onto the waveguide walls. The Bragg grating structure takes the form of small periodic index perturbations whereby specific wavelengths resonant in the grating are completely reflected. This results in a notch in the transmission spectrum of the waveguide grating. When used as an evanescent field sensor, variations of the superstrate refractive index was shown to cause a spectral shift in the waveguide's transmission spectrum. The reported measurement resolution was as high as 10^{-6} RIU for bulk refractive index changes for a device length of 180μm. However, this proposed grating technique, unlike the MZI which uses a reference arm, is highly susceptible to spectral shifts caused by temperature changes due to the large thermo-optic coefficient of silicon.

A common biosensor topology where the nanowire waveguide has been exploited is in ring resonator structures [22, 25–28]. De Vos et. al. [22] utilized a SOI ring resonator structure to demonstrate label-free measurement of biomolecules adsorbed or deposited on the waveguide surface for quantitative molecular detection. The ring resonator with a race-track shape was used in an add-drop topology showing a sharp resonance peak in the transmission spectrum. When biomolecules were deposited on the ring surface, a shift in the resonance peak

was observed The race-track shape was utilized instead of a circular ring because it gave more control over the coupling coefficient between the bus waveguide and the resonator. They concluded that the SOI ring was particularly sensitive for measuring adsorbed biomolecules rather than for bulk sensing of concentration changes in the surrounding fluid with a detection limit of 10^{-5} RIU. Xu et al [25] went further and characterized the effect of the ring radius on the ring resonators spectral sharpness and found that a larger ring radius gives a sharper resonance which would more suitable for detecting smaller changes in the resonance shift caused by biomolecular adsorption. However, a larger ring radius covers a larger area and so they instead utilized a folded cavity topology to achieve the long cavity length of a large radius ring but over a smaller area. The resonance peak of the folded cavity was also much sharper than that of a simple race-track ring. They concluded that with a folded cavity with a Q-factor of about 20,000, a long interaction length could be achieved of 1.27mm within an area of $110\times110\mu m^2$. Multiplexing of several ring resonator biosensors was also shown to be possible by using multiple ring resonators having different radii and hence independent resonances [26, 28]. In this way each resonator sensor could be used for different measurements but they can all be simultaneously probed since each resonator occupies a different resonance wavelength. SOI ring resonators have been successfully trialed in the biological sciences for measuring important biological proteins such as cancer biomarkers [27].

In spite of having several advantages, the ring resonator structure suffers two problems when used for biosensing. Firstly, the positive thermo-optic coefficient of silicon causes spectral shifts due to temperature variations. This problem was solved by using a reference resonator which is not exposed to the biosensing environment and thus only experiences spectral shifts caused by temperature changes [28]. This reference shift is then used to compensate for temperature shifts experienced in the sensing resonator thus accurately evaluating spectral shifts caused by biomolecular adsorption. This however takes up valuable real estate on the chip and also requires additional post-processing of the evaluated data to obtain correct measurement data.

Another intrinsic problem of ring resonators known as resonance or mode splitting occurs at resonance resulting in a dual peak [29]. This is due to the

presence of a forward (clockwise) propagating and backward (counter-clockwise) propagating resonant modes which are degenerate. Generally the backward propagating mode is not expected to be excited, but in practice surface roughness on the ring can lead to coupling to this backward propagating mode.

Whispering gallery mode (WGM) resonators in SOI waveguides, which take the form of disk resonators, have also been exploited for label free integrated biosensing [30, 31]. Boyd and Heebner [30] wrote a seminal paper in 2001 proposing the use of disk resonators for biosensing. Like ring-resonators, adsorption of biomolecules on the disk surface changes the resonant mode effective index and consequently causes a spectral shift of the resonant wavelength. Grist et. al. [31] showed that it is possible to reduce the disk radius to as low as 3μm with the advantage of increasing the free spectral range (FSR) of the resonator which enables multiplexing of several disk resonators. However, this results in a significant decrease in the quality (Q) factor of the resonator thus decreasing its sensitivity. Having a larger disk resonator enables the attainment of higher Q-factors but at the same time increases the number of modes that can be supported in the disk resonator. A multimode disk resonator is non-ideal due to the risk of cross coupling between modes that may be caused by fabrication defects of the resonator. Multimode resonators would also have several spectral peaks for each of the supported modes thus significantly decreasing the FSR and potential of being able to multiplex several resonators.

2.2.2 Slot waveguide biosensors

Slot waveguide structures have also been exploited in the development of integrated optical biosensors [6, 32]. A slot waveguide is composed of two strip or ridge waveguides of narrow width, which are positioned adjacent to each other with a narrow gap between them. This dual-waveguide structure in fact behaves as a single waveguide and supports a quasi-TE and quasi-TM mode that spans both waveguides and the slot [32]. As shown in [32], the quasi-TM mode looks similar to that of a general strip waveguide. However, the quasi-TE mode is quite different in that it appears strongly laterally confined within the slot region. The slot introduces a discontinuity in the laterally oriented TE electric

field which results in a high field intensity maintained within the narrow slot interfaces. It was shown in this paper that the quasi-TE mode had a significantly stronger surface sensitivity. In [6], an almost four fold improvement in sensitivity was demonstrated in a ring resonator based on an optimally designed quasi-TE slot waveguide over a strip waveguide. The slot gap was 100nm wide. The slot waveguide is primarily beneficial when biomolecular binding occurs within the waveguide slot where the field is enhanced. This makes it difficult to ensure precise delivery of biomolecules to the useful sensing area within the slot. Due to the strong lateral confinement of the optical field within the slot, scattering loss due to surface roughness would be enhanced in slot waveguides. Therefore, great care needs to be taken with their fabrication - particularly in ring resonators.

2.2.3 Photonic crystal waveguide biosensors

Lee and Fauchet [33] in 2007 proposed the utilization of a silicon photonic crystal microcavity for single particle detection. The lattice constant was 400nm and the pore diameter used was 240nm. The microcavity defect was achieved by increasing a single pore size to 685nm. The microcavity was introduced into the photonic crystal lattice such that it supported a defect cavity mode which appears as a spectral transmission peak inside the spectral bandgap of the photonic crystal. Lee and Fauchet proposed the potential use of this structure for biosensing by testing its sensitivity to an artificial single particle of 320nm diameter which was placed inside the microcavity. It was observed that the transmission peak was shifted by as much as 4nm when the particle of 320nm diameter was at the edge of the cavity.

The defect mode can be supported inside the photonic bandgap of a photonic crystal (PC) in other ways than with a microcavity. An entire row of holes in the PC lattice can be removed [34] to form a line defect waveguide, or the holes of a an entire row can be made of smaller dimensions to the other holes in the PC [35]. Garcia-Ruperez et. al. [34] proposed using a line defect in a PC with a lattice constant of 390nm and a pore size of 110nm. Rather than monitoring the band-edge of the guided mode they utilized the sharp fringes in the slow-light regime near the guided mode band-edge. The benefit is that in the slow-light

regime the interaction with the target biomolecules is enhanced. They tested the detection capability with standard anti-BSA/BSA binding tests and concluded that they could attain an extremely low mass detection limit of 2.1pg/mm^2. The refractive index sensitivity was measured as 174.8nm/RIU. More recently, Dutta and Pal [35] proposed the use of a line defect in a SOI PC lattice to achieve an even higher sensitivity of 260nm/RIU. Their proposed sensor topology relied on the detection of the cut-off wavelength of the guided defect mode which shifted under the influence of a changing external refractive index.

A particular advantage of using photonic crystals for biosensing was identified as the enhanced field strength provided by the small photonic crystal waveguide dimensions. The enhanced field within the hole and cavity defects consequently increases the light-matter interaction with the adsorbed biomolecules within the defect cavities, thus improving the sensitivity of the device. While the holes and cavity defects are beneficial for providing enhanced light-matter interaction, they also introduce challenges unique to PC biosensors. The presence of such minute surface perturbations could make it more difficult to perform surface chemistry necessary for the biosensing process. This includes both the pre-treatment or functionalization as well as the post-processes of rinsing the waveguide surface. Improper surface chemistry can lead to non-specific biomolecular binding which can lead to false-positive or false-negative results.

2.2.4 Thin-Ridge waveguide biosensors

Thin-ridge waveguides differ from the more common strip and ridge waveguides by the fact that the waveguide is formed by shallow etching the silicon slab layer. The TM mode is particularly attractive for evanescent field sensing due to the strong evanescent field at the waveguide surface [12]. Some demonstrations of biosensing utilizing thin-ridge waveguides for evanescent field biosensing have been presented [36, 37]. The waveguide used in [36] had a width of 1.23μm which was expected to provide a larger surface area for sensing. It was shown that athermal silicon waveguides can be achieved with some constraints applied on the thin-ridge waveguide dimensions. This has the added benefit of not requiring reference waveguides that are generally used to compensate for effective index

shifts caused by temperature changes. A TM thin-ridge waveguide was used in a ring resonator sensor topology and the waveguide width was selected for low loss TM mode propagation to minimize lateral leakage effects. The reported detection limit of surface mass density was calculated as 100fg/mm^2 which in comparison to other sensors was relatively good.

However, a drawback of such a technique could be that when biomolecules are deposited on the waveguide surface not only would the phase velocity of the TM mode change but also it is possible that the lateral leakage loss may vary. The reason for this likelihood is that low loss TM mode propagation in thin-ridge TM waveguides is width dependent due to destructive interference of the TE lateral radiation generated at the waveguide walls as discussed in Section 1.1. Biomolecular deposition on the waveguide surface would have the effect of varying the optical path length between the waveguide walls and could therefore affect TM mode lateral leakage loss. The thin-ridge ring resonator loss has also been investigated [38] and shown to be strongly dependent on the ring radius thus severely limiting the realization of small ring radius sizes. These factors may negatively impact the ring resonator quality factor and hence any improvements on sensitivity based on the proposed ring topology.

2.2.5 Summary

Some important features of optical biosensors have been identified. Firstly, high index contrast waveguide platforms such as SOI are advantageous since they provide a strong field enhancement at the waveguide surface especially for modes with the field oriented normal to the strong index contrast. Enhancing the interaction length between the waveguide mode and the analyte has also been identified as a key criteria to achieving high sensitivity and low detection limits. Consequently, there has been a preference for the use of resonant structures such as ring resonators where the effective optical length of the device is much longer than the physical length. Fabrication errors inherent to deeply etched silicon waveguides pose a problem for ring resonator structures due to scattering losses that lead to such effects as mode splitting. Other waveguide structures such as slot-waveguides and photonic crystal waveguides have also been exploited because

of the optical field enhancement they provide. The difficulty in the exploitation of slot waveguides and photonic crystal waveguides was the difficulty in delivering biomolecules to the enhanced field regions due to their very small size.

The thin-ridge waveguide structure, which is the core subject of this thesis has also been previously investigated for biosensing purposes exploiting the existing ring resonator sensor topology. Because of the inherent TM mode lateral leakage loss behaviour it is believed that thin-ridge waveguide sensors using existing topologies such as ring resonators will be severely restricted. In spite of this, the thin-ridge waveguide topology has advantages over strip waveguides because the small waveguide walls minimize scattering losses common to strip waveguides. This analysis therefore raises an interesting question: Is it possible to realize a biosensor topology that takes advantage of this lateral leakage phenomenon rather than being hamstrung by it?

2.3 Lateral leakage response to an adsorbed biofilm on the waveguide surface

This section investigates through simulation what would happen to the lateral leakage radiation if a biomolecular layer (biofilm) were deposited on the waveguide surface. It is hypothesized that, if a biofilm was deposited on the waveguide surface, the cladding refractive index would be perturbed altering the effective indices of both the guided TM mode and the TE slab mode. This should consequently affect the coupling relationship between the guided TM mode and the TE slab mode.

Consider a functionalized waveguide immersed in a solution whereupon biomolecules suspended in the solution are immobilized onto the waveguide surface to form a continuous biomolecular film (biofilm). This biofilm would have a higher refractive index than the surrounding solution and would therefore increase the cladding refractive index at the waveguide surface. This would consequently alter the effective index of the guided modes in the waveguide.

Now consider a laterally radiating thin-ridge waveguide with biofilm deposited indiscriminately over the entire surface, including both the waveguide and slab

regions. The effective indices of the guided TM and the TE slab modes would both be perturbed by the presence of the biofilm. However, as illustrated in Figure 1.4, the TM mode has a significantly stronger evanescent field that the vertically tightly confined TE slab mode. It would therefore be expected that the strongly evanescent TM mode would vary significantly in effective index compared to the TE slab mode.

A fully vectorial mode matching technique was used to simulate the guided modes of a thin-ridge SOI waveguide. This was done for a range of biofilm thicknesses from 0nm to 500nm with a material refractive index of 1.5, which is a typical refractive index of a biomolecular film [39]. The biofilm thickness was increased vertically to simulate its accumulation on the waveguide surface. In doing so, an approximation was taken in assuming that the biofilm only grows vertically on the waveguide surface and not laterally on the waveguide walls. The impact of biofilm accumulating on the waveguide walls might have a larger impact on the TE-TM coupling strength rather than the phase velocities of the guided TM and radiated TE modes which is of interest in this investigation. In reality the biofilm would probably accumulate laterally as well, but given that the ridge height is significantly less than the biofilm thickness, the impact of this approximation would only be noticeable while the film was thin.

In addition, the lateral increase in biofilm would primarily be significant only over the 15nm waveguide wall whereas the biofilm thickness ranges from 0nm to 500nm which is far greater than the wall thickness. Furthermore, this simplification eases the complexity of the mode-matching simulation.

The simulation window, as shown in Figure 2.1 (a), was bounded vertically by perfectly conducting planes but left fully open in the horizontal direction to accurately model the lateral leakage radiation [15]. Similar waveguide dimensions to [15] were used. A waveguide width of 1μm and etch depth of 15nm was selected to maximize lateral leakage radiation at 1.55μm wavelength.

Figure 2.1 (c) shows the effective index gradient of the guided TM mode and that of the radiating TE slab mode as a function of the biofilm thickness. The effective index rate of change for both modes is initially steep. The change in the guided TM mode effective index is about 4 times greater than that of the radiating TE slab mode. As the biofilm thickness increases, the rate of change in

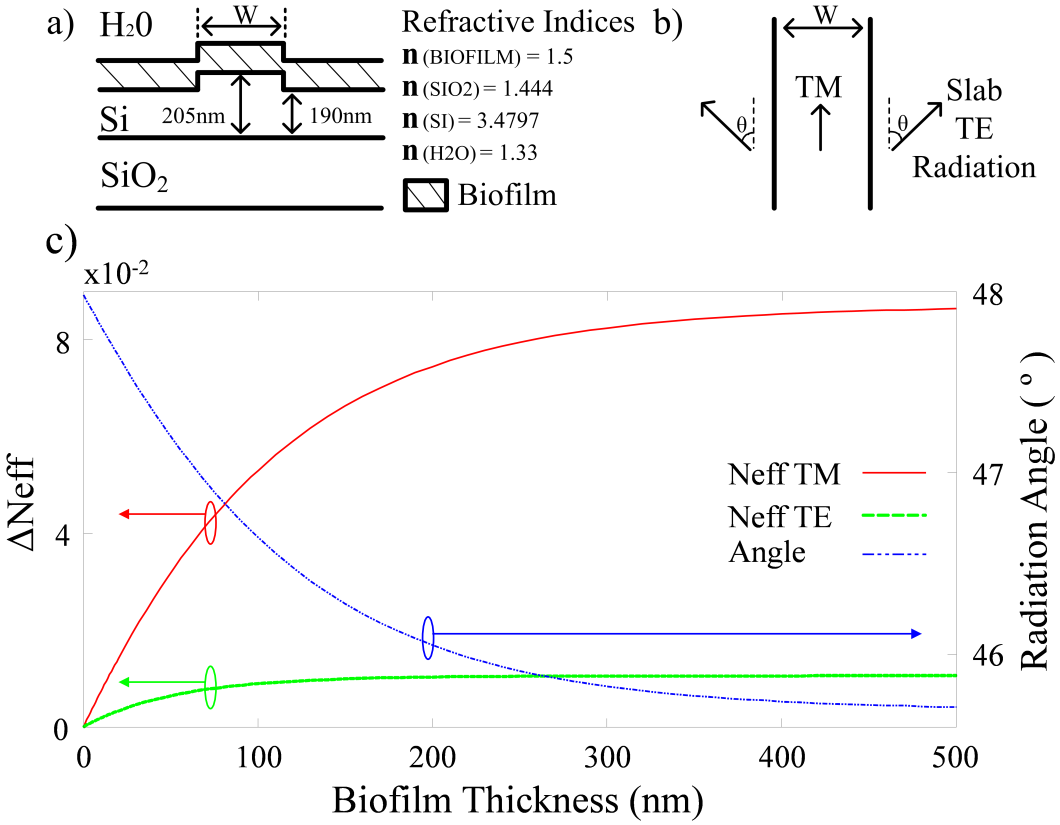

Figure 2.1: (a) Cross sectional view and (b) plan view of the thin-ridge waveguide simulation window. (c) Rate of change of the TM and TE mode indices for varying biofilm thicknesses and the resulting change in TE slab mode angle.

effective index for both the guided TM and TE slab modes decreases and slowly approaches a maximum value.

This decreased gradient is caused by the fact that as the biofilm thickness increases, its interaction with the evanescent tail of the mode above the biofilm also decreases. The steeper TM mode gradient indicates a stronger interaction with the biofilm. This is due to the longer evanescent tail of the guided TM mode extending into the cladding medium as opposed to the vertically tightly confined radiating TE slab mode.

This result shows that the guided TM mode is therefore more sensitive to changes in the biofilm than the radiating TE slab mode.

Since the guided TM and TE slab modes respond differently to the variation of the biofilm thickness, it is expected that the radiation angle illustrated in Figure 2.1 (b) will also vary with the biofilm thickness.

The TE slab mode angle depends on the effective indices of the guided TM mode (N_{TM}) and TE slab mode (N_{TE}) [10], which is expressed as

$$\theta = \arccos(\frac{N_{TM}}{N_{TE}}) \tag{2.1}$$

Using the simulated effective indices of the guided TM mode and slab TE mode, the TE slab mode angle at different biofilm thickness was calculated using Equation (2.1).

Figure 2.1 (c) shows the calculated radiation angle on the right y-axis as a function of the biofilm thickness. The increase in biofilm thickness results in a decreasing angle of radiation. The rate of change for small biofilm thicknesses is higher and this gradient decreases as the biofilm thickness grows.

It is not surprising that this asymptotic curve of the radiation angle is similar to that observed for the effective indices. Since the rate of change of the effective index is highest for small biofilm thicknesses, we would also expect the highest rate of change in the radiation angle for smaller biofilm thicknesses. As the biofilm thickness grows and its interaction with the evanescent field diminishes, its effect on the TM mode's phase velocity consequently also decreases. This results in the characteristic asymptotic curve of the radiation angle as a function of the biofilm

thickness.

This result shows that when a biomolecular film is deposited on the surface of a thin-ridge waveguide the angle of propagation of the TE slab mode is altered.

2.4 An evanescent wave biosensor concept exploiting the lateral leakage effect

In Section 2.3, it was shown through simulation that when a biomolecular film is deposited on the surface of a thin-ridge waveguide, the angle of the TE slab mode generated by the waveguide is altered. In this section, a sensor topology is investigated that could exploit this relationship between the deposited biofilm and the lateral leakage radiation angle.

2.4.1 Sensor topology

Equation (2.1) assumes the ideal case of a longitudinally invariant waveguide with a fixed width and which radiates at only one angle. However, this is not practical since the TM mode launched into the waveguide has to first propagate in a non-radiating structure to arrive at the radiating waveguide. To get from the non-radiating structure to the radiating structure, a transition is needed. If the transition is a simple step function, then the beam will be poorly formed. Instead the transition needs to be gradual. Such a device was demonstrated using a thin-ridge waveguide taper [14].

It has been shown that a tapered thin-ridge waveguide which transitions from a non-radiating waveguide to a strongly radiating waveguide can generate a well collimated Gaussian-shaped TE beam [14]. The tapered thin-ridge waveguide could therefore be a suitable sensing platform. It is expected that the deposition of biofilm on the tapered waveguide would alter the principal angle of radiation of the collimated TE beam just as it did for the longitudinally invariant waveguide.

However, the problem still exists of how to observe the change in angle of such a wide radiating TE beam. Dalvand proposed in his thesis [40] a wavelength division multiplexing (WDM) device concept based on the thin-ridge waveguide taper, which tackles a similar problem to that faced by the waveguide taper used

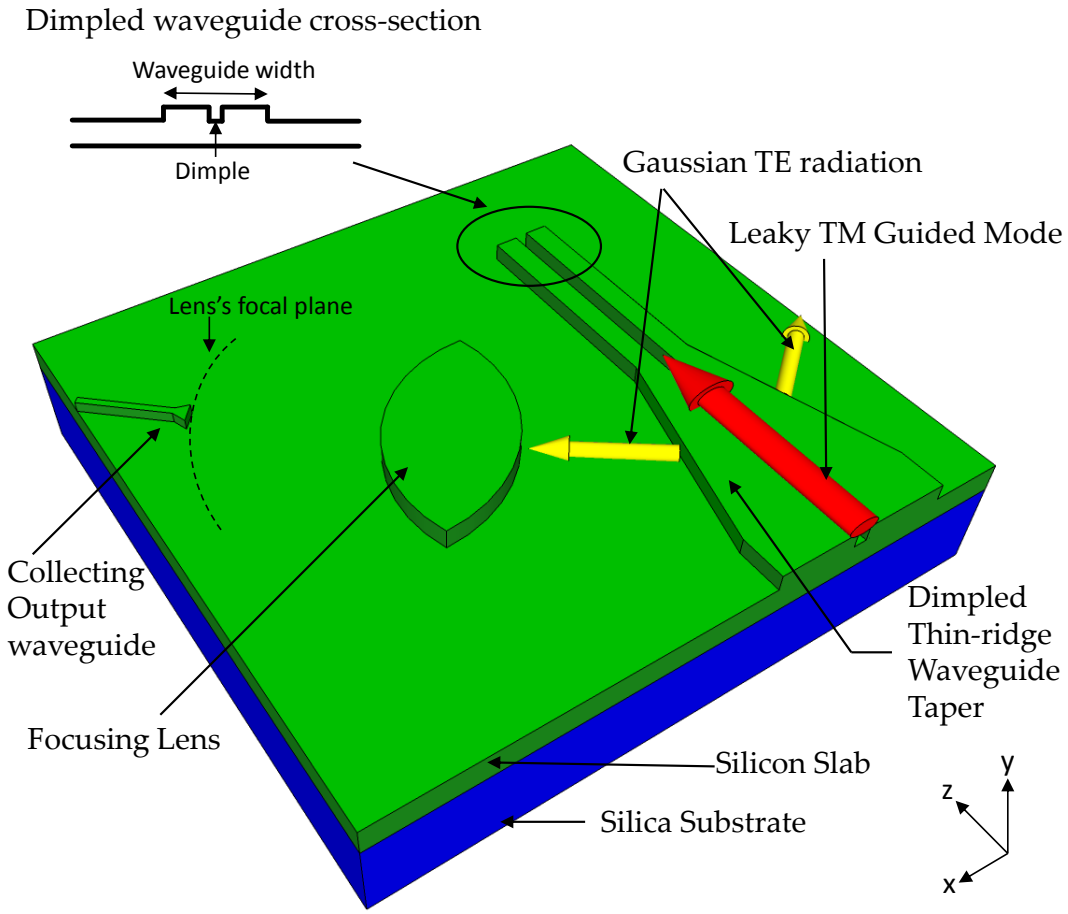

Figure 2.2: 3D render of the sensor topology. The waveguide taper provides the sensing surface and the lens is used to resolve any changes in the TE beam radiation angle by focusing it to the output waveguide at the focal plane. Inset image shows the cross section of a dimpled waveguide structure.

as a sensor. In the WDM device, a waveguide taper was proposed to radiate the waveguide TM mode into a coherent TE beam propagating in the slab waveguide. When the wavelength of excitation was changed, consequently altering the mode effective indices in the waveguide and the slab, the TE beam's angle of radiation, predicted by simulation, was also altered. A planar lens structure was used to focus the coherent TE beam to a narrow focal point. It was shown in Dalvand's thesis that the change in angle of the TE beam results in a shift of the focal point where the beam is focused to at the lens's focal plane. This effect was based on the Fourier transformation properties of a lens [41]. When there is a shift in the angular spectrum of an incident beam, this results in a spatial shift of the transmitted beam resulting in a spatially shifted focal point at the focal plane. Consequently, by positioning several waveguides at the focal plane of the lens, it was shown that it is possible to distribute various input wavelength channels into several separate output waveguides positioned at the focal plane of the lens.

The proposal in this section is that a similar structure as illustrated in Figure 2.2 could also be exploited as an evanescent wave sensor topology. In this sensor topology a thin-ridge waveguide taper is designed to radiate a TE Gaussian-shaped beam. The radiated TE beam is then focused through a planar lens structure, which focuses the beam to a point on the focal plane of the lens. It is expected that if a biofilm were to be deposited on the surface of the waveguide taper, then the angle of the radiated TE beam would also change. The consequence of this should be that when the beam continues to propagate through the lens structure, the TE beam beam would be focused to a different point in the focal plane of the lens. The shift in the position of the focal point of the beam should be relative to the biofilm deposited on the waveguide taper.

If an output waveguide is then positioned at the focal plane of the lens, it will be illuminated by the focused TE beam resulting in a specific amount of power being coupled into the TE mode of the waveguide. As the location of the focused beam should be shifted under the influence of biofilm being deposited on the waveguide taper, the amount of power being coupled into the waveguide should also change. This would consequently result in a direct relationship between the quantity of biofilm being deposited on the thin-ridge waveguide taper and the amount of power coupled into the output waveguide.

2.4.2 Techniques for simulating the thin-ridge waveguide taper sensor

A full 3D electromagnetic simulation of the proposed sensor topology illustrated in Figure 2.2 is not a trivial problem. This is due to the wide separation and large size of the taper and lens structures coupled with the high resolution required to resolve the small waveguide dimensions such as the nm-scale etch depth. To simplify such a 3D numerical analysis, it is simpler to simulate the thin-ridge waveguide taper and the planar lens structure separately. As was done in [14], the thin-ridge waveguide taper can be modelled using a mode-matching approach; while the lens can be modelled using a beam propagation approach [40]. The two problems can be linked together by utilising the TE beam generated from the taper as the input field to the second simulation of the lens structure. This dual approach was used in the simulation of the thin-ridge waveguide taper sensor.

The common options for modeling optical waveguide structures includes the finite difference time domain (FDTD) method, conventional and wide angle beam propagation methods (BPM) and the eigenmode expansion method (EME) [42].

FDTD can be used to accurately model a structure since the exact wave equation satisfying Maxwell's equations is used to calculate the field propagation through the structure. The only approximation made is in discretizing the equation in space and time so that the equations for the electric and magnetic fields can be computationally evaluated. However, the accuracy of this technique is dependent on the discretization resolution used. The resolution has to be high enough to properly represent the field in the smallest refractive index changes within the problem. If the simulation window is small or if the number of dimensions required are few then it is possible to use this method. However, in large 3D simulation windows where waveguide features are very small, as is the case for thin-ridge waveguides, the FDTD method becomes intractable due to the immense computational requirements that are necessary.

In the conventional beam propagation method (BPM) simulation techniques paraxial approximations are made on the field. As such the type of structures simulated with BPM generally need to have fields propagating mainly along one principal axis (generally called the z-axis). If the problem or structure contains

fields propagating at wide angles to this principal axis then the error due to the paraxial field approximations increase leading to inaccurate results. BPM would therefore not be suitable for the simulation of thin-ridge waveguide structures since the propagation of the TM fields in the waveguides and the TE radiating fields are at wide angles to each other of about 50°.

The semi-analytical eigenmode expansion (EME) method simulates the propagation of fields in a waveguide structure by discretizing the waveguide into longitudinally invariant sections. In each section the electromagnetic field is decomposed into a finite set of eigenmodes that exist in the waveguide structure. For a continuously varying waveguide structure, such as a tapered waveguide, the staircase approximation is used to subdivide the taper into longitudinally invariant sections. The advantage of the EME method is that it can model fields propagating at wide angles to the principal z-axis and is also computationally very efficient. The accuracy of this simulation technique is dependent on having an adequate set of eigen modes to correctly represent the propagating field. EME has in fact been exploited for the efficient and accurate simulation of longitudinally varying structures [14]. As a result, the EME method was similarly chosen for simulating the waveguide taper structure in this investigation.

However, the propagation of the TE beam through the planar lens structure was simulated using the beam propagation method (BPM). This was based on the fact that the lens structure has a smooth curvature and it is important that its continuously varying index profile is accurately approximated in the simulation. With the eigen mode expansion which was used in the waveguide taper structure, accurately modeling the lens would mean that the structure would have to be subdivided into a large number of longitudinally invariant sections. This can be computationally very expensive.

On the other hand, since a beam can be expressed as a superposition of paraxial waves [41], the TE beam can also he expressed as superposition of paraxial slab modes. As was done in [43], the BPM simulation method provides an efficient and accurate way to simulate the propagation of the TE beam through the lens structure. In addition to this, there is no expected TE-TM polarization coupling at the lens but only conventional Fresnel reflection and transmission. As such, a 2D approximation of the propagating field can be taken, where only

the TE polarization is considered to be propagating and the background index is equal to the TE slab mode effective refractive index. The Beamprop tool in the Rsoft simulation software was used to perform this simulation.

2.4.3 Simulated thin-ridge waveguide taper response to biofilm deposition

As a first step towards analysing the complete sensor of Figure 2.2, the thin ridge taper was analysed in isolation to predict the effect of adding a biofilm to the taper. It is expected that the deposition of biofilm on the waveguide taper surface will result in a variation of the principal propagation angle of the radiated TE beam.

To explore this proposal the waveguide taper was modeled under different biofilm thicknesses using the eigen mode expansion method as discussed in Section 2.4.2. The dimensions of the waveguide taper were identical to that of the taper presented in Dalvands thesis [40]. The length of the waveguide taper was 140μm and the waveguide width was linearly tapered along this length starting from a non-radiating waveguide width of 1.72μm to a strongly radiating waveguide width of 1.05μm. This waveguide taper topology is illustrated in Figure 2.3 (a) and (b). Similar to the waveguide taper topology in [40], a dimple was positioned at the center of the waveguide as illustrated in Figure 2.3 (a). The dimple structure serves the purpose of enhancing the lateral leakage radiation [44] by increasing the number of waveguide walls where TM-TE coupling can occur. In the waveguide taper design, the dimple allows the length of the taper to be minimized while still coupling about 99% of the power from the TM mode to the TE radiating beam [40]. The etch depth of the waveguide was also increased to 50nm, compared to the 15nm etch depth used in Section 2.3, to meet the 99% coupling requirement along the 140μm taper structure.

Figure 2.3 (c) shows the y-directed electric field component corresponding to the TM polarization. It is observed that the TM mode that is launched into the waveguide taper decays in power as it propagates through the length of the taper. Figure 2.3 (d) shows the x-directed electric field component corresponding to the TE polarization. A TE polarized beam is observed to be propagating at an angle

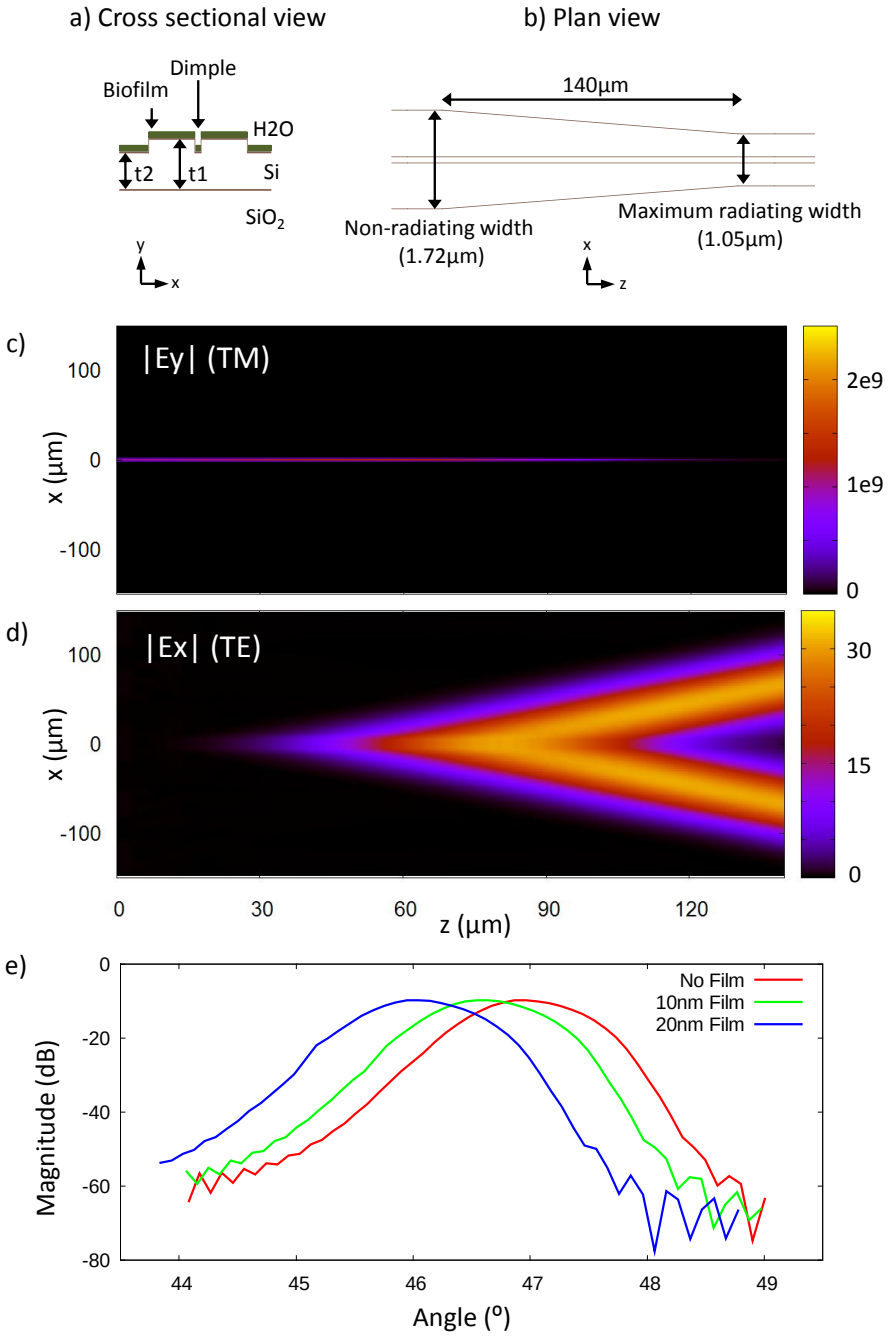

Figure 2.3: (a) and (b) Shows the cross sectional and the plan view of waveguide taper. The dimensions t1=220nm and t2=170nm). (c) and (d) Shows the electric field components for the TM and TE polarizations respectively.(e) Angular spectrum of TE beam for various biofilm thicknesses.

from the waveguide on either side of the taper structure. It is evident that these radiated TE beams have a Gaussian-like amplitude profile.

To analyse the effect of biofilm deposition on the waveguide taper surface, the angular spectrum of the radiated TE beam was plotted and compared over various biofilm thicknesses. As discussed in Section 2.4.2, the total TE field propagating through the uniform slab region can be expressed as a weighted superposition of the eigenmodes of the slab waveguide. The effective index of each eigenmode can be interpreted as a propagation angle [14]. The eigenmode with an effective index equal to the effective index of the silicon slab corresponds to a 0° propagation angle relative to the z-axis.

Figure 2.3 (e) shows the angular spectrum of the radiated TE beam for three different biofilm thicknesses of 0nm, 10nm and 20nm. It is observed that there is a distinct shift in the angular spectrum of the radiated TE beam as the biofilm thickness increases. The principal angular direction of the radiated TE beam is observed to decrease as a result of the increasing biofilm thickness. This result agrees with the decreasing radiation angle observed in Section 2.3.

Therefore, it is clearly evident from these results that the application of biofilm on the waveguide taper surface has the effect of changing the principal angle of propagation of the radiated TE Gaussian beam.

2.4.4 Fourier transform of the TE beam via a Lens

If the radiated TE beam observed in Section 2.4.3, is propagated through a planar lens structure, it is expected that the broad Gaussian beam incident on the lens will be focused to a narrow Gaussian spot at the focal plane of the lens. It is hypothesized that based on the Fourier transformation properties of the lens, any angular shifts in the incident TE beam, caused by biofilm deposition on the taper waveguide, should result in a spatial shift of the focal point of the beam. If an output waveguide is positioned at the focal plane to collect the power in the focused beam, then this spatial shift in the beam should consequently alter the amount of power coupled into the output waveguide.

The lens width was designed to be 300μm, which is about double the maximum TE beam width, so that the entire TE beam propagates through the lens. Using

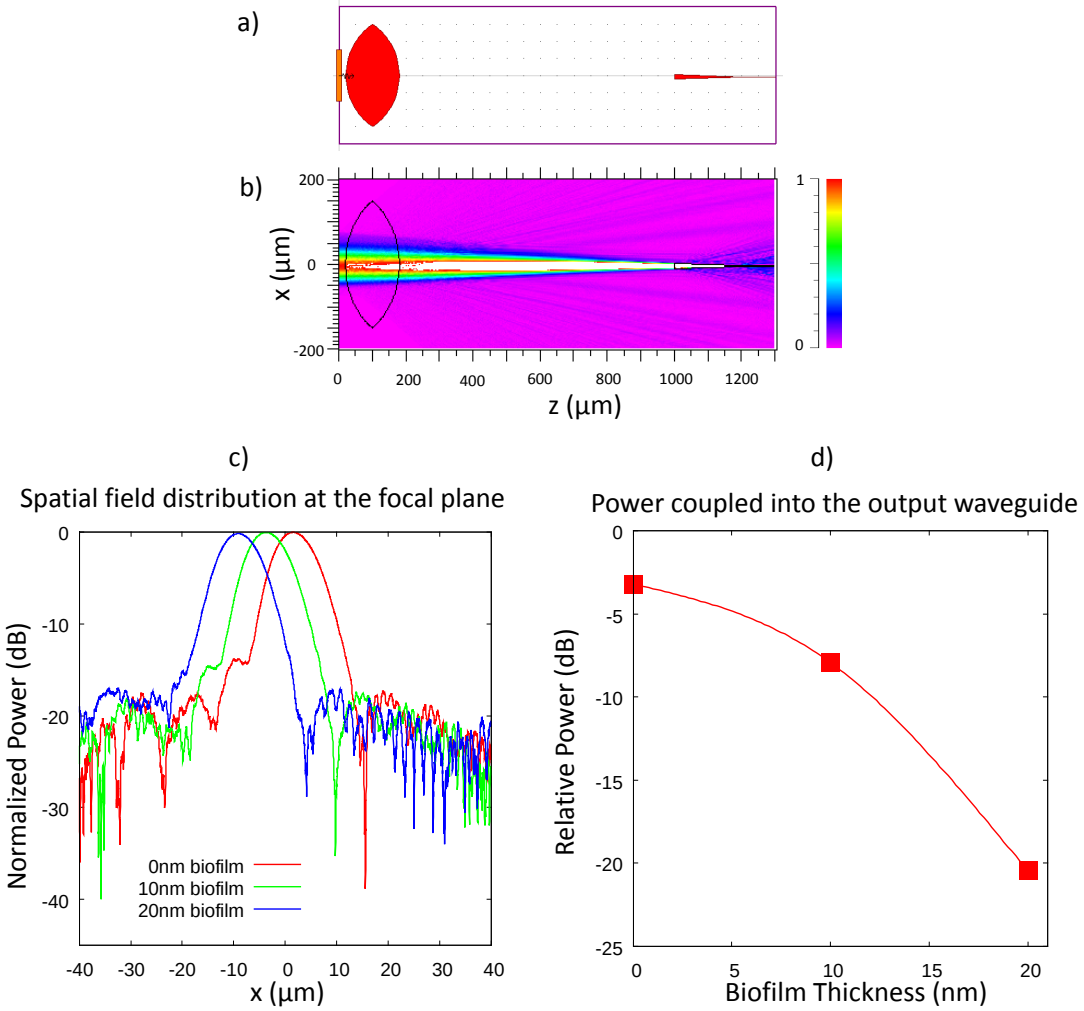

Figure 2.4: (a) Lens and output waveguide simulation window. (b) Shows the TE beam propagating through the lens and focused onto the focal plane of the lens where the output waveguide aperture is positioned. (c) Spatial field distribution of the TE beam at the focal plane for various biofilm thicknesses. (d) The relative power coupled into the output waveguide as a function of biofilm thickness

simple lens equations [41], the radius of curvature was set to 180μm so as to give the lens an approximate focal length of 1000μm. This long focal length improves the depth of focus for the TE beam [41], which aids efficient coupling into the output waveguide. The etch depth of the lens structure and the output waveguide is equal to 50nm which is the same as that of the waveguide taper. As discussed in Section 2.4.2, the lens was simulated in 2D, since only the propagation of the TE polarized beam through the lens was being investigated. Figure 2.3 (a) shows the 2D simulation window.

To evaluate the power coupled into the fundamental mode of the output waveguide, the overlap integral was taken between the TE beam at the focal plane and the fundamental TE mode of the output waveguide. The output waveguide aperture was 10μm which is equal to the width of the focused TE beam. The output waveguide is aligned with the focused TE beam when there is no biofilm on the waveguide taper.

Figure 2.3 (b) shows the 2D field plot of the TE beam propagating across the lens structure for the scenario where there is no biofilm on the waveguide surface. It is observed in this plot that the TE beam is launched perpendicular to the lens and propagates parallel to the z-axis. After crossing the lens the TE beam width begins to decrease monotonically as the beam is focused. At the output waveguide, the TE beam is incident across the aperture of the waveguide and it is observed that most of the beam is coupled into the aperture of the waveguide.

Figure 2.3 (c) shows the spatial field distribution of the TE beam across the focal plane of the lens where the output waveguide aperture is located (z=1000μm). The focused TE beam field at the focal plane is plotted for three different biofilms of 0nm, 10nm and 20nm thicknesses. It is evident from this plot that there is a spatial shift of the focused TE beam as a result of the deposition of biofilm on the waveguide taper. The spatial shift in the beam's position is approximately 5μm for both biofilm increments from 0nm to 10nm and 10nm to 20nm.

Figure 2.3 (d) represents the relative power coupled into the output waveguide as a function of the biofilm thickness. It is observed that for the zero biofilm case, the power coupled into the output waveguides is about -6dB. This is likely due to the mis-match between the incident beam and the waveguide mode. Figure 2.3 (d) shows that as the focused beam is shifted under the influence of an increased

biofilm thickness, the power coupled into the output waveguide is decreasing following the Gaussian profile of the focussed beam. This may be due to the fact that the biofilm range being observed is relatively wide.

These results therefore show that by utilizing a lens structure, it is possible to transform the angular shift in the wide TE beam observed in Section 2.4.3 into a spatial shift of the focused TE beam in the focal plane of the lens. This shift consequently alters the amount of power coupled into the output waveguide. This leads to a direct relationship between the biofilm thickness and the power in the output waveguide. Importantly, there is a 20dB change in output power for a 20nm change in biofilm thickness.

2.4.5 Wavelength dependence of power coupled to the output waveguide

In Section 2.4.4, it was shown that a lens structure can be used to spatially shift the focal point of the beam in the focal plane as a result of biofilm application on the waveguide taper. It was also shown that the amount of power coupled into the output waveguide would decrease as the focused beam shifts farther away from the waveguide aperture. However, the measurement of absolute power is not a reliable technique of monitoring changes in the biofilm thickness on the waveguide taper. Fluctuations in this absolute power can be caused by other factors such as changes in TM-TE coupling as well as by absorption.

To overcome such problems, a robust alternative to measuring optical power at the output waveguide is proposed. In Dalvand's WDM device concept [40], it was shown numerically that the power from the focused TE beam that is coupled into the output waveguide is wavelength dependent. This is due to the fact that changing the wavelength alters the radiation angle of the TE beam from the thin-ridge waveguide taper. This results in a spatial shift of the focused beam which alters the amount of power coupling into the output waveguide positioned at the focal plane. However, the waveguide taper sensor utilizes a single waveguide rather than several output waveguides as was the case for the WDM device concept [40]. It is therefore proposed that the application of biofilm on the taper should consequently shift the spectral response of the beam observed at the

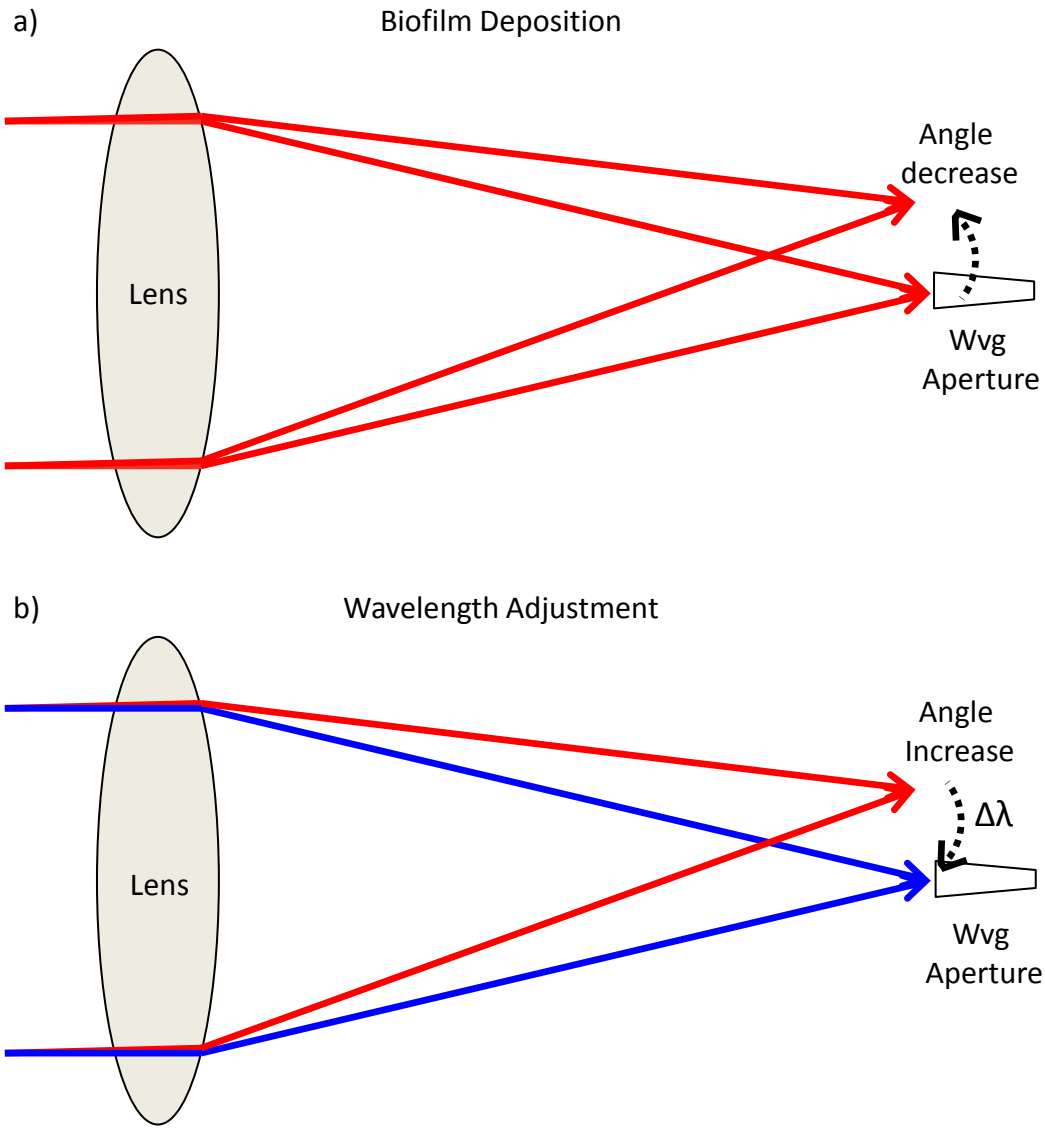

Figure 2.5: (a) Depicts the spatial shift in the focused beam as a result of biofilm deposition on the waveguide taper. (b) Depicts the expected TE beam spatial shift in the opposite direction as a result of wavelength adjustment.

output waveguide. Therefore, the wavelength shift in the maximal power coupled into the output waveguide can be used to monitor the quantity of biofilm deposited on the thin-ridge waveguide taper.

To evaluate the power coupled into the fundamental mode of the output waveguide as a function of wavelength, the overlap integral was taken between the TE beam at the focal plane and the fundamental TE mode of the output waveguide. This is the same method as outlined in Section 2.4.4. The power coupled into the output waveguide was then evaluated as a function of the excitation wavelength. This was done for two scenarios, when there was no biofilm on the waveguide taper surface and when it was coated with 10nm of biofilm.

Figure 2.6 shows a plot of the power coupled into the fundamental mode of the output waveguide in decibels as a function of wavelength. Two plots are shown for the case when there is no biofilm on the waveguide surface and for when it is coated with 10nm of biofilm. At 1.55μm, it is evident that the power coupled into the output waveguide is at a maximum for the uncoated taper. When the taper is coated, the power coupled into the output waveguide falls by about 3dB. However, as the wavelength is increased for the coated taper waveguide, the power coupled into the output waveguide increases to a maximum at about 1.56μm. This corresponds to approximately a 10nm wavelength shift for the 10nm of biofilm coating.

Figure 2.6 shows that there is distinct shift in the peak-power wavelength, which is a direct result of the biofilm coating that was deposited on the waveguide taper surface. It may be possible to enhance the sensitivity and extinction ratio of the sensor response by utilizing a longer taper to generate a wider TE beam with a narrower angular spectrum. The result would be a narrower waist of the focused beam and therefore a smaller width waveguide can be used at the output. A shift in angle as previously observed would result in a lot less power being coupled into the narrower waveguide making it more sensitive. However, this enhanced sensitivity would come at a cost requiring a longer taper and wider lens and therefore a larger device footprint.

Be that as it may, by utilizing the excitation wavelength it is possible to track changes in the biofilm thickness atop the waveguide taper by monitoring the wavelength shift required to achieve maximum power coupling into the output

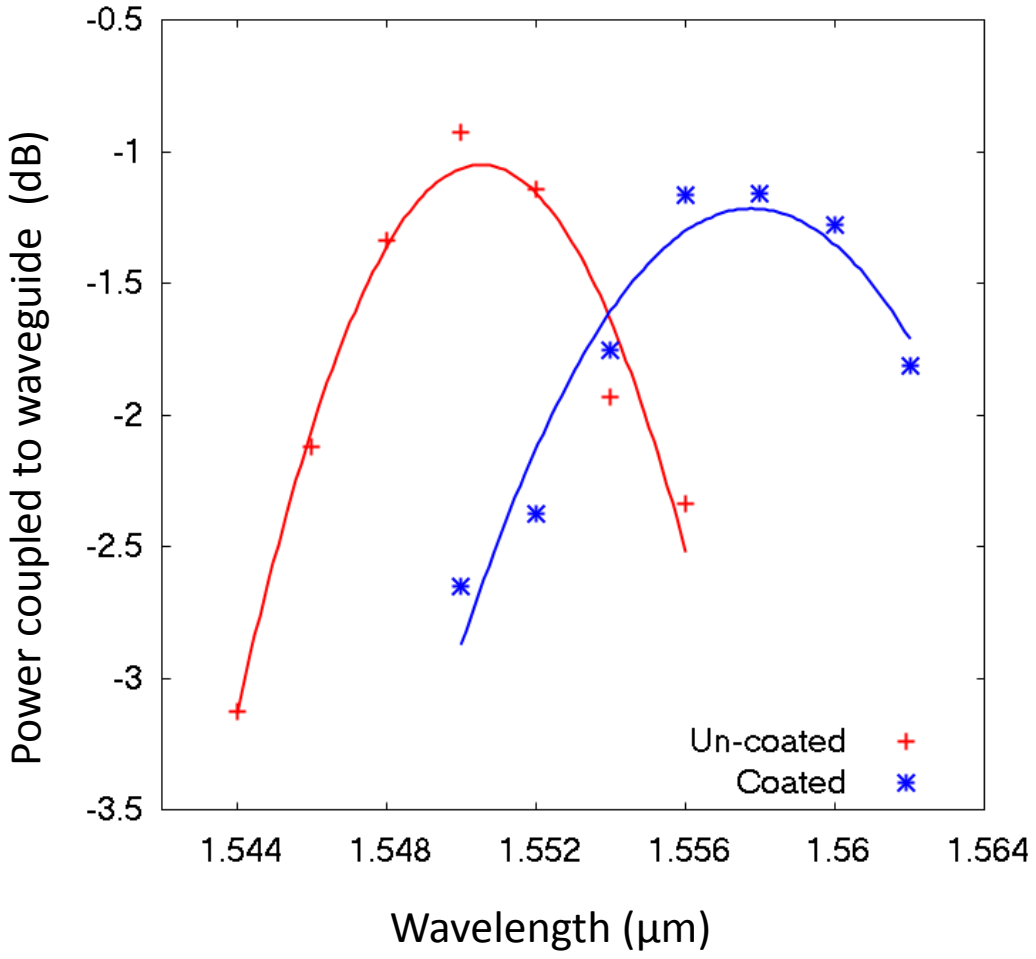

Figure 2.6: The power coupled from the focused beam into the fundamental mode of the waveguide as a function of wavelength for the uncoated scenario and when 10nm of biofilm coating is present.

waveguide.

2.5 Discussion

The numerical investigations done until this point have focused primarily on the transduction mechanism of converting a binding signal, caused by the deposition of biomolecules on the waveguide surface, into a measurable optical signal.

There are other important investigations that could follow such as interpreting the optical signal to extract the relevant binding signal again. However, crucial to the analysis of the proposed design of the tapered thin-ridge waveguide sensor in this chapter would be to experimentally verify the proposal through fabrication and characterization of the sensor. Such characterization would enable a realistic analysis of the device's sensitivity, limit of detection and even dynamic range which would be otherwise quite difficult to realistically estimate through simulation. However, it is possible to speculate on the factors affecting these sensor characteristics.

Noise

Interpretation: Noise is any signal that is received at the detector that is not due to the analyte. This can be due to random fluctuations in sensing optical carrier, or the materials responding to this carrier, or can be due to parasitic channels that arrive at the detector, but did not interact with the analyte.

- *Thin-ridge waveguide taper sensor:* Main source is parasitic channels because the beam is in free space, it is in principle possible for light that did not interact with the analyte to arrive at the detector.
- *State of the art waveguide sensors:* In ring resonator, MZI waveguide based sensors, parasitic noise is mitigated by light being confined to a single mode of the system only light that is guided in the fundamental mode arrives at the detector, and it can be guaranteed that this light has interacted with the analyte.

Sensitivity

Interpretation: Interpreted as the rate of change of signal at the detector with changing concentration of analyte.

- *Thin-ridge waveguide taper sensor:* Is dependent on the strength of the evanescent field which is enhanced by using the waveguide TM mode. Sensitivity is also dependent on the contrast between the highly evanescent guided TM mode and the tightly confined radiating TE mode. Sensitivity

is dependent on interaction length, which is single pass for the taper sensor. Increasing the taper length for example increases interaction length between light and analyte.

- *State of the art waveguide sensors:* Is dependent on the evanescent field strength of the waveguide mode, where TM is also primarily used. In MZI sensors, the sensitivity is also dependent on the contrast between the sensing arm and reference arms of the sensor. Interaction length is single pass in interferometric topologies such as MZI and multiple pass in resonant topologies such as rings. In MZI sensors sensitivity can be improved for example by increasing the length of the MZI arms. In ring resonators, interaction length can be enhanced by increasing the resonator Q-factor.

Detection limit

Interpretation: Interpreted as the smallest amount of analyte that can be detected. Ultimately, the fact that the analyte is formed of discrete, localized molecules must be considered. Would be dependent on both the sensitivity and the noise floor. Increasing sensitivity and decreasing the noise floor improves the detection limit.

- *Thin-ridge waveguide taper sensor:* In the regime of single molecules, improving sensitivity of a taper sensor, for example, by making it longer would not improve detection because of the inherent single pass interaction between light and analyte.

- *State of the art waveguide sensors:* In the regime of localized single molecules, increasing the length of an MZI to improve its sensitivity does not improve detection of localized molecules. However, for ring resonators, increasing Q-factor to improve sensitivity can enhance the detection limit of the sensor for localized molecules.

Dynamic range

Interpretation: Is taken to refer to the sensors linear range starting from the noise floor until saturation where the sensor response becomes non-linear.

- *Thin-ridge waveguide taper sensor:* In the taper sensor, the parameter that changes during sensing is the radiation angle which is defined by a sinusoidal function. The dynamic range would therefore be defined by the range from the noise floor to the peak of the sinusoid where signal changes become non-linear.

- *State of the art waveguide sensors:* In MZI sensors, the dynamic range is also defined by a sinusoidal function formed from the interference between the two arms of the MZI. Consequently, the dynamic range would also span from the noise floor to the peak of the sinusoid. In ring resonators, the dynamic range is dependent on the Q-factor or sharpness of the resonance peak as well as the free spectral range of the sensor.

From the above comparison, it appears that the taper sensor proposed in this chapter shares similar properties to an MZI sensor particularly in terms of sensitivity, detection limit and dynamic range. This is no surprise since both the taper sensor and the MZI reply on using the contrast between two sensing arms to detect refractive index changes at the waveguide surface. There is some difference, however, in the taper sensor noise characteristic. This can be attributed to the fact that the reference arm of the taper sensor is coherent radiation while the reference arm in an MZI is a fully confined waveguide mode. The collection and measurement of this radiation is thus more susceptible to parasitic noise compared to the collection of a well confined waveguide mode in the MZI.

An advantage of waveguide based sensors is that light is confined in a single-mode waveguide, which strongly limits the parasitic channels. In the TM lateral leakage sensor, this single-mode system is abandoned, and the signal is collected from a 2D free-space system. One may easily think that this system would therefore have plenty of room for parasitic channels in the form of light scattered from waveguide boundaries as well as edge reflections within the chip. These parasitic channels, which are effectively noise sources, may end up at the output of the system thus undermining sensor characteristics such as the dynamic range. However, such parasitic channels can be mitigated through k-vector or k-space filtering if the angular spectrum supported by the system is limited to a narrow range, for example by using a long aperture. Randomly scattered light in the

system having a broad angular spectrum would therefore be filtered out by the limited range of supported k-vectors within the sensor system. This may indeed be the case for the tapered waveguide sensor since only the collimated and coherent TE beam radiated by the taper, having a narrow angular spectrum, would be focused via the lens and end up at the output waveguide. Parasitic channels passing through the lens would be focused randomly at the output plane thus limiting the parasitic noise collected at the output. Other methods for filtering the beam in k-space could be for example using another tapered waveguide at the output since it would also have a narrow angular spectrum over which it can collect light from an incident beam. In fact any output structure that can discriminate based on k-vector or angle of incidence could plausibly be engineered into the TM lateral leakage based sensor.

2.6 Conclusions and Future Work

In this chapter, it has been shown that the lateral leakage phenomenon in thin ridge SOI waveguides can in fact be exploited for evanescent field biosensing. The deposition of biofilm on the waveguide surface has the effect of perturbing the strongly evanescent TM guided mode to a larger extent than the tightly confined TE slab mode. The result is that the phase velocity of the TM mode changes at a higher rate, resulting in its coupling to TE slab radiation propagating at a different angle. It is this change in the TE radiation angle that can be exploited to monitor variations in the biofilm thickness accruing on the waveguide surface.

A sensor topology was proposed that utilizes this lateral leakage phenomenon based on a thin-ridge waveguide taper, a planar lens structure and an output waveguide. It was shown that the taper radiated a TE slab beam at a specific principal angle and this angle varies as the thickness of biofilm on the taper surface increases. The planar lens structure was used to focus the TE slab beam to the focal point of the lens where an output waveguide was positioned. The TE beam was focused and coupled into the fundamental TE mode of the output waveguide. It was shown that as the angle of the TE beam changed under the influence of biofilm, the focal point to which the lens focuses the TE beam was spatially shifted. This means that the focused beam was taken out of alignment

with the output waveguide and less power was coupled into the output waveguide. In this way the power at the output waveguide was shown to vary with the biofilm thickness on the taper surface.

In addition to this, it was shown that by scanning the wavelength of excitation, the angle of radiation could be varied too. Consequently, the biofilm thickness which altered the TE angle of radiation also caused a spectral shift in the power delivered to the output waveguide. It was therefore shown that the taper and lens structure provides a direct relationship between the biofilm deposited on the waveguide taper and the spectral shift observed at the output waveguide. The wavelength shift at the output waveguide could therefore be used as a means of monitoring the biofilm accruing on the waveguide taper surface.

Further improvements can be made to this biosensing topology given that the overall device length of about 1mm is quite large. This is in comparison to other integrated sensing mechanisms such as optical ring resonators which for example can have a radius of 10μm plus additional input and output waveguides of a few hundreds of microns. This may necessitate a change in the sensor topology to exploit optical phenomena such as resonance to enhance the light-matter interaction at the thin-ridge waveguide surface. Increasing the number of waveguide walls in the sensor topology may also improve the TM-TE conversion efficiency. This may improve the compactness of the device and also enhance the sensitivity of the TM-TE coupling to evanescent field perturbations.

The analysed sensor utilizes a lens to collect the TE beam emitted by the leaky waveguide and focus it into the aperture of an output waveguide. This is effectively a means to filter the output based on the k-vector of the beam. A possible technique for reducing the overall size of the sensor would be to remove the lens and instead use another leaky taper to collect the collimated beam. It was shown in [14], that a tapered leaky waveguide could generate a highly collimated beam with a very narrow range of k-vectors. It should be possible to use such a taper to collect a collimated beam as well. It is conceivable that an array of tapers, each designed to collect a different k-vector TE beam could be placed side by side very close to the sensor and this would serve to direct the different k-vectors of TE beam to one or the other outputs of the various tapers. However, it should be noted that a simple taper will radiate or collect equally from both

sides and thus some further research would be required to establish a taper that could robustly and efficiently collect light from a single side only. However, as noted in [13], it is difficult to maintain single side radiation over a broad aperture and so further research would be required to pursue this opportunity.

Even if a lensed tapered waveguide could be designed, there is still a fundamental drawback of this sensor topology. The taper radiates a TE beam from both waveguide walls. However, only one of these beams is utilized for sensing purposed. The result is that half of the light is wasted by not utilizing the both TE beams. Furthermore, there is the possibility that this light may find its way back into the sensor resulting in parasitic effects. To overcome these problems, one may consider utilizing a dual waveguide setup, as was proposed in [13], where the separation and excitation phase between the waveguides is engineered to generate a single-sided TE beam from the coupled waveguide system. Such an approach may mitigate both light wastage as well as potential parasitic effects.

Due to the high thermo-optic coefficient of silicon, evanescent field biosensors such as ring resonators and Mach Zhender interferometers generally incorporate a reference arm which is used to compensate for temperature induced wavelength shifts in the sensing arm. The taper sensor could be sensitive to temperature. Like the ring sensor, it would be possible to have a reference taper that is not exposed to the analyte which could be used to calibrate against variations in temperature. Another possibility would be to try to engineer the sensor to be minimally sensitive to temperature. Some researchers have proposed athermal waveguides [36], however, these designs have been optimized over several waveguide geometric parameters to achieve waveguide properties that are minimally impacted by temperature over a modest wavelength range. To achieve something similar with these ridges, several waveguide parameters would be required. The simple ridge of Section 2.3 has only one parameter the ridge height, but it may be possible to introduce additional parameters, for example a dimple [44] and then optimize these properties to minimize temperature dependence.

Ideally to keep the response of the sensor simple and to maintain as high a contrast between the sensitive TM mode and the reference TE mode, the biofilm should be applied only to the surface of the ridge, with the side-walls and slab region protected. It is possible to fabricate the silicon ridge waveguide with side-

oxide covering the side-walls of the waveguide. This side-oxide layer is achieved by coating the waveguides with oxide SiO_2 and then planarizng the oxide revealing only the top-surface of the ridge. Such a configuration may be useful to consider for this type of sensor.

Chapter 3

Beam polarization rotator in thin-ridge waveguides

3.1 Introduction

The investigation in Chapter 2 looked into how the lateral leakage phenomenon in thin-ridge silicon waveguides could be exploited for evanescent wave sensing. It was predicted that the highly evanescent guided TM mode would be more susceptible to refractive index changes at the waveguide surface compared to the tightly confined TE slab mode to which it is coupled. Through simulation it was shown that surface refractive index perturbations affects the coupling relationship between the guided TM mode and the TE slab mode such that the radiation angle of the TE slab mode may be altered. It was also shown through simulation that a tapered thin-ridge waveguide in tandem with an integrated lens structure could be used as a sensor topology that exploits this TM-TE coupling relationship to measure refractive index changes at the waveguide surface in terms of a corresponding wavelength shift.

This chapter focuses on another attribute of the lateral leakage effect also based on the coupling relationship that exists between the TM guided and TE slab modes. Since these two orthogonal polarizations become intrinsically cou-

pled under the conditions of lateral leakage, there exists the possibility of exploiting this coupling relationship to convert from one polarization to the other. Essentially being able to realize polarization rotation, which can be TM to TE conversion or vice versa.

From a general perspective polarization rotators, quarter wave plates and polarizers are some of the key devices for controlling and changing the polarization state of light. Another crucial polarization controlling device is the polarization beam splitter (PBS). The ability to manipulate the polarization of light using these devices is extremely useful in optics and has been exploited in numerous applications, for example in polarization multiplexing (POLMUX), which has been used to increase the data carrying capacities in optical fiber links [45, 46]. Optical isolation can also be achieved by the use of non-reciprocal polarization rotators which aids in the attenuation of back-scattered and unwanted reflected light in an optical system [47]. In chemical and biological polarimetric sensors, these detect changes in birefringence caused by molecular adsorption [48, 49]. Polarimetric sensors of physical parameters such as strain have also been demonstrated in birefringent optical fibers [50, 51]. In imaging systems polarizers are used for viewing or filtering light of specific polarization [52, 53] that can yield vital information such as surface features [54] as well as in enhancing image contrast for remote sensing [55]. Polarization conversion systems employing polarizing gratings and quarter-wave plates have also been utilized to efficiently convert unpolarized light into linearly polarized light for use with liquid crystal displays [56]. In quantum optics, polarization encoding exploits the dual polarization states that a single photon can have to encode information in quantum bits also known as qubits. Consequently, polarization rotators and splitters are essential for quantum communication [57, 58]. These examples show some of the important roles that polarization control plays in optics today.

The integration of optical devices including polarization controllers into compact photonic integrated circuits (PICs) enables complex optical systems to be shrunk onto a chip . This is both cost and space effective compared to bulk optics. There is also the inherent stability the optical waveguide platform provides particularly for phase sensitive devices such as interferometers [58]. One example is in coherent receivers used for polarization multiplexing (POLMUX).

Coherent receivers contain multiple optical and electronic components, including polarization splitters, and through integration there is now a possibility of monolithically fabricating and packaging these devices into compact coherent receiver modules [45, 59]. Integration of polarization rotators [58] and splitters [57] have also been demonstrated for potential application in polarization encoding for on chip quantum computing and communication.

Silicon is one of the most desired optical materials for integration primarily because of its CMOS fabrication compatibility [2] which makes it a highly economical platform especially when considering the integration of optical and electronic circuits. Silicon-on-insulator (SOI) in particular is advantageous because it is a high index contrast platform which enables high mode confinement and low bending loss suitable for dense integration of photonic circuits [60]. Consequently, research into polarization controllers in the SOI platform has attracted extensive research interest.

One example is in implementing polarization diversity in silicon photonic integrated circuits (PICs). PICs in the SOI platform are particularly affected by high birefringence [61] due to the asymmetry of the SOI rectangular waveguide structure. Side-effects of birefringence include polarization mode dispersion (PMD), polarization dependent wavelength characteristics (PDλ) and polarization dependent loss (PDL) and these can lead to signal-to-noise ratio deterioration in phase sensitive PICs. Polarization insensitive photonic circuits are the key to overcoming these side-effects. Currently the most popular approach for achieving polarization independence is through polarization diversity technologies [62, 63]. Other approaches include using square shaped waveguides [64, 65] or through stress compensation [66] but these methods generally suffer from fabrication intolerance.

Polarization diversity technologies are composed of polarization beam splitters (PBS) and polarization rotators (PR) or combined polarization splitter-rotators (PSR). Polarization diversity technologies overcome the problem of birefringence in PICs by first splitting the randomly polarized input light from an optical fiber into two orthogonal polarization channels, TE and TM. One of the polarization channels is then rotated so as to be identical to the other, then both are sent independently into two identical PICs. This does away with the need for designing

PICs for the two different polarization states.

One of the most effective and novel solutions to this problem was demonstrated by Bogaerts et. al. [62]. They utilized a 2D-grating coupler to separate the light in an optical fiber into two orthogonal polarizations which are simultaneously coupled into the TE polarization of two separate waveguides that are perpendicular to each other. However, this solution is primarily targeted to situations where light originates from a fiber and needs to be coupled into a PIC through a grating coupler. This may represent a majority of the PICs today, but would not work if one is butt-coupling light into a chip. Another fact to consider is that only the TE mode is excited meaning PICs utilizing TM polarizations as in integrated sensing would still need polarization rotators to convert the TE polarized light to TM. Research into inline polarization splitters and rotators for polarization diversity would still be of great interest because there are and will be situations in photonic chips where light sources [1] and photo-detectors [67] are integrated to form complete PICs in which polarization control is still necessary.

While polarization diversity is an important application for which polarization splitters and rotators are sought, it is not the only focus of research into SOI polarization manipulation. Cutting edge research is also being undertaken to successfully deposit garnet on SOI waveguides to design Faraday rotators [47] which if realized would pave the way for integrated optical isolators and circulators. Nonlinear polarization rotation is also being exploited in silicon waveguides for the purposes of optical switching [68, 69] albeit this research area is still in its infancy with typical device lengths of several millimeters. The strong birefringence present in SOI waveguides also lends itself naturally to applications in integrated polarimetric sensing. Polarimetric sensors for measuring biological adsorption [48] as well as in measuring physical strain [50] have been demonstrated in optical fibers as discussed earlier. While integrated refractometric sensors have been well studied as discussed in Section 2.2, integrated polarimetric sensors that exploit the strong birefringence in waveguide platforms such as silicon appear to be an untapped area of research.

Therefore, there is clearly continuing interest in polarization manipulation in silicon waveguides and most research seems particularly focused on polarization rotation. This is not surprising since the high index contrast in SOI waveguides

would be expected to enhance the asymmetry between the TE and TM polarizations making polarization rotation difficult. It therefore becomes an attractive research proposition to look into polarization conversion when one comes across a phenomenon such as the lateral leakage effect where the TE and TM polarizations of a SOI waveguide structure are intrinsically coupled.

This chapter begins by reviewing SOI integrated polarization rotators to identify what are the important characteristics of polarization rotators. The investigation then considers what are challenges for polarization rotation using the lateral leakage effect. If it is indeed possible to utilise the lateral leakage effect for polarisation manipulation, then the question arises - what sort of structure could be utilized to achieve this polarization rotation and how can it be simulated to demonstrate this effect? The efficiency of the polarization rotating device is considered as well as what improvements can be made to increase this efficiency.

3.2 Review of SOI polarization rotator technologies

There exist several types of SOI integrated polarization rotator technologies that can be broadly grouped according to the polarization rotation method. Some techniques for achieving polarization rotation include mode coupling [70–74] as well as adiabatic tapering [75, 76]. There is also a class of polarization rotators that rely on changes to the waveguide geometry which enables excitation of hybrid mode polarizations [77–88]. A majority of polarization rotators, particularly in the silicon waveguide platform, fall within the above general categorizations. Let us consider the advantages and shortcomings of these existing types of polarization rotators.

3.2.1 Mode coupling

Evanescent mode coupling has been exploited to couple TE-TM polarizations between adjacent waveguides with varying structures utilized to phase-match the two polarizations.

Yue et. al. [70] proposed a three waveguide structure composed of two single mode rectangular waveguides and a larger square multimode waveguide structure. One of the smaller waveguides is positioned atop the square multimode waveguide and the other to the side. The higher order TE_{01} mode of the large square waveguide provides a short intermediate coupling path between the TE and TM polarizations of the two smaller waveguides. This structure yielded a polarization rotator with a relatively short length of 21μm, however, the three waveguides were vertically and horizontally offset making it a complex topology from a fabrication point of view. The reported polarization rotation efficiency was greater than 90% over a 68nm bandwidth.

Liu et. al. [71] demonstrated that by using two adjacent photonic wire waveguides, the corresponding widths can be engineered so that the TM mode in a 600nm wide waveguide can be coupled across to the TE mode of a 333nm wide waveguide. The TE mode in the input waveguide is not phase matched to any modes in the adjacent waveguide and therefore remains within the input waveguide. Consequently, not only is polarization rotation obtained but also polarization splitting is simultaneously achieved to make a polarization splitter-rotator (PSR) device. While this device is only approximately 45μm in length, adiabatic tapers are necessary for coupling from standard 450nm wide waveguide to the polarization coupler which increases the overall device length. The reported insertion loss (IL) was less than 2dB over a 60nm bandwidth and had a polarization extinction ratio (PER) of 12dB. Recently, researchers have devised and simulated similar concepts for mode polarization cross-coupling between adjacent waveguides of various types to make a PSR. This includes coupling between wire and slot waveguides [72, 73] as well as between rib waveguides [74], which all had simulated operational bandwidths under 100nm.

A significant advantage of using the mode coupling technique for polarization rotation is that it is also possible to achieve polarization splitting simultaneously within the same device. This can be beneficial particularly for implementing polarization diversity in PICs. The insertion loss is also generally very low due to the lack of significant scattering interfaces within the waveguide. The drawback however is that the mode couplers are phase sensitive and are optimized to have a specific optical length at a specific wavelength. Consequently, the bandwidth

of operation cannot be large. Because of the sensitivity to phase, the fabrication process needs to also be precise so as to attain good polarization extinction ratios.

3.2.2 Adiabatic Tapering

Ding et. al. [75] demonstrated that by adiabatically tapering out a strip waveguide, it is possible to convert the fundamental TM mode into the first order TE mode while preserving the fundamental TE mode. They used a 2×2 multimode interference coupler to separate the fundamental TE mode to one output while the first order TE mode is converted into the fundamental TE mode at the second output waveguide. Consequently, both polarization conversion and polarization splitting can be obtained with this cascade of devices. The device length was approximately 30μm without including the adiabatic tapers leading into the device. The insertion loss was better than 2.5dB across a 100nm bandwidth but suffered from poor cross-talk between the output waveguides at -12dB. The use of multimode interference also limits the device's bandwidth of operation due to its wavelength dependent behaviour.

Sacher et. al. [76] also recently demonstrated an adiabatically tapered polarization rotator and splitter. They utilized a bi-level taper to convert the fundamental TM mode of a wire waveguide into the first order TE mode of a rib waveguide over a length of 100μm. They then adiabatically coupled the first order TE mode into an adjacent wire waveguide while the fundamental TE mode was preserved throughout the entire structure. The insertion loss was less than 1dB across the entire bandwidth but the length of the entire structure added up to approximately 500μm.

Although adiabatic tapering has shown to yield low insertion losses combined with simultaneous polarization splitting and rotation, the device lengths can be quite large compared for example to mode coupling technologies. In addition to this, it is necessary that at the output the multiple waveguide modes generated in the conversion process need to be well separated, which usually requires strong index contrast and hence deep side-wall etching which could cause scattering loss. The potential benefit of thin-ridge waveguides as polarization rotators is that the polarization conversion process due to the lateral leakage effect does not require

any adiabatic tapering at all.

3.2.3 Mode hybridization

A large number of integrated polarization rotators can be classed as achieving polarization rotation through the excitation of hybrid polarization modes. These can be further functionally grouped into polarization rotators that operate through the use of asymmetric waveguides [77–82], through mode evolution [83–86] as well as through the use of hybrid plasmonic waveguides [87, 88].

3.2.3.1 Asymmetric waveguides

Polarization rotation using asymmetric waveguides was in use over 15 years ago [77] to overcome birefringence in polarization sensitive integrated GaAs waveguides and devices. Huang et. al. [77] utilized an asymmetric waveguide with one sidewall vertically tilted inwards thus rotating the polarization axis of the waveguide. With a specific choice of geometry and index contrast they showed that it is possible to rotate the polarization axes within the angle faceted waveguide by 45° with respect to the polarizations of the input rectangular waveguide. In this way, when a TE polarized mode is incident on the angle-faceted waveguide, its energy is distributed almost equally into the two hybrid polarizations of the angle-faceted waveguide. The result is that after half a beat-length, the two hybrid polarizations will have rotated by 90° and the TE polarization will now be a TM polarized mode when coupled back out to a rectangular waveguide. A maximum conversion efficiency of 96% was reported at a beat-length of approximately 750μm.

Continued improvements have been made in angle-faceted polarization rotators in recent years. Yamauchi et. al. [78] proposed an exaggerated angle-faceted waveguide designed in the shape of a triangle that is inline with a SOI square waveguide. Through optimization of the ratio between the input waveguide width and the triangular waveguide height, the insertion loss due to the mode mismatch between these two structures could be theoretically reduced to 0.5dB. It was also shown that the device length could be as little as about 2μm. Angle faceted waveguides, however, are not simple to fabricate due to the difficulty of ensuring

the correct slope and dimension of the angled waveguide edge.

The same principle of introducing asymmetry to a waveguide structure so as to rotate the polarization axis of the hybrid modes by 45° over a half-beat length has been applied in different ways but with emphasis on simplifying the asymmetric waveguide structure. This includes the staircase design where a small square section on a waveguide edge is etched away to from a staircase-like pattern [79, 80]. Jia et. al. [79] demonstrated a staircase design on a silicon waveguide with a square profile of 340nm width and surrounded by SiO_2 cladding. A small square section with a width of 180nm was partially etched into the edge of the waveguide. It was shown that a smaller partially etched section would decrease the insertion loss but would also increase the overall device length. Their device length of 3μm had a measured TM-TE polarization extinction ratio (PER) of 14.8dB and TE-TM PER of 13.3dB with an insertion loss 2.5dB.

Wakabayashi et. al. [80] proposed a similar staircase structure but applied at two opposite edges of a SOI waveguide which could potentially have even higher extinction ratios of more than 20dB. However, this means than one of the partially etched waveguide edges will be sitting under the waveguide which could be quite complex to try and fabricate. Velasco et. al. [81] also demonstrated polarization rotation using nano-slots of varying heights placed close to the edge of a SOI waveguide. The performance of their device with a length of 10μm was a PER of 16dB which is approximately similar to what was observed in the other publications. Fukuda et. al. [82] on the other hand added more material to the waveguide rather than etching it away so as to induce asymmetry and rotate the polarization axis of the waveguide. Their waveguide structure consisted of a transition from a square silicon core with a width of 200nm into a larger square silicon oxy-nitride core with a width of 840nm. While this structure addresses the issue of easier planar fabrication, the conversion efficiency was only 50% and the polarization rotation achieved was only 72° rather than the complete 90° for TE-TM or TM-TE.

The main advantage observed in these asymmetric waveguide structures for polarization rotation are the very short device lengths that can be achieved. However, the complexity of implementing such asymmetric modifications to silicon waveguides which already have nano-scale dimensions makes them difficult

to fabricate reliably. The bandwidth is also limited due to the half-beat length requirement of the polarization rotator which is wavelength dependent.

3.2.3.2 Mode evolution

Mode evolution is a technique first proposed by Watts and Haus in 2005 [83] as a technique for using tapered planar waveguide structures to adiabatically twist the polarization axis of a waveguide thus achieving polarization rotation. The example they utilized to illustrate this principle was two square 400nm waveguides sitting ontop of each other effectively forming a single waveguide into which a TM mode is launched. The lower square waveguide was horizontally flared outwards over the length of the structure until it formed a rectangular waveguide with a 800nm width while the height remained constant. The upper waveguide was in one instance tapered inwards and in another instance tapered inwards and separated from the lower waveguide. In both instances, the TM mode that initially occupied both waveguides transitioned into a TE polarized mode confined within the lower rectangular 800nm waveguide. The length of the structure determines the degree of polarization rotation that is observed, however, beyond a certain critical length, complete polarization rotation occurs. A significant finding from their simulations is that beyond this critical length, the wavelength dependence of the polarization rotation becomes insignificant. Therefore these types of mode evolution based polarization rotators can have a wide bandwidth of operation.

Chen et. al. [84] confirmed mode evolution polarization rotation using the same structure as in the Watts and Haus paper [83] but using a flared out silicon waveguide at the bottom. The upper waveguide was of Si_3N_4 which was inwardly tapered and shifted in a horizontal direction away from the the lower silicon waveguide. They demonstrated predominantly wavelength independent TM to TE polarization rotation as predicted with conversion efficiency of more than 90% across a 100nm bandwidth in a device 250μm long.

Zhang et. al. [85] demonstrated polarization rotation using mode evolution in strip and horizontal slot type SOI waveguides thus removing the necessity for the silicon nitride upper waveguide that was used in [84]. They demonstrated polarization rotation for both TM to TE and TE to TM with extinction ratios

greater than 14dB which is average from what has been reported in the publications discussed thus far. This conversion efficiency was only achievable for device lengths greater than 100μm.

A unique type of mode evolution was proposed by Chen et. al. [86] in 2014 where they utilized two ring resonators of different radii. The small ring resonator is positioned ontop of a larger ring resonator and it is offset so as to overlap with the bottom larger ring over part of its circumference. The structure thus forms a horizontal slot waveguide along part of its circumference where the rings overlap and this transitions to just the bottom resonator on the other half of the structure where they don't overlap. A TE mode can be evanescently coupled into the bottom ring resonator via a strip waveguide adjacent to the bottom ring resonator where there is no overlap. The TE mode in the bottom ring is then rotated into a TM polarized mode in the horizontal slot waveguide formed by both rings as it propagates around the dual ring structure. The now TM polarized mode can then be evanescently coupled out to a similar horizontal slot waveguide which forms the drop-port. Because of the ring structure, it is shown that the transmission spectrum of this polarization rotator has the characteristic repeating resonance peaks instead of a flat bandwidth. The PER as well as the insertion loss was shown to be relatively proportional to the slot gap and a gap of 20nm or less is necessary to achieve acceptable device performance. While this structure is rather complex, it is a novel example of mode evolution polarization rotation that manages to achieve both polarization rotation and polarization splitting within the same ring structure that is about 7μm in diameter.

The types of structures proposed for mode evolution are quite complex due to the necessity of ensuring adiabatic tapering of the hybrid mode and because of this can be relatively long with the exception of the ring resonator based polarization rotator [86].

3.2.3.3 Hybrid plasmonic waveguides

Hybrid plasmonic (HP) waveguides exploit the field confinement that occurs between a high index dielectric waveguide and a metal-dielectric interface to confine a field within a lower index dielectric region that separates the two guiding layers.

The benefit of this is tight field confinement with low loss dielectric propagation of the optical field compared to surface plasmon polaritons.

Hybrid plasmonic (HP) waveguides have been successfully utilized for polarization rotation. Caspers et. al. [87] utilized a HP waveguide composed of a silicon strip waveguide with a silver layer covering the waveguide and a low index silica film separating the two. The silver covering layer is initially deposited across the entire 180nm width of the silicon waveguide and is then tapered sideways until it is no longer atop the silicon waveguide. It was shown that a TM mode launched into this waveguide structure excites the hybrid plasmonic mode whose polarization axis is slowly twisted as the silver layer is tapered away. This is because the electric field remains orthogonal to the metallic interface. Consequently the mode emanating from this waveguide structure will be twisted into the TE mode of the silicon waveguide. While this device is similar in principle to the mode evolution method and was infact shown to have a wide bandwidth, the polarization rotator length was very short at 3.7μm.

Xu et. al. [88] simulated the use of a hybrid plasmonic waveguide based on the same principle as asymmetric waveguides to rotate the polarization axis of a slot waveguide. Using an aluminium strip carefully positioned at the top right-hand corner of the slot waveguide, they were able to excite hybrid polarization modes in the slot waveguide rotated by 45°. These hybrid polarizations were then propagated over a half-beat length so as to rotate the original waveguide polarization in the slot waveguide by 90°. The overall device length was 11.6μm with an efficiency of 97%.

Hybrid plasmonic waveguides have the potential of achieving very short polarization rotation device lengths as well as wide operational bandwidths if engineered well such as in the case of [87]. However, they require very careful placement of the metallic structures relative to the waveguide core to achieve the desired polarization rotation. This fabrication process can be difficult, leading to poor yields. Further, the introduction of metals to the waveguide structures can significantly increase absorption and scattering losses.

3.2.4 Summary

The plethora of current works in integrated polarization rotators found in the literature indicates that there is continued interest in the manipulation of polarization, particularly polarization rotation, in optical waveguides. This is especially important for the high birefringence introduced by the strong index contrast of the silicon platform. In the analysis of the current state of the art, it is apparent that there are some main aims in the development of polarization rotators. One is compactness of the device such that it occupies a smaller footprint on a silicon chip. Tolerance to fabrication errors is also of importance. High polarization extinction ratios and also low insertion loss are properties of good polarization rotators. A wider bandwidth of operation over which the device is functional is also preferred. Of significant importance is also the ease of design and fabrication of the polarization rotator as this can complicate and slow down the fabrication process. This gives preference for single rather than multilevel waveguide structures and it was found that single level polarization rotators were primarily those employing the mode coupling technique.

In light of this background on the importance of polarization rotation, the phenomenon of lateral leakage was considered for its intrinsic TM to TE polarization coupling characteristics. The lateral leakage process occurs without the need for hybrid integration with other materials or any other intricate manipulations of waveguide geometries which is characteristic of the majority mode hybridization techniques. The investigations in this chapter look into how one can efficiently couple between the TE and TM polarizations through the exploitation of the lateral leakage coupling effect in thin-ridge SOI waveguides. Through a search of existing research works, no similar report on this type of investigation has been done. Therefore, this is considered the first time this work is being reported.

3.3 Challenges in converting a TE polarized beam into the TM polarization

In the investigations of Chapter 2, it became apparent that in thin-ridge SOI waveguides, polarization conversion occurs when guiding a TM mode. At the waveguide walls the TM guided mode couples to TE slab radiation on both sides of the waveguide, which propagates at a specific angle to the waveguide. Since this TE slab radiation is highly coherent, it should be possible to couple to the TM guided mode if the waveguide is illuminated with a TE slab mode. This is simply because the mode coupling process is reciprocal.

However, a TE slab mode is an infinitely wide construct which is not practical in a real system. Generally, beams of finite spatial width are more practical forms of unguided propagation of light in a slab waveguide. So the question becomes whether one can couple a TE beam into the TM mode of a thin-ridge waveguide through the lateral leakage effect. A finite TE beam would have a finite angular spectrum and therefore the TE components propagating at angles not phase matched to the TM mode of the waveguide would not be expected to coupled into the waveguide. Therefore, only partial coupling from a TE beam into the TM mode of a waveguide with a specific width may be achievable in this manner.

In [14], Dalvand et. al. investigated how a thin-ridge waveguide taper guiding a TM mode could radiate bi-directional TE beams, of finite width, from both walls of the taper. In true reciprocity, if one wanted to couple backwards into the TM guided mode of the taper, it would mean two TE beams would simultaneously need to be incident on the waveguide taper. This is certainly not a trivial problem. The efficiency of this method would be dependent on factors difficult to control such as having the same TE beam profile launched towards the taper as that which the taper excites. The phase of both TE beams incident on the waveguide taper may also need to be precisely controlled.

In addressing this issue of practicality, a simpler approach was considered for coupling a TE beam into the TM polarization. Referring back to the idea discussed in Section 2.4.2 that a TE beam has a finite angular spectrum, it stands to reason that the efficiency of converting this TE beam into the TM polarization is dependent on converting a majority of the angular components contained within

the TE beam into the TM polarization. Since a single TM waveguide can only couple to one specific TE angular component, as was discussed in Chapter 2, a possible alternative would be to utilize several waveguides that span the range of angular components contained within the incident TE beam. However, in [13] it was shown that cascading even two TM waveguides to couple to the TE polarization is not a trivial task requiring precise control of the separation between waveguides. It was shown that the waveguides would need to be more than 5μm apart to reduce evanescent coupling between waveguides which affects the phase velocity of the TM mode in the waveguides and consequently the coupling angle to the TE slab radiation. This can lead to an overly large device footprint if multiple waveguides are required. Therefore, cascading several waveguides, enough to cover the angular spectrum of an incident TE beam can become an intractable problem using this approach.

However, a different approach would be to split the constraint of coupling a TE beam into the TM polarization in a thin ridge waveguide into two separate problems. One problem is the conversion of the TE beam into the TM polarization utilizing the lateral leakage effect. The other is efficiently coupling this new TM polarized light into a waveguide or some thin-ridge waveguide structure. In fact, in some cases, an unbound TM polarized field could be utilized without necessarily coupling into the guided mode of a waveguide. An example includes evanescent field sensing as was discussed in Chapter 2. A laterally unbound TM field would for example cover a larger surface area than a guided mode in a waveguide hence enhancing its interaction with surface environment perturbations. This TM field could also propagate without interacting with any etched silicon and thus should have exceptionally low propagation losses.

In this Chapter, the focus will be on the first problem of efficiently converting a TE polarized beam into the TM polarization. Structures for coupling unguided beams in a slab waveguide into a waveguide mode already exist [43] and will not be dealt with in this chapter.

3.4 Efficient conversion of a TE polarized beam into the TM polarization

This section starts with the question: how is it possible to efficiently convert a TE polarized beam into the TM polarization? The idea that a finite TE beam has a finite angular spectrum, highlighted in Section 3.3, is brought up again here. Each of these angular components of the TE beam can be thought of, through Fourier decomposition, as a TE slab mode with a specific angle of propagation. And all together these paraxial TE slab modes form the TE beam. This is simply restating the well known paraxial wave approximation [41]

Now consider a structure whereby as the TE beam propagates through it, each of the component TE slab modes in the TE beam are coupled into a phase matched TM slab mode. Since these two polarizations have different phase velocities in the slab they would have to be oriented at specific angles relative to each other in order to be phase matched. One can therefore imagine that each of the new TM slab modes generated from the TE components would be rotated by this same angle and together would also form a TM beam similar to the TE beam that traversed our conceptualized structure. This conceptual structure can be thought of as simply converting a TE beam into a similar phase matched TM beam. If this structure can rotate a majority of the angular components within the TE beam into the TM polarization, it would be expected to be very efficient.

A method for designing this conceptual structure that efficiently scatters an input light field into a preferential and predetermined output light field is not a new problem. Consider the interference pattern formed between an image/object beam and a reference beam. If it is preserved in some persistent medium, then illumination of this preserved interference pattern with the reference beam alone has the effect of regenerating the image/object beam including both its amplitude and phase in all three dimensions. This process is called holography. Holographic principles have been used for the design of planar integrated optic structures previously [89]. Peroz et. al. demonstrated how the transfer function of a spectrometer could be digitized and replicated using a 2D computer-generated hologram etched onto a planar waveguide. The spectrometer's spatial transfer function was essentially replicated by effective refractive index changes on the planar waveg-

uide. Illumination of the digitized hologram with an input field yielded the desired spectroscopic response. In this example the transfer function, or the effective refractive index perturbation that is the hologram, was obtained by taking the overlap integral between the input and output light fields. It is proposed that these holographic principles can be used to design a TE to TM converter based on lateral leakage.

Now consider two Gaussian beams confined to a silicon slab as depicted in Figure 3.1. One beam is confined vertically in the fundamental TE mode of the silicon slab, but is an unbounded Gaussian beam laterally, as shown in the lower and upper images of Figure 3.1 (a), respectively. The other beam is confined vertically in the fundamental TM mode of the slab but is an unbounded Gaussian beam laterally, as shown in the lower and upper images of Figure 3.1 (b), respectively. If the propagation axes of the two beams are oriented such that they remain in phase along the axis of the TM beam (the z-axis), the z-directed E field components will have a non-zero overlap where the two beams intersect. The product of the two fields will appear as the interference pattern shown in Figure 3.1 (c). Vertically along the y-axis , the pattern is strongest at the top and bottom silicon surfaces with a null near the center of the silicon slab. Along the z-axis the interference pattern has a Gaussian amplitude profile, however, along the x-axis the pattern has sinusoidal fringes with the Gaussian envelope of the two original beams.

Drawing on holographic concepts, it can be predicted that if a perturbation were implemented resembling Figure 3.1 (c), then illumination of this perturbation with a TE Gaussian beam with the same properties and angle of incidence as shown in Figure 3.1 (a) should generate a TM beam similar to Figure 3.1 (b).

3.5 Simplification of the holographically derived interference pattern

To test the hypothesis that illuminating a waveguide structure resembling the interference pattern in Figure 3.1 (c) with a TE beam would generate a TM beam, a rigorous numerical simulation first needs to be performed. The common

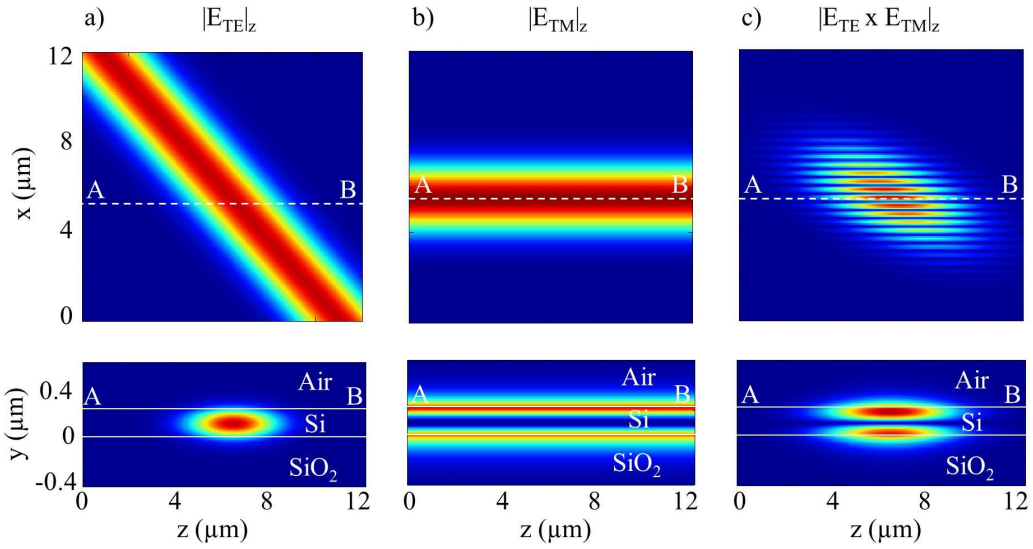

Figure 3.1: (a) The E_z field component of a TE Gaussian beam propagating at an angle. (b) The E_z field component of a TM Gaussian beam propagating in the z-axis direction in a SOI slab waveguide. (c) Shows the product of the two fields when they are phase matched along the z-axis.

options for modeling optical waveguide structures includes the finite difference time domain (FDTD) method, conventional and wide angle beam propagation methods (BPM) and the eigenmode expansion (EME) [42]. As was explained in Chapter 2, EME is advantageous for efficiently simulating TE-TM coupling in thin-ridge waveguide structures. It is computationally very efficient which is a problem when using FDTD for large 3D structures with fine features. The EME method also has no problems modeling fields with wide propagating angles as is the case for the BPM method. These advantages have made EME the preferential method for simulating lateral leakage in thin-ridge waveguide structures [14] and will be the simulation technique used in this chapter as well.

However, numerical simulation of a perturbation with the exact structure of the interference pattern of Figure 3.1 (c) would be challenging. This is because in EME the field within a waveguide structure is discretized into a finite set of eigenmodes that exist within the boundaries of the structure. Any field propagating within the waveguide structure can be decomposed into this set of eigenmodes

provided a sufficient number of eigenmodes are used. If there are variations in the waveguides direction of propagation, then the waveguide has to be subdivided into longitudinally invariant subsections. This is because each subsection has a different set of eigenmodes from the next. Therefore, the interference pattern seen in Figure 3.1 (c), which has continuous amplitude variations in the z-axis would have to be discretized. The accuracy of such a model would therefore be dependent on the resolution of this discretization. A high resolution discretization would consequently undermine the efficiency that EME provides over other simulation methods such as FDTD.

Thus, a number of approximations were made to simplify the waveguide perturbation based on the interference pattern in Figure 3.1 (c) to make it simpler to simulate using EME. The result is presented in Figure 3.2 (a). Firstly, the location of the perturbation was limited to the top silicon surface. The sinusoidal interference fringes were then approximated using a square function of two levels as shown in Figure 3.2 (c). It should be noted that these two levels are equally above and below the thickness of the open silicon slab. This is done to ensure that the average refractive index in the structure and the open slab are equal in order to minimize the effects of reflection and refraction. The envelope of the interference pattern was approximated as a simple rectangular step function as shown in Figure 3.2 (b).

The structure of Figure 3.2 appears to have the form of a grating. However, the grating is not periodic along the direction of propagation of the desired TM beam, but is rather periodic across the beams width. This is as expected since the TE and TM beams are inherently phase matched along the z-axis [10], however, the two beams are not phase matched along the x-axis. For efficient coupling to occur, the two beams should be completely phase matched across the entire interaction area and the grating oriented along the x-axis provides this additional phase matching. In order to be phase matched along the z-axis, the angle between the two beams should be

$$\theta = \arccos\left(\frac{N_{TM}}{N_{TE}}\right) \tag{3.1}$$

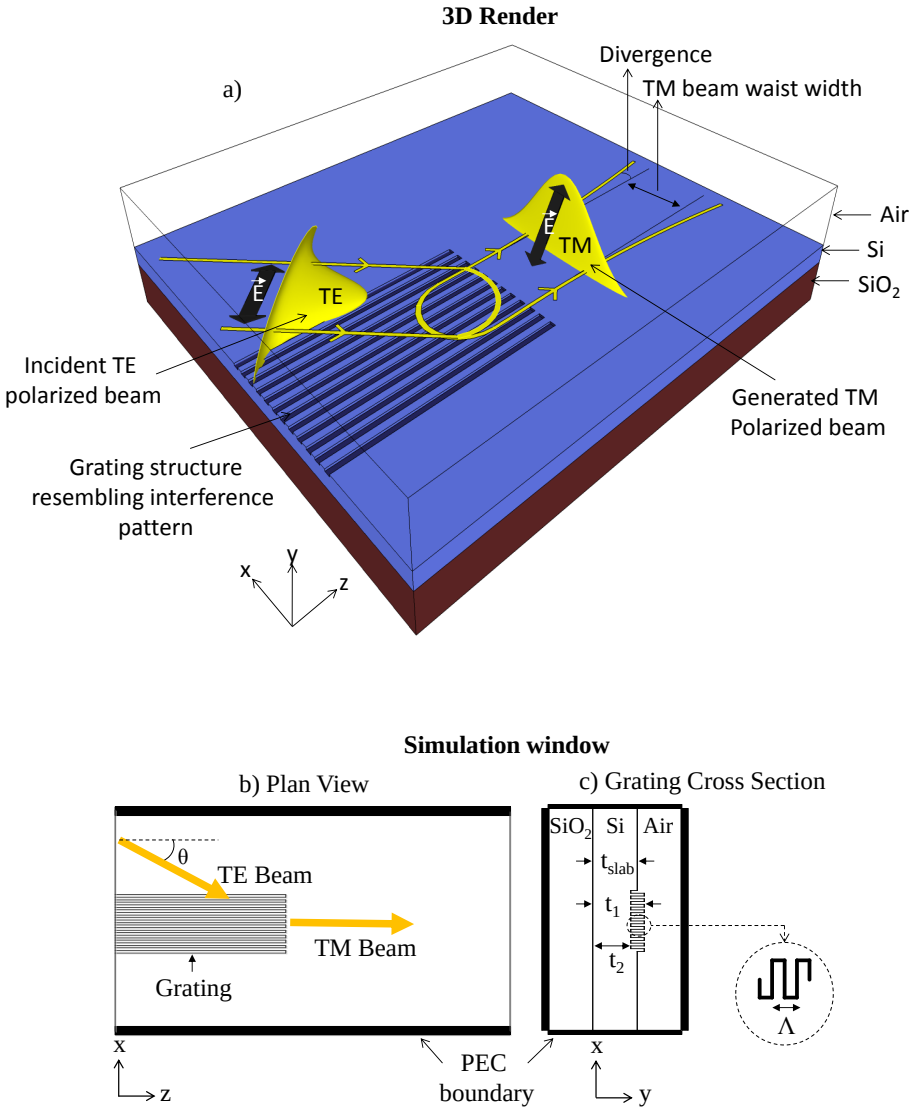

Figure 3.2: (a) 3D render of the device illustrating how a TE beam when launched towards the grating at a specific angle is coupled to a TM slab beam propagating along the z axis. (b) Plan view and (c) cross section view of the 3D simulation window. Here t_1=220nm, t_2=205nm and t_{slab}=212.5nm. The perturbation structure was designed to resemble the interference pattern of Figure 3.1 (c). The TE beam within the silicon slab is launched towards the grating at an angle θ.

where N_{TE} and N_{TM} are the effective indexes of the TE and TM slab modes respectively. At this angle, phase matching along the x-axis would require a grating of period

$$\Lambda = \frac{\lambda}{\sqrt{N_{TE}^2 - N_{TM}^2}} \tag{3.2}$$

where λ is the free space wavelength.

In hindsight one may deduce that it is possible to arrive at an equivalent solution for the grating parameters using conventional grating design methodologies by exploiting a k-space diagram. However, the grating orientation and profile would not be immediately obvious as was observed using the holographic design approach in Section 3.4. In a conventional grating, the periodicity of the grating is typically oriented in the propagation direction of the mode being coupled to. However, it was found in Section 3.4 that the grating profile required for a lateral leakage based polarization rotator is in fact oriented perpendicularly to the propagation direction of the mode being coupled to. This may not be immediately obvious or intuitive when using a k-space diagram approach in the grating design. Analysing the grating from a k-space diagram approach may yield additional insights but it appears that the design of the grating is more suited to a holographic design approach.

3.6 Simulation of a simplified holographically derived TE to TM coupler

Having predicted that a holographic grating similar to the pattern of Figure 3.1 (c) should convert a TE beam into a TM beam, and having simplified this pattern as shown in Figure 3.2, so that it could be effectively simulated in a SOI platform, this section uses rigorous numerical modeling to investigate the actual effect that the simplified grating would have on an incident TE beam.

Figure 3.3 (a) illustrates the cross-section of the grating. With N_{TE}=2.8058 and N_{TM}=1.8223 [10], the angle of incidence of the TE beam on the grating was calculated from Equation (3.1) as θ=49.5°. The grating period was calculated

from Equation (3.2) as Λ=726.5nm with λ=1.55μm. The width was set to 80μm to accommodate 32μm wide beams and thus the grating had 110 periods. The electromagnetic response of the grating structure was simulated using an in-house implementation of the fully vectorial eigenmode expansion (EME) method [90]. This is the same simulation method introduced in Section 2.4.2 for modeling lateral leakage radiation in a thin-ridge waveguide taper, which was covered in Section 2.4.3. To launch the TE beam into the simulation window, a canonical Gaussian TE beam profile rotated at an angle was expanded into the eigenmodes of the input slab waveguide structure.

Figure 3.3 (b) shows the x-directed component of the electric field, which corresponds to the TE polarization. Before interacting with the grating, the Gaussian TE beam remains unperturbed and well collimated. After entering the grating region the amplitude of this TE beam decays rapidly over the first few ridges and a pair of narrow reflected and transmitted TE beams appear to be generated when the grating terminates. Figure 3.3 (c) shows the y-directed component of the electric field, which corresponds to the TM polarization. There is no evidence of the TM beam until the TE beam strikes the grating. However the TM field is excited once the TE beam does interact with the grating. This is clear evidence of the conversion from TE-polarized field to TM-polarized field due to the grating. This TM beam is strong at the point where the TE beam strikes the grating, but rapidly decays within the grating region. The generated TM beam within the grating region continues to propagate once the grating terminates, but is very narrow and has an asymmetric profile causing it to diverge strongly when propagating over a long distance as shown in the inset of Figure 3.3 (c).

It is proposed that the narrow aperture of the TM beam is due to the strong, uniform grating used. When the TE beam is incident onto the grating, there is a sudden coupling of the TE field to the TM field. The amplitude of the TM field continues to increase due to continuous coupling from TE to TM. However, after a few periods, the TE field amplitude has reduced dramatically, due to strong conversion, causing the drop of TM field amplitude.

The apparent reflection of the TE beam in Figure 3.3 (b) is surprising as care was taken to keep the effective index of the grating equal to the slab. The most common cause of reflection is generally Fresnel reflection. This is caused when

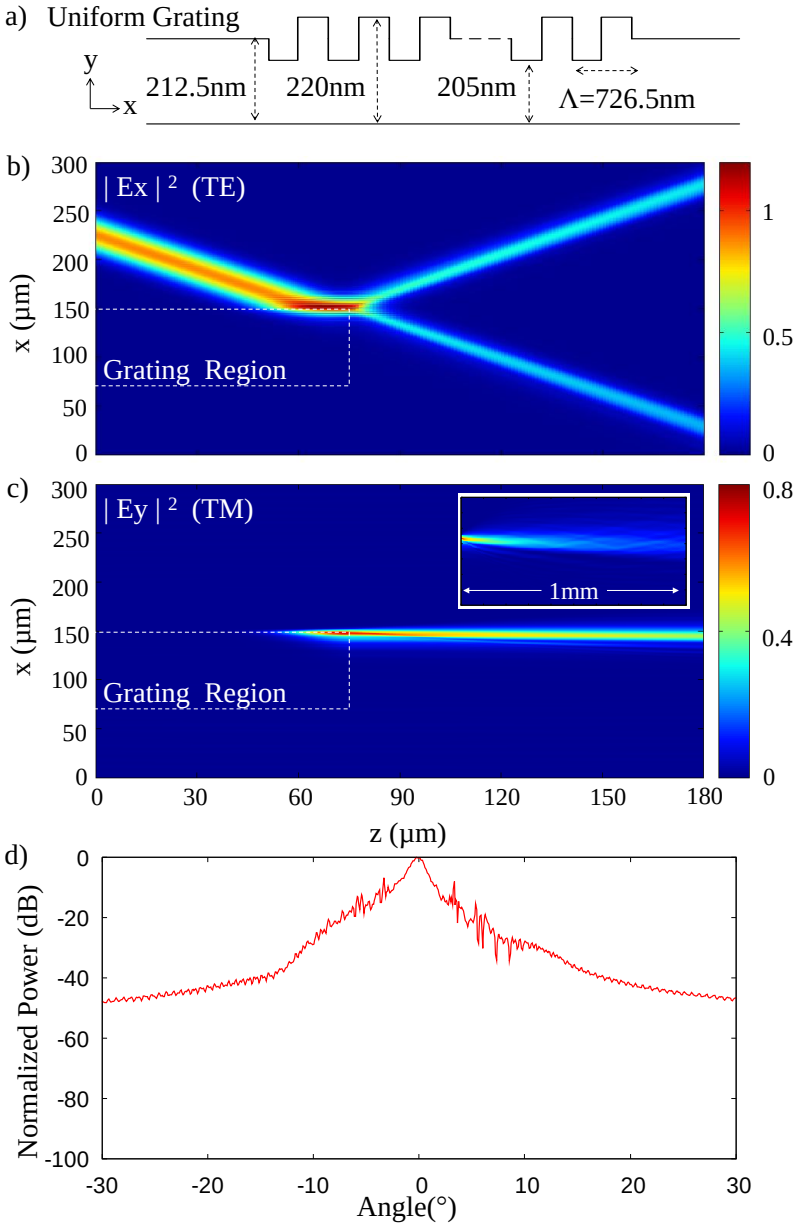

Figure 3.3: (a) Uniform grating profile; (b) x-directed E field, corresponding to the TE beam launched at 49.5°; (c) y-directed E field, corresponding to TM beam, Inset: TM beam propagating 1mm; (d) Angular spectrum of TM beam.

light propagates across an interface between regions of different refractive indices. However, the reflection strength seems too strong to be due to Fresnel reflection. An alternative is that the observed reflection could be due to Bragg reflection but this hypothesis would need further analysis which is deferred to the end of this Chapter. Yet another alternative explanation is that the observed reflected TE beam could be due to cascaded conversion of the TE beam to a TM beam (which are phase matched) and then back, from TM to TE (which are also phase matched). The fact that the reflected TE beam is narrower than the incident TE beam and is more like the generated TM beam supports this hypothesis. The fact that there is also an equivalent narrow beam propagating as a mirror image to the reflected beam also supports this hypothesis. This unexpected behaviour is of great interest, but is deemed peripheral to the current investigation. Hence, a rigorous examination of the cause of this observed reflection, is deferred to Chapter 4.

The collimation of the generated TM beam can be analyzed by examining its angular spectral properties. The total TM field propagating through the uniform slab region can be expressed as a weighted superposition of the eigenmodes of the slab. The effective index of each eigenmode can be interpreted as a propagation angle [14]. The eigenmode with an effective index equal to the effective index of the silicon slab corresponds to a 0° propagation angle relative to the z-axis. Figure 3.3 (d) shows the normalized TM field amplitude as a function of the angle of propagation exhibiting a broad peak centered at 0°. Like the field profile itself, the spectrum is also slightly asymmetric. The 3dB angular width was measured to be $\Delta\theta$=1.36°. The slope of the angular spectrum is also quite gradual with some noisy spectral components observed at around 5° on either side of the peak. This gradual slope indicates that the TM beam generated from the grating has a fairly wide angular spectrum in that a large proportion of its energy is propagating at relatively wide angles.

The results of Figure 3.3 show that, in principle, the grating of Figure 3.2 could convert a Gaussian TE beam into TM radiation, however, the TM beam produced was narrow and asymmetric leading to high divergence when propagating over a long distance. These qualities of the generated beam were attributed to the rapid conversion of the TE beam into TM within the space of only a few

periods of the holographically derived grating. Thus, only a small portion of the interference pattern encoded into the grating was actually experienced by the incident and converted beams. It is proposed that if the conversion can be achieved more gradually across the grating then the TM beam should be generated over a broader aperture and should hence have lower divergence.

3.7 Linear apodization of a TE to TM coupler

In Section 3.6 it was shown numerically that a TE beam can be converted into a TM beam using a uniform grating structure, but the generated beam was highly divergent due to the conversion occurring in a very confined region in the grating. It was proposed that the beam quality could be improved by apodizing the grating strength [91] such that conversion was distributed across all of the periods of the grating. This apodization would allow both beams to experience the full extent of the holographically derived grating, and thus create the expected broad, canonical aperture for excitation of the TM beam illustrated in Figure 3.1. Such apodization techniques have been used previously on many optical coupling structures including tapers, gratings and dispersion compensators [14, 91, 92]. It should be possible to vary the coupling strength of the grating by changing the duty cycle [91]. The ideal profile to achieve a collimated beam would be a Gaussian window. However it would not be effective to simply set the grating strength to match a Gaussian. This is because the excitation of the TM beam will be the product of both the grating strength and the amplitude of the TE driving beam which is reducing throughout the conversion process. As shown in [14], taking into account the fact that the excitation aperture will be the product of the profiles of the grating strength and the input optical beam, an approximately Gaussian aperture can be achieved using a simple linear increase in coupling strength. It is proposed that simply linearly increasing the grating strength will also produce an effective Gaussian apodization for the TM beam.

To test whether a linear apodization would improve the collimation of the generated TM beam, the uniform grating of Figure 3.3 (a) was replaced with an apodized grating. The coupling strength of the grating was apodized by linearly varying the duty cycle across the grating as illustrated in Figure 3.4 (a).

The grating period and width of the grating were kept as 726.5nm and 80μm, respectively. The duty cycle of the grating was linearly increased from 0% duty cycle to the maximum coupling strength at 50% duty cycle. The same approach described in Section 3.6 (utilsing the EME approach introduced in Section 2.4.2) was used to simulate the effect of illuminating the apodized grating when a TE beam is incident upon it at an angle of 49.5°.

Figure 3.4 (b) shows the x-directed component of the electric field. Unlike Figure 3.3 (b), the amplitude of the TE beam does not drop abruptly when the TE beam strikes the grating. Instead, it slowly decays as it propagates through the grating. At the end of the grating, very little power is left in the TE beam. Figure 3.4 (c) shows the y-directed component of the electric field, which corresponds to the generated TM field. Similar to the case of the uniform grating of Figure 3.3 (c), inside the grating structure, most of the power from the TE beam is converted into a TM beam. However, unlike Figure 3.3 (c), the TM field slowly increases in amplitude to a peak, then slowly decreases. The generated TM beam using the linear grating is much broader than that generated from the uniform grating. Also, unlike Figure 3.3 (c) the generated TM beam of Figure 3.4 (c) appears to be relatively symmetric and approximately Gaussian. The resulting TM beam can propagate over a long distance parallel to the z-axis in the silicon slab with low divergence as shown in the inset of Figure 3.4 (c).

The angular spectrum of the TM beam was evaluated using the same method as described in Section 3.6 (treating the effective indices of each of the modes excited as the angular spectrum of the beam). Figure 3.4 (d) shows the y-directed (TM) electric field amplitude as a function of the angle of propagation. The 3dB angular width was measured to be $\Delta\theta$=0.83°. In comparison to Figure 3.3 (d), a far narrower angular spectrum of the TM beam is seen to be launched from the apodized grating. It is also observed that the narrow spectral peak has rapidly varying, low level out of band features, which upon closer inspection appear to be sidelobes on both sides of the central peak.

Figure 3.4 (b) also shows that while most of the input TE beam has been converted to TM, there is still some small residual TE polarized light appearing as both transmitted and reflected TE beams. These beams are far broader and weaker than those observed in Figure 3.3 (b) which seems to indicate that the

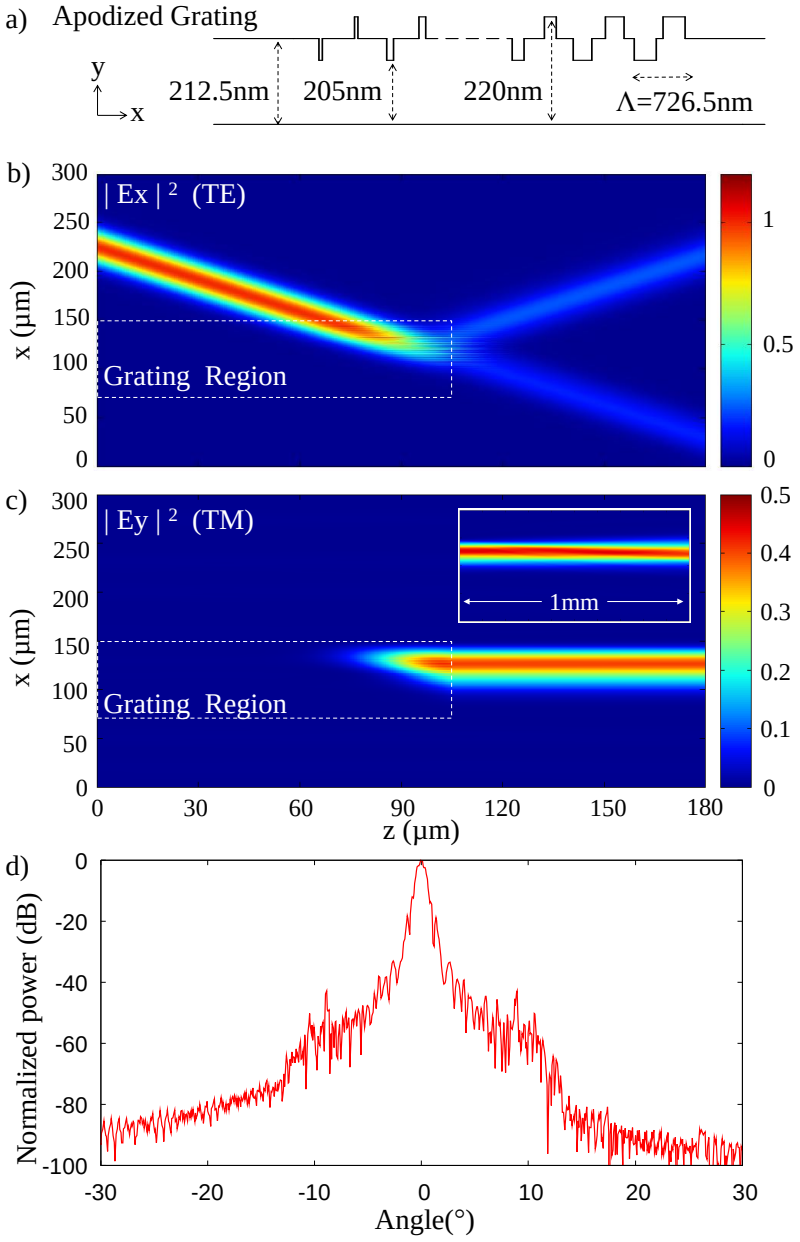

Figure 3.4: (a) Apodized grating profile; (b) x-directed E field, corresponding to TE beam launched at 49.5°; (c) y-directed E field, corresponding to TM beam, Inset: TM beam propagating 1mm; (d) Angular spectrum of TM beam.

apodization has had the desired effect. The reflected and transmitted TE beams appear to originate from within the grating, where the TM beam is strongest supporting the hypothesis discussed at the end of Section 3.6 that this may be due to cascaded conversion of the TM beam back to TE. Again, a more thorough investigation of these TE beams is deferred until Chapter 4. However, it would seem that the apodization has reduced the strength of these reflections. Hence, it may be possible to fully suppress these transmitted/reflected TE beams if the full form of the holographic apodization window of Figure 3.1 (c) were implemented. Testing this hypothesis would be difficult with eigenmode expansion and may be better suited to finite difference time domain. This simulation is proposed as future work.

In spite of this, the significantly improved TM beam proves the effectiveness of this simple apodization strategy. By utilizing an apodized grating structure, it is possible to generate a Gaussian-like collimated TM beam which propagates with minimal divergence when launched from the grating aperture. This is possible due to the the linear apodization of the grating which yields the Gaussian-like beam profile. This TM Gaussian-like beam was shown to be capable of propagating over a relatively long distance through the silicon slab waveguide.

3.8 Reduced strength linearly apodized TE to TM coupler

The simple apodization technique presented in Section 3.7 showed that a broad Gaussian-like TM beam can be generated from a grating coupler that is launched with minimal divergence from the grating's aperture. However, it was noted that the TM beam was generated almost entirely from the top half of the structure, with almost no interaction occurring in the bottom half of the structure. This would have the consequence of broadening the beam due to an effectively smaller aperture. It was also noted that the TM beam was a bit lop-sided with most of its intensity originating still from the top part of the grating structure, this may mean that the step response at the input edge of the grating may result in some spectral features (such as the broad spectrum shoulders observed in Figure 3.4).

It may be possible to avert this broadened beam and the broad shoulders by broadening the aperture over which the TM beam is generated and positioning the generated TM beam at the center of the grating away from the abrupt edges of the grating. This can be achieved by decreasing the apodization gradient such that the TE beam is coupled to the TM beam even more gradually.

In order to widen the aperture over which the TE to TM conversion would occur, the strength of the apodized grating was reduced by scaling the duty cycle proportionally across the whole grating aperture. The starting duty cycle remained unchanged at 0% but the maximum duty cycle at the end of the grating was decreased from 50% to a value of 30%. This effectively should decrease the slope of the change in duty cycle and therefore the apodization gradient. The conversion of a TE polarized Gaussian beam with this reduced strength grating was simulated in exactly the same manner as the investigation of Seciton 3.6 and the results are presented in Figure 3.5.

Figure 3.5 (a) shows the x-directed component of the electric field corresponding to the TE polarization. Figure 3.5 (b) shows the y-directed component of the electric field, which corresponds to the generated TM field. Similar to Figure 3.4 (c), it is evident that a Gaussian-like TM beam is generated in the grating coupler, which is shown in the inset figure to propagate with minimal divergence over a distance of 1mm. However, unlike Figure 3.4 (c), the TE and TM beams are seen to interact over almost the full width of the grating, and the TM beam is observed to be broader and centered midway between the walls of the grating coupler.

The angular spectrum of this TM beam is plotted in Figure 3.5 (c), which shows the y-directed (TM) electric field amplitude as a function of the angle of propagation. In comparison to Figure 3.4 (d), the pedestal of the central peak is smooth without any observable noise. The closest sidelobes to the central peak are 27dB below the main lobe. The 3dB beam width was found to be $\Delta\theta$=0.73°. Both the sidelobe level and the beam width are much lower than those of the TM beam generated from the uniform grating as shown in Figure 3.3 (d).

The reduction in the grating strength therefore caused the conversion of the TE beam to the TM polarization to occur at a slower rate. This resulted in a generated TM beam which has its peak located at a centralized position within the

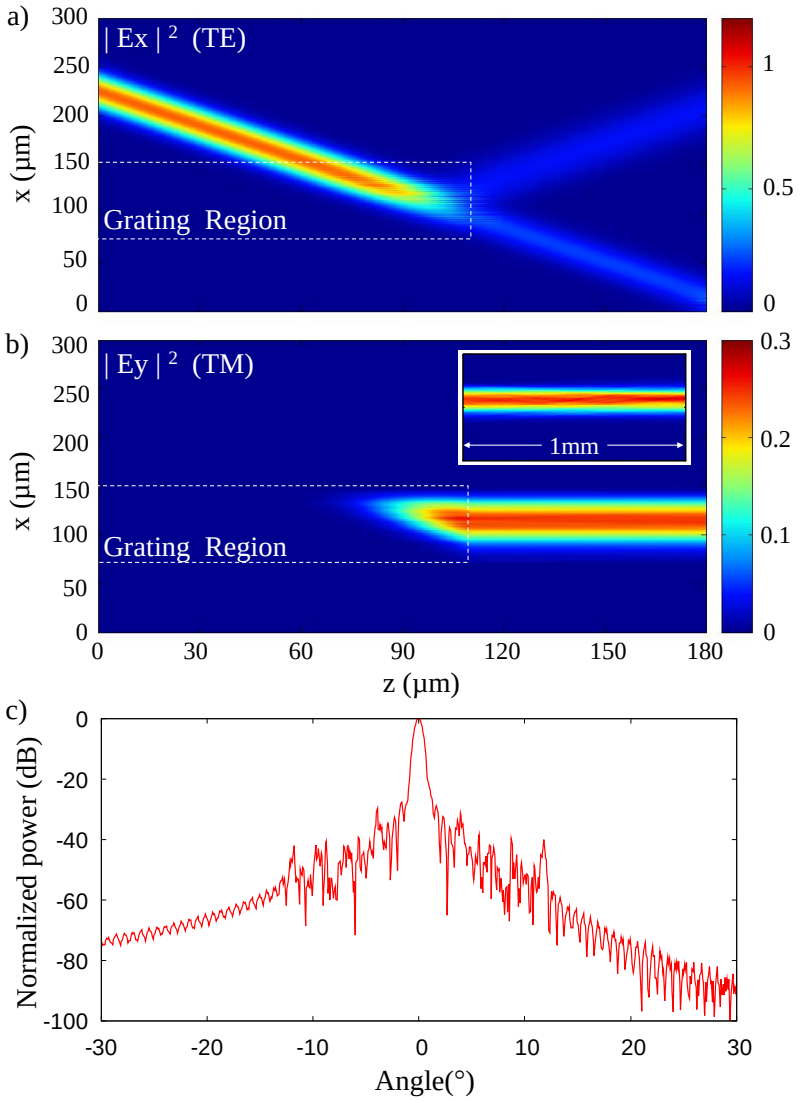

Figure 3.5: (a) x-directed E field, corresponding to TE beam launched at 49.5°; (b) y-directed E field, corresponding to TM beam, Inset: TM beam propagating 1mm; (c) Angular spectrum of TM beam.

grating coupler. Consequently, the TM beam at the grating aperture is broader resulting in less diffraction and a narrower beam.. Hence the TM beam would be expected to be more collimated when launched from the grating aperture.

3.9 Preliminary investigation of the grating's strong reflection behaviour

In this section, the reflection behaviour observed particularly in Figure 3.3 is revisited again. In Section 3.6 two possibilities were considered as to the likely causes of this reflection behaviour. One explanation is that the observed reflection could be due to Bragg reflection. An alternative explanation is that the observed reflected TE beam could be due to cascaded conversion of the TE beam to a TM beam (which are phase matched) and then back, from TM to TE (which are also phase matched). The latter hypothesis of cascaded conversion will be looked at in chapter 4. Here, the Bragg reflection question is explored briefly.

If the TE beam reflection in Figure 3.3 is a bragg effect, then the important requirement of phase-matching should exist for coupling to occur. A simple tool for analyzing the phase matching that a grating provides in k-space is conveniently illustrated using a k-space diagram [93]

Figure 3.6 shows a k-space diagram of the grating coupler whose k-vector K_{gr} is perpendicular to the gratings periodicity. The grating k-vector and consequently the gratings period is calculated from the grating equation;

$$k_{TEty} = k_{TEqy} - qK_{gr} \tag{3.3}$$

where K_{gr} is the grating's k-vector oriented in the y-axis, k_{TEty} is the k-vector of the transmitted TE beam in the y-axis, k_{TEqy} is the k-vector of the q^{th} diffracted beam in the y-axis where $q = 0, \pm1, \pm2, ...$ The grating period is evaluated from the grating k-vector as;

$$K_{gr} = \frac{2\pi}{\Lambda} \tag{3.4}$$

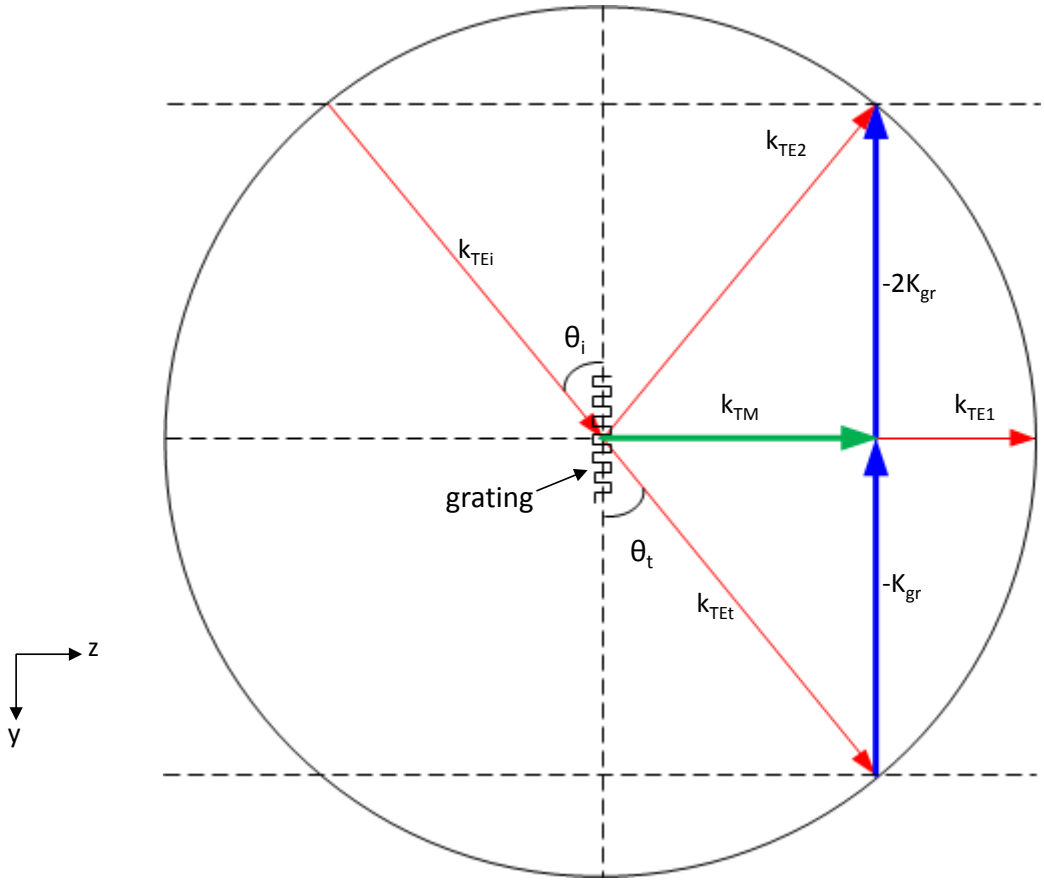

Figure 3.6: A K-diagram depicting the phase matching that the grating provides for an incident TE field. A TE beam k_{TEi} incident on the grating at an angle θ_i is shown to transmitted at an angle θ_t, equal to θ_i. The grating provides phase-matching in the y-direction to the first k_{TE1} and second k_{TE2} diffraction orders.

where Λ is the grating period.

Figure 3.6 illustrates that when a TE beam k_{TEi} is incident on the grating at an angle θ_i, it is transmitted at an angle θ_t which in this case is equal to θ_i since both are propagating within the silicon slab. The grating provides phase-matching in the y-axis to the first k_{TE1} diffraction order where $q = -1$ and the second k_{TE2} diffraction order where $q = -2$. Although the grating provides phase-matching to the diffracted TE beam k_{TE1} in the y-direction, coupling would not be expected to occur to this diffraction order since it has a greater phase velocity in the z-direction and thus not phase matched in the z-direction. However, the TM beam k_{TM} is inherently phase matched to the TE beam in the z-direction by choice of the launching angle of the TE beam. Consequently, the TE beam is phase matched to the z-directed TM beam in the y-axis by the grating and inherently in the z-direction by the TE beam's launch angle, and as seen in this Chapter, coupling does occur between the incident TE beam k_{TEi} and the z-directed TM beam k_{TM}.

Interestingly, the second order diffraction k_{TE2}, is observed to also be phase matched to the incident TE beam inherently in the z-direction and via the grating in the y-direction. Therefore, one can deduce from the k-space diagram that the grating provides phase-matching not only to the z-directed TM beam k_{TM} but also to the second order diffracted beam k_{TE2}, which is effectively a reflected beam.

Although the phase matching condition is met, this does not necessarily mean that bragg reflection would occur. A non-zero overlap is also required and the unit-cells of grating should couple in-phase to the reflected beam. An easy method for validating whether this grating would successfully provide coupling to the reflected TE beam via bragg reflection would be to perform a semi-vectorial simulation where only the TE polarization is used. Bragg reflection of the TE beam should be independent of the TM polarization.

Figure 3.7 (a) shows a TE beam launched towards the grating structure, similar to that of Section 3.6 at the same phase matching angle using a fully-vectorial simulation where TE-TM coupling is allowed. In this simulation, the grating structure is not truncated as in Section 3.6 but runs the full width of

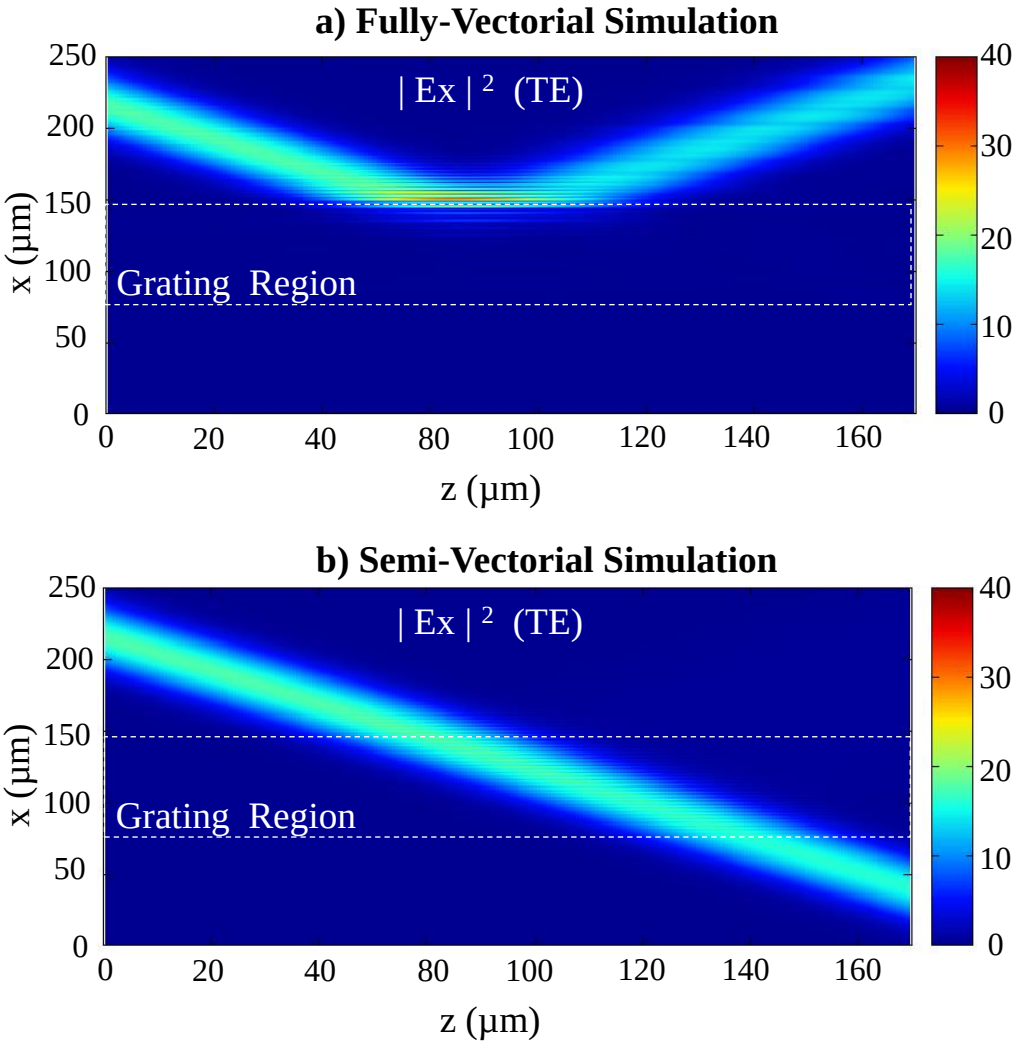

Figure 3.7: a) Fully-vectorial simulation of a TE beam incident on a thin-ridge waveguide grating. b) Semi-vectorial simulation of a TE beam incident on a thin-ridge waveguide grating.

the simulation window. It is evident from Figure 3.7 (a) that the TE beam is completely reflected.

Figure 3.7 (b) shows an identical scenario to that of Figure 3.7 (a), but this time using a semi-vectorial simulation where TE-TM coupling is prohibited by only utilising TE slab modes in the mode-solver. It is evident from Figure 3.7 (b) that the TE beam is not reflected as in Figure 3.7 (a).

It was expected that if bragg reflection had been the cause of the observed reflection behaviour, then the TE beam reflection would have occurred in both the fully and semi-vectiorial simulations since the Bragg reflection would occur independently of the TM polarization. However, this is not what was observed in Figure 3.7.

The result of Figure 3.7 therefore shows that the reflection behaviour exhibited by the thin-ridge grating structure is not due to Bragg reflection. This leaves the likely possibility that the reflection may be due to a TE-TM cascaded coupling phenomenon which will be the focus of Chapter 4.

3.10 Discussion

Comparing the proposed thin-ridge waveguide based grating polarization rotator to the state of the art.

Bandwidth

Interpretation: The wavelength range over which the polarization rotator maintains close to maximum efficiency.

- *Grating polarization rotator:* Is dependent on the wavelength range over which phase matching can be maintained between the incident TE beam and the excited TM beam within the grating region.

- *State of the art polarization rotators:* In mode coupling polarization conversion techniques, bandwidth is also determined by the coupling strength and coupling length of the structure which are interdependent parameters. For mode hybridization techniques, the bandwidth is dependent on the wavelength range over which the beatlength between the excited hybrid modes

maintains quadrature phase.

In summary, for conventional gratings, bandwidth is dependent on the grating strength or the grating length depending on the type of grating. One could hypothesize that the bandwidth of the proposed grating polarization rotator could also be dependent on the same parameters of length and strength of the grating. These parameters for controlling bandwidth could include the number of periods in the grating, duty-cycle and even apodization.

Efficiency

Interpretation: Is defined by the extinction ratio between the energy of the polarization entering the device to the remainder of the energy in the same polarization that was unconverted.

- *Grating polarization rotator:* A limitation to efficiency in the proposed polarization rotator was observed to be the topology of the polarization rotator. The rectangular topology used resulted in some back conversion from the generated TM beam back into the TE polarization.
- *State of the art polarization rotators:* In mode coupling as well as mode hybridization techniques the efficiency is generally highest at the center wavelength but decays away from resonance.

There may be the possibility of engineering the efficiency of the grating to have a flat response across its bandwidth based on the analogy to bragg grating structures since gratings can be designed to have a flat response over a broad wavelength range.

Polarization Splitting and Rotation

Interpretation: The ability of a device to perform both functions of rotating polarization as well as spatially separating the TE and TM polarizations.

- *Grating polarization rotator:* It is expected that the grating structure would not perturb an incident TM polarization but would rotate an incident TM polarization propagating in a different direction. There is thus a possibility here for both polarization rotation and splitting.

- *State of the art polarization rotators:* Mode coupling polarization rotators exhibit both the ability rotate as well as to split polarizations. Mode hybridization techniques generally exhibit only polarization rotation since the conversion occurs within a single hybrid waveguide.

There is therefore the opportunity here for additional research looking into the potential of simultaneous polarization conversion and splitting based on the proposed polarization rotator.

3.11 Conclusions and Future Work

At the beginning of this chapter, by reviewing existing literature, it was found that there is significant interest in polarization control particularly in integrated silicon photonic devices where birefringence is high. It was then proposed that the intrinsic TE to TM polarization conversion present in thin-ridge silicon waveguides could be exploited for the design of efficient polarization converting structures. The concept of holography was used to devise a structure that, potentially, could efficiently couple between phase matched TE and TM beams in a silicon slab waveguide based on the interference pattern formed between both polarizations.

The holographic interference pattern was implemented using thin-ridge structures on the surface of the silicon waveguide and it was observed that this pattern resembled a grating-like structure. A binary approximation of the interference pattern was made so as to simplify the complexity of the interference pattern to make it more suitable for numerical modeling of the structure. The eigenmode expansion technique was employed to simulate the coupling characteristics of the resulting grating structure. It was found that the grating structure did behave as predicted and successfully coupled an incident TE beam into a TM polarized beam. However, it was observed that the simulated grating structure which closely resembled the ideal interference pattern yielded a narrow and highly divergent TM beam.

It was proposed and shown through simulation that an apodization of the grating structure could be implemented to broaden the generated TM beam by slowly coupling the TE beam into the TM polarization. After reducing the steepness of

the apodization gradient, it was possible to generate a well collimated TM beam that could propagate for long distances within the slab waveguide with minimal divergence.

Following this proposal of a polarization rotator based on the latarel leakage effect, it would be important to first experimentally verify the behaviour of such a grating structure. The characterization of the lateral leakage based polarization rotator is also an important future work, both through simulation and experimentation. The investigation thus far has looked at a very specific state whereby the incident TE beam is launched at a precise angle toward the grating where it is phase matched perfectly to the TE slab modes of the structure. Therefore an important question is raised here. What effect does angular variation of the incident TE beam have on the polarization rotators efficiency? Similarly, what effect does wavelength variation in the incident TE beam have on the conversion efficiency? Also, what effect does the incident TE beam's spatial and spectral width have on the grating's conversion efficiency? Although the grating is designed to convert an incident TE beam to a TM beam,it is useful to also characterise the gratings behaviour when a TM beam, instead of a TE beam, is launched towards the grating. Similarly, what would happen if a TM beam was launched towards the output aperture of the grating? Would the grating's behaviour be reversed resulting in coupling to a TE beam in the same way that the TE beam was converted to a TM beam in the grating? Answering these additional questions would provide excellent material to analyse in a journal article on this new technique. This analysis is proposed for work in the very near future.

One application of this grating structure is as a polarization rotator of a TE beam into a TM beam. It may also be possible for this device to be used as both a polarization splitter and rotator (PSR). As shown in this chapter, the TE polarized beam would be strongly coupled to a TM polarized beam propagating at a different angle to the incoming beam. However, it is expected that if a TM beam is incident on this grating coupler at the same angle as the the TE beam, the TM beam should remain unaffected and should propagate through the grating mostly unperturbed. Consequently, it is expected that a TE and TM beam simultaneously incident on this grating structure could be split and the TE polarization rotated into the TM polarization resulting in two TM polarized

beams propagating in different directions.

Another application of such a device could be for evanescent field sensing as an enhancement to the structures investigated in Chapter 2. The sensitivity of the TM polarization to surface refractive index perturbations, as shown in Section 2.3, would be expected to significantly alter the TE-TM coupling characteristics within the grating. This would provide a means of probing environmental refractive index changes using the highly evanescent TM polarization in the grating excited by an incident TE polarized beam.

With regards to improvements to the grating structure, it should be noted that the structures investigated so far have been three-level waveguide structures. The grating structure contained both ridges above the nominal slab waveguide thickness and trenches which dipped below the nominal slab waveguide thickness. This multilevel waveguide structure could make the fabrication process more complicated by introducing several etch steps which also increases the likelihood of fabrication errors. The fabrication of a polarization rotating grating could be greatly simplified if a two-level grating structure could be devised that can be realized in a single etch step. Means for achieving such a two level grating can be conceived, but the investigation of these structures is proposed as future work.

Another avenue for improvement is the enhancement of the bandwidth over which this polarization rotator can function. As pointed out in Section 3.4 it is imperative to the operation of the polarization rotator, that the incident TE beam is phase matched to the TM beam. Due to the dispersive nature of the waveguide, significant changes in the wavelength of the incident TE beam could result in significant changes to its phase velocity which the grating coupler may not be able to compensate for. However, this can be mitigated by utilizing a more robust grating designed to cater for a larger bandwidth of the incident TE beam. One possible way of achieving this, still based on the holographic approach, would be to design the grating as was done in Section 3.4 but by including within the overlap integral wavelength variations of the input TE field as was done in the holographic spectrometer example [89]. Such an approach may yield complex grating patterns requiring the use of computer generated digitized holograms.

Perhaps the most surprising finding of this chapter is strong reflections of the TE beam observed in Section 3.6. It was shown that these could be reduced, but

not entirely suppressed through apodization. It was reasoned that this reflection could be due to cascaded conversion from TE to TM and then back to TE again, however further investigation would be required in order to be conclusive. Understanding how this reflection occurs will be of significant academic interest. Being able to harness, enhance and engineer this reflection could create new possibilities for integrated silicon photonic applications. Chapter 4 is dedicated to the understanding and exploitation of this reflection behaviour.

Chapter 4

Thin-ridge waveguide resonators and filters

4.1 Introduction

In Chapter 3, the inherent TE-TM coupling exhibited by the lateral leakage effect of thin ridge waveguides was considered as a possible avenue for realizing a polarization rotating device. Based on the principles of holography, it was proposed that a possible waveguide structure for achieving this polarization rotation could be derived from the interference pattern formed between a phase-matched TE slab beam and TM slab beam. It was found that a grating structure resembling this interference pattern could be used to convert a TE polarized beam into a TM polarized beam. A peculiar observation made during this exercise was a surprisingly strong reflection when the TE beam was incident on a uniform grating and to a lesser extent on an apodized grating. A good example of this unexpected reflection can be found in Figure 3.3. The unexpectedness of this reflection was due to the fact that the grating was designed to have an average refractive index similar to that of the slab in which the TE beam was propagating thus mitigating conventional Fresnel reflection. In the conclusion of Chapter 3, it was discussed how this reflection behaviour could likely be caused by resonant coupling from the incident TE beam to the TM beam in the grating structure and back into a TE beam due to the reciprocity of the coupling process. This reflection behaviour

was identified as a promising avenue for further research. To investigate this behaviour further, it is necessary to ask two questions. Firstly, what is responsible for the strong reflections observed in Chapter 3? Is it indeed resonance? And then, assuming that it is a resonance effect, what are the important applications of resonators and what features must these resonators have in order to be effective? To justify the investigation of this effect, the second question is explored first through use of a literature survey.

4.1.1 Applications of resonators

The significance of resonators in optics today can be identified by the multitude of applications that rely on optical resonators. One of the more common applications of resonators is in lasers where they form an integral part of the oscillation process [41, 94, 95] since they facilitate re-circulation of specific wavelengths of light providing resonant enhancement of the interaction photons at these resonant wavelengths with the excited gain medium. As sensors, optical resonators have been shown to be useful for biomolecular sensing [27, 96–98] as well as for monitoring biomolecular interactions [99] with applications in clinical diagnostics, drug discovery as well as detection of food-borne pathogens. Optical ring resonators [100–102], microdisk resonators [103] and photonic crystal cavities [104] have been shown to play a key role as optical filters for wavelength division multiplexing which is critical in telecommunications for achieving high spectral efficiency and throughput. Non-linear optical processes such as third-harmonic generation have been demonstrated in micro-resonators to enable wide-bandwidth continuous-wave generation of light [105]. Four-wave mixing has also been demonstrated in ring resonators for achieving all-optical wavelength conversion [106–108] as well as for optical signal regeneration [109] which are useful for fast optical signal processing. Optical modulation has also benefited from the use of optical resonators due to their smaller physical dimensions and enhanced efficiency for the specific resonant wavelengths [110, 111]. Of final note is the use of optical resonators for optical switching which can enable signal routing between single or multiple input and output optical interconnects [112, 113] for applications in wavelength selective switching or reconfigurable optical add-drop

multiplexing (ROADM). There are therefore a myriad of applications which have exploited the benefits of optical resonators.

However, the scope of this thesis is SOI thin-ridge waveguides and their applications. If it is possible that SOI thin-ridge waveguides behave resonantly, then the applications one could consider investigating are therefore those that best suit this SOI waveguide platform.

One could consider looking at SOI resonators for laser cavities because of the several advantages of using SOI as a platform for photonic circuits [114]. Developing lasers in silicon in comparison to other materials such as GaAs, InP and GaN is made very difficult by the fact that silicon has an indirect bandgap [95]. However, research into lasers for integrated SOI photonics has progressed over the years with demonstrated success using primarily hybrid integration techniques [115, 116] or through Raman amplification [117, 118]. The primary problems with SOI lasers appears to be focused more on how to achieve gain in silicon and less on the actual resonator cavities.

In optical sensing, the primary benefit of SOI resonator sensors has been identified as the compactness achieved while still remaining sensitive which allows dense integration of sensors on a chip as well as the possibility for opto-electronic integration [18]. However, in terms of sensitivity and detection limit, which are the primary parameters of importance in sensors, SOI ring resonators are outperformed when compared to other technologies such as dielectric microspheres [18] and silica microtoroids [119]. In addition to this, highly sensitive optical detection, for example in microtoroids, is performed typically at visible wavelengths around 600nm [120] where absorption from the normally water based sensing environment is minimal [121, 122]. However, at these visible wavelengths silicon is not-transparent [123] hence SOI sensors typically operate at telecommunication wavelengths [22, 28] where water absorption is higher [122].

Resonators for non-linear applications such as wavelength conversion in SOI appear to be of interest for signal processing purposes [107]. However, the main limiting factor for using silicon for non-linear applications is the two-photon absorption that occurs at the commonly used telecommunication wavelengths [124]. This has necessitated the consideration of other CMOS compatible platforms for non-linear applications [108, 124].

In optical modulation on SOI, resonators have been shown to minimize the physical size of modulators for more compact integration on the SOI platform in comparison for example to Mach-Zehnder modulators (MZM) [125]. However, one finds that the modulation speed performance of ring resonators [126] and MZM [127] are closely matched. With the advent of the Silicon Insulator Silicon CAPacitor modulators (SISCAP) [128] it is possible to achieve compact, non-resonant Mach-Zehnder modulators that can be driven with TTL voltages and this negates the need for further improvements in efficiency that might be offered by ring resonators.

For optical switching, The main types of integrated optical switches are those that use resonators [129] or those that utilize Mach-Zehnder Interferometers(MZI) [130] or both [113]. Similar to optical modulators it is observed here that ring-resonator based switches provide spatial efficiency due to their compactness. However, in terms of performance the switching speeds are not significantly different between the MZI and ring resonator optical switches. In addition to this, it has also been identified that ring resonator switches have to be tuned to compensate for fabrication errors and temperature variations [130].

Optical filtering is also an area of interest for SOI resonators particularly in wavelength division multiplexing (WDM) for high speed on-chip communication in the future [104]. At the moment, there are primarily four kinds of optical devices capable of WDM which are ring-resonators, lattice form filters, arrayed waveguide gratings (AWGs) and Echelle gratings [131]. Of these, ring-resonators have been identified as providing the most compact on-chip filtering solutions suitable for dense photonic circuit integration. A recent review paper paper [131] concluded that the main limiting factor of using SOI for WDM lies in the fabrication errors which limits cross-talk. Coupled resonator optical waveguides (CROW) were identified as an avenue for breaking this low cross-talk limitation, however, CROW devices may present their own challenges in terms of practical fabrication and environmental tolerance.

From the listed applications of resonators, it appears that the exploitation of resonators for laser cavities as well as for non-linear applications is not of paramount importance since the fundamental problems lie in other areas such as indirect bandgaps and two-photon absorption respectively. Optical sensors are

of possible interest but the high absorption of water at telecommunication wavelengths where silicon is transparent is a major limiting factor to attaining higher Q-factors and hence more sensitivity for silicon resonators. This leaves optical filtering, optical modulation and optical switching. Optical modulators and optical switches have been shown to mainly benefit in terms of compactness when using resonators. In fact, high speed and relatively compact modulators and switches in silicon have already been demonstrated using mach-zehnder interferometers. As for optical filtering, integrated SOI resonators are having a big impact in wavelength division multiplexing (WDM). They provide the most compact optical filters compared to other technologies such as gratings, which is important for dense integrated photonic circuits. Although fabrication of silicon resonators is error prone, current ring resonator technologies provide a means for enhanced filtering performance by cascading several resonators to form coupled resonator optical waveguides (CROW) with improved spectral performance. However, it is expected that the sensitivity of rings and the interfacing directional couplers creates challenges for their practical implementation. In summary, one can see that optical filtering for WDM is quite an important application for integrated optical resonators especially looking into the future.

With this in mind, we need to reflect back to the goal of the chapter which is to investigate the peculiar strong reflections observed in the SOI thin-ridge waveguide grating structures of chapter 3. Is it a resonance effect? If so, what are the implications or potential applications? It has been identified that optical filtering for WDM is an important applications of resonators worth investigating. Therefore, to guide this research, one must first consider what are the characteristics of a good filter or what are the important features in a filter? In light of this, what role do resonators play in optical filtering and what features must resonators have in order to be effective optical filters?

4.1.2 Review of integrated optical filtering

The four main types of integrated optical filters used for WDM are arrayed waveguide gratings (AWG), Echelle gratings (EG), lattice form filters composed of cascaded asymmetric Mach-Zehnder interferometers (AMZI) and ring resonators

which also encompasses cavity resonators [131]. It is evident from the above groups that there are filters that utilize resonant structures which is the ring resonator class and those that are non-resonant which are the rest. To identify what are the important features of optical filters one could first look at the non-resonant filters. Then to identify the role and effectiveness of resonators as filters one could then compare resonant filters to the non-resonant type of filters.

4.1.2.1 Non-resonant optical filters

In the paper [131] classifying integrated optical filters, Okamoto begins by highlighting an important fact which is that the free spectral range (FSR) of all the filters listed is inversely proportional to the path length difference parameter ΔL. ΔL in the AWG is the path length difference between adjacent waveguides in the array. In the EG ΔL is measured between two light beams reflected from adjacent reflection facets and in AMZI it is the minimum path length difference in the cascaded MZIs. Interestingly, although this is a slight digression, the ring resonator (RR) FSR bears a similar resemblance where ΔL or simply L is the ring circumference. This similarity is in fact not surprising if one considers that all the above filters utilize either spatial (AWG and EG) or temporal (AMZI and RR) interference effects [131]. The important point Okamoto highlights here is that this path-length difference is inversely proportional to the FSR.

For example, Takada et. al. demonstrated [132] a silica-based AWG with a heroic ΔL of 1.26cm. The FSR was only 16GHz and they could fit 16 1GHz(8pm) channels within this range with about -16dB of crosstalk between adjacent channels. The key to this achievement was that they utilized silica-based waveguides with a refractive index difference of 1.5% which allowed a tighter bend radius of 2mm. In the end, the device footprint occupied an entire four inch silicon wafer. This is obviously one extreme. A similar 1.5% refractive index difference silica waveguide platform was utilized by Hida et. al. [133] where they fabricated an AWG with a ΔL of 27.7mum yielding an FSR of 7.27THz. With a spacing of 25GHz they were able to fit 256 channels in this range with far-end cross-talk of -40dB and adjacent channel crosstalk of -20dB. Their device footprint was 74mm x 50mm. It is important to note here that the channel wavelength spacing

in an AWG is also inversely proportional to to the path length difference in an AWG but can also be changed by adjusting the star coupler dimensions [134]. Silica AWGs became industry standard filter devices for optical communications because of their several identified advantages [134] of design flexibility, stability, mass-producibility, low fiber coupling losses and low propagation losses.

Echelle grating (EG) filters in silica were also of research interest for WDM. Janz et. al. for example demonstrated a 256 channel EG demultiplexer with a 25GHz channel spacing which are the same specifications as Hida's AWG mentioned earlier [133]. In comparison, the EG device size was 20mm x 40mm which is almost a quarter the size of Hida's AWG but the insertion loss was -10dB which is 5dB worse. Interestingly, the adjacent channel crosstalk was -30dB which is 10dB better than in Hida's AWG. So why were Echelle gratings not highly adopted by industry if they performed equally if not better to AWGs experimentally?

This question is answered by looking to another important property of filters known as phase error [135]. Phase error is an intrinsic property of interferometric optical filters such as AWGs that adversely affects crosstalk performance. Phase error is identified as being caused by imperfections in a waveguide due to fabrication errors which causes fluctuations in the waveguide core size, the refractive index in the core and cladding as well as the actual waveguide length. This phase error is also referred to as effective index fluctuations [131]. In regards to Echelle gratings, Okamoto [131] indicates that the position of the reflection facet contributes to an Echelle gratings phase error. While experimentally it was possible to more precisely control fabrication errors, it was not the case in industry due to the lower fabrication resolutions used. Consequently, the actual achievable crosstalk in Echelle gratings was worse by more than 10dB in comparison to AWGs which led to an industry preference for AWG based WDM systems.

Inspite of these advancements in silica based WDM, Hibino pointed out [134] that to advance to high density integration of photonic circuits, it is imperative that the waveguide bending radius must be reduced. One approach identified for doing this was to transition to higher refractive index contrast waveguide structures. InP and SOI waveguides were both options for doing this. Barbarin et. al. for example [136] demonstrated an InP AWG with physical dimensions of 230x330μm^2. However, with an FSR of 12.8nm (1600GHz) they could only

fit four channels with 3.2nm (400GHz) spacing at 1550nm with crosstalk of just -12dB. In SOI Sasaki et. al. compressed an AWG to 70x60μm^2 using 450nm silicon wire waveguides with a path length difference of 6.06μm. They were able to achieve an FSR of about 85nm(10THz) with 11nm(1.4THz) channel spacing and cross talk of -13dB. It appears that although the physical size is significantly decreasing, in comparison to the silica AWGs, the spectral resolutions are getting much worse for these higher index contrast platforms. Even in 2013, 12 Channel SOI AWGs with channel spacing of 400GHz, dimensions of 560x350μm^2 and achievable crosstalk of -17dB is still normal [137].

Okamoto [131] explained these observations very well in his review for why this spectral resolution penalty is observed in the physically smaller but higher index contrast AWGs. Although the bending radius in silicon is 700 times smaller in silicon than silica, the device size cannot scale down by the same amount and still have the same spectral characteristics. This is because, for an interferometric filter such as an AWG, the device size is determined by the path length difference needed between the arms of the array as well as the number of WDM channels. If the AWG spectral characteristics are to stay the same, the requirement is that the optical path length difference must also stay the same. However, because the propagation length in silicon is about 50 times smaller than in silica, this means that the physical length can also be about 50 times smaller. Okamoto identified that another penalty of transitioning to the higher index SOI platform is that the path-averaged effective index fluctuation is 300-500 times larger than in silica waveguides which is why silicon AWG crosstalk is experimentally observed to be 15 to 20 times worse than silica AWGs.

Reflective AWGS (R-AWGs) in silica were first proposed in [135] as a way of addressing phase-error problems, which predicted about -40dB crosstalk in silica AWGS using techniques that agreed well with experimental results. In SOI, R-AWGs have also been implemented to try to improve on size and cross talk limitations [131, 138]. Using straight lower-loss rib waveguide R-AWG arms terminated with bragg reflectors [131] -20dB crosstalk could be achieved, which was good but in fact not better than existing SOI AWGs. However, R-AWGs have been identified as being the most compact topology for AWG filter implementations.

Echelle gratings (EG) in SOI also benefited significantly in size. Horst et. al. [139] demonstrated an SOI EG with a size of 600x170μm^2, 8 channels, a 1.8nm channel bandwidth and a channel separation of about 3nm(400GHz). The reported adjacent channel crosstalk was -19dB. More recently Lycett et. al. [140] demonstrated how chirped echelle gratings, with an area of about 800x500μm^2, can be utilized to engineer the filter passband for a flat response with a 1.2nm bandwidth. This is a significant improvement from previous echelle gratings that had a Gaussian-like passband response [139, 141, 142]. However, the drawback of this technique was that the roll-off factor remained the same and therefore the effect of flattening the spectral passband adversely affected the crosstalk between wavelength channels.

Lattice form filters using asymmetric MZIs (AMZIs) were also investigated in silica and then in higher index silicon waveguides. Kamei et. al. [143] for example fabricated a silica 4 channel AMZI filter with a chip size of 55x22mm^2 and was able to obtain 0.4nm (50GHz) channel spacing with crosstalk greater than -28dB. What is interesting about the AMZI filter is that the passbands are flat-topped and not Gaussian which means there is a relatively equal attenuation across all wavelengths in a given filter channel. In silicon, Horst et. al. [144] demonstrated an 8 channel AMZI demultiplexer with a size of 500x400μm^2. The passband was relatively flat within 0.7dB across a channel bandwidth of 2.4nm (320GHZ) at a wavelength of 1500nm. The reported crosstalk was only about -15dB but here again we observe the flat-topped box-like wavelength channel shape.

In summary, a number of important filter characteristics have been identified. Firstly, both the FSR and the filter bandwidth parameters are inversely proportional to the path length difference in the interfering optical paths in the filter. Silica is characterized by low waveguide losses but also large bending radii requirements which makes the filters quite large. Consequently, filters with small FSR and very narrow bandwidths are common since it is possible to implement very large path length differences in the interfering optical paths. The SOI platform, due to its high index contrast, provides a means for making these filters much smaller and suitable for dense integration purposes. However, the penalty of making the filter smaller is that the optical path length difference possible in the filters is also reduced due to lack of space. This results in SOI filters with

much wider FSR and bandwidths but much smaller physical size. By using SOI waveguides it is also observed that the reported crosstalk in the filter channels was worse and this was attributed to higher effective index fluctuations in the SOI waveguides. It was also found that AMZI filters have a flatter response in the passband which was seen as being more suitable than a Gaussian-shaped filter spectrum since the in-band wavelength attenuation can be kept relatively constant. With this in mind, one can now consider the characteristics of resonant filters and how they differ from or improve on non-resonant wavelength filters.

4.1.2.2 Resonant optical filters

So what role do resonators played as optical filters and what makes them effective at optical filtering? Integrated resonator topologies used for optical filtering can be categorized into whispering gallery mode resonators also called microdisk resonators [145], photonic crystal slabs [146] and cavities [147], ring resonators [100] and coupled resonator optical waveguides [148].

The filtering effect of ring resonators was proposed as far back as 1969 by Marcatili [149]. By the 1990's silicon based ring resonators had been fabricated with ring radii of 3μm and a wide FSR of 24nm (3THz at 1550nm wavelength) [150]. In 2008 an even smaller SOI ring resonator with 1.5μm radius was demonstrated by Xu et. al. [100] having an FSR of 62.5nm (7.8THz at 1550nm wavelength). These large FSR measurements are due to the small optical path length around the circumference of the ring resonator made possible by the high index contrast of SOI [131]. A significant advantage of the ring resonator topology is that the Quality factor (Q-factor) and hence the bandwidth of the resonator can be controlled by changing the coupling coefficient between the input waveguide and the resonator [151]. High-Q and narrow bandwidth resonators have been demonstrated in silicon [152] With such a wide FSR in these small rings, does it mean there is significant spectral room to fit as many narrow wavelength channels as one would like by controlling the Q-factor? Chu et. al. [153] showed that in practice the channel spacing is limited by the difference in cavity lengths between individual resonator filters that can be achieved. This is because each resonator filter should be resonant at a different wavelength to the other channels. Chu et.

al. [153] utilized 8 ring resonators of different radii and were able to obtain about a 5.7nm channel spacing for a 50nm increment in the ring radius. The bandwidth of each resonator was approximately 1nm and the FSR was approximately 20nm. The benefit of such a wide channel spacing between the narrow bandwidth filter channels was that the reported crosstalk was less than -30dB. Fabrication errors have been identified as a significant problem in controlling the resonance wavelength of ring resonators particularly in filters where the wavelength channels may be closely spaced. Consequently techniques such as thermal tuning [101] have been exploited to better control the resonance of a ring.

Microdisk resonators which are sometimes referred to as whispering gallery mode resonators have also been used as optical filters and closely resemble the ring resonator. Microdisk resonator filters have been demonstrated in SOI [103, 154] and even with radii as small as 1.5μm [145]. However, the major drawback of microdisk resonators as illustrated in [103, 154] is that the resonator supports higher order lateral modes. They indicate that although the coupling efficiency is highest for the fundamental mode, resonant coupling of higher order modes can still occur albeit with lower efficiency. Consequently, the spectrum of a microdisk resonator has several resonance peaks which could possibly interfere with other channels. Another important issue Soltani et al. [154] highlights, which is attributed to traveling wave resonators such as microdisks, is the phenomenon of resonance mode splitting which results from coupling between clockwise (CW) and counter-clockwise resonant modes. This is caused by surface roughness due to fabrication errors and leads to a double peak observable at the resonant wavelength.

Photonic crystal based structures are the third type of resonator based filters that were identified. The photonic crystal (PhC) structure, first proposed in the seminal paper by Yablonovitch [155], is a dielectric periodic lattice structure that supports a so called photonic bandgap within which optical field propagation is prohibited. By introducing defects, such as a line defect [156], in the lattice structure it was shown that so called defect modes could propagate at wavelengths inside the stopband of the photonic crystal A photonic crystal cavity can be introduced as a point defect. This can be done for example by removing periodic structures [147, 157] or by moving adjacent periodic structures further apart[104,

158]. Another method for creating a photonic crystal cavity resonator is to loop a photonic crystal waveguide to form a ring resonator structure [159, 160]. A significant advantage of photonic crystal cavities is their small size and can be even smaller than the operating wavelength [104]. Manzacca et. al. demonstrated a 3 channel WDM system in 2007 utilizing photonic crystal cavities albeit far away from the telecomm wavelengths at 3.2μm. More recently, with improved fabrication methodologies, optical filtering at telecomm wavelengths (1.55μm) has been demonstrated for example in a 4 channel photonic crystal based WDM system [104].

The Photonic crystal slab has also been shown to be resonant in some specific instances. It has been shown [146] that while a photonic crystal slab does in fact support guided modes that are completely confined within the slab, there also exist guided resonances. Guided resonant modes of a photonic crystal slab differ from normal guided modes by the fact that they can couple to a continuum of radiation modes outside the slab resulting in a leaky guided mode. In fact, it has been shown that an externally incident optical field on the photonic crystal slab structure exhibits interesting resonance lines in the transmission and reflection spectrum [161] which could be useful for filtering purposes. What is interesting about this phenomenon is the resonance behaviour in a photonic crystal slab that is due to coupling from a medium with continuum of radiation modes to the guided mode of the photonic crystal. In fact, this phenomenon is analogous to the proposal of this chapter which states that it is possible for an incident TE beam to be reflected from a thin-ridge waveguide due to the coupling that exists between the continuum of TE slab modes in the slab and the waveguide's TM mode, and that this behaviour would exhibit resonance effects.

A significant factor evident when utilizing the aforementioned individual resonators as add-drop filters is that a single resonator has been shown to have a Lorentzian shaped frequency response [60, 145, 147, 162]. This means that the roll-off factor at resonance is fixed and could be a limiting factor in how close wavelength channels can be positioned due to crosstalk. In addition to this, the decaying frequency response round the resonance wavelength would also mean that the attenuation is not constant within the filter bandwidth.

The concept of utilizing several coupled resonators to improve spectral filtering

properties of the single resonator was proposed by Little et. al. in their ground breaking work published in the mid 1990s [162, 163]. They showed that increasing the number of resonators in a series or parallel coupled resonator topology could flatten the passband attenuation of the filter while significantly enhancing the extinction ratio. A few years later Yariv et. al. proposed the idea of coupling resonators together to form a new type of waveguiding structure called the coupled resonator optical waveguide(CROW) [164]. While designs of CROWs based on photonic crystal cavities have been proposed and theoretically investigated [165–168], these recent publications indicate that this research area is still in its infancy in comparison to ring resonator CROWs. Silicon ring resonator CROWS were first demonstrated around 2006 by various groups [148, 169–171]. Xia et. al. [169] demonstrated how, with 16 coupled resonators, an extinction ratio of >40dB could be practically realized across a bandwidth of 4nm. However, their results also showed that there was a significant presence of ripples in the passband. The peak to peak amplitude of the ripples in the passband decreased as the filter order increased. The drawback was that also the insertion loss of the filter increased with the filter order. To overcome this problem, the same group demonstrated that by tapering the coupling coefficients of the ring resonators, it is possible to significantly reduce the ripple effect observed in CROWs [170]. However, in practice this apodization approach does not seem to completely remove the presence of inband ripples as was shown in the Cooper et. al. paper [172] where they fabricated CROWS of 35 up to 235 ring resonators. In spite of using state of the art fabrication methods, their results showed that increasing the number of resonators in a CROW also increases the in-band ripples. By using filter design techniques derived from microwave filter synthesis methods, it has been shown that it is possible to predictably design a higher order filter with pre-determined spectral characteristics such as a maximally flat (Butterworth) filter response [173].

An identified problem with SOI resonators is the low tolerance to fabrication errors For example it has been shown that a deviation of just 1nm in the waveguide width of a ring resonator can result in a resonance wavelength shift of 1nm which is equal to 125Ghz at a 1550nm wavelength [174]. This would be intolerable for example in Dense-WDM where channel spacing can be between 50GHz to

100GHz. To counter this fabrication intolerance problem of silicon, a common approach has been to fabricate tunable CROWS, where the large thermo-optic coefficient of silicon is exploited to be able to adjust the resonance characteristics of individual resonators [175]. Another severe limiting factor of ring resonators in particular which arises from surface roughness during fabrication is coherent backscattering [176], which is the coupling to the counter-propagating resonant mode. This firstly leads to resonance splitting. Morichetti et. al. [176] also showed that the intensity of backscattered light increases with the filter order and can dramatically alter the spectral response of cascaded ring resonators.

4.1.3 Summary

In summary it can be deduced from the reviewed literature that a significant amount of research has been done particularly on ring resonator filters and that they provide the most compact device topology for integrated optical filtering. Resonators provide flexibility in terms of bandwidth since they can be easily tuned by controlling the coupling strength to the bus waveguide. Particularly in silicon, small resonators can yield very wide free spectral ranges. However, fabrication errors in silicon introduce many challenges. The impact of fabrication errors can be overcome through thermal tuning of the resonance wavelength of the ring. Coherent backscattering is also a problem in resonators that is induced by fabrication errors. An avenue for improving the spectral characteristics of resonators, such as the roll-off steepness, has been to couple several to form coupled resonator optical waveguides (CROWs). CROWs also enable the flattening and broadening of the filter passband. However, the sensitivities to fabrication errors and the environment that plague individual resonators are worsened when coupling several resonators together.

In light of these observations on resonators, one finds that there has been significant advancements made but also there is room for improvement in the design of integrated resonant optical filters. Also, in the review of existing literature, no reports have been found that investigate resonance effects in thin-ridge waveguides in relation to the lateral leakage effect. It is therefore considered that there is great incentive in carrying out this research into the reflection be-

haviour observed in Chapter 3 and it would be the first time this research is being reported.

The investigations presented in this chapter thus tackle a number of questions. Firstly, the investigation begins by asking if a reflection of similar strength would be observed in a single thin-ridge waveguide as was observed in the grating of chapter 3. If so, this would likely indicate a resonance effect. Therefore, does this resonance effect have the typical Lorentzian spectral response with a peak reflection response at the resonance wavelength? If it does, can the Q-factor and therefore the bandwidth of resonance be controlled or adjusted and how could this control be achieved? On this basis, one could then ask whether a higher order filter could be designed by cascading several of these potential resonators together? How exactly would this be achieved and what topology would the filter have? How would the filter response relate to that of an ideal higher order filter? These are the main questions that will be investigated in this chapter? Finally, the findings of these investigations will be summarized at the end of this chapter. New research opportunities will be identified and discussed primarily towards the realization of thin-ridge waveguide devices that can be usefully adopted by the silicon photonics community.

4.2 Resonant behaviour of a single thin-ridge waveguide

In the literature review of Section 4.1 it was found that integrated optical resonators are important and useful particularly for optical filtering and that there are several challenges that face the implementation of resonators and coupled resonator optical waveguides (CROWs) in the silicon platform of today. It would therefore be of significant benefit to explore new types of optical resonators and filters. This justifies the search for new resonance effects that may or may not be occurring in thin-ridge waveguides. In Chapter 3, an observation was made that when a TE beam was incident on a grating structure it appeared to be strongly reflected. This occurred even when the index perturbation caused by the waveguide structure was minimized to remove any significant Fresnel reflection. It was

proposed that this reflection may be due to resonant coupling from the incident TE field to a guided TM mode in the grating, which is then coupled back to a reflected TE field (TE-TM-TE coupling). The grating can be considered as several adjacent thin-ridge waveguides. Assuming that it is resonant coupling then it would be expected that this reflection behaviour would occur not only in a grating structure but also in a single thin-ridge waveguide, at a similar level to that of observed for the grating. This would indicate that the observed reflection is due to a resonance effect and not due to some periodic grating-like phenomenon.

In this section the behaviour of an individual thin-ridge waveguide is investigated when it is illuminated with an infinitely wide TE beam. It is expected that if the infinitely wide TE beam is propagating at a specific angle to be phase matched to the waveguide TM mode, then TE-TM-TE coupling should also occur resulting in strong reflection of the incident TE beam. To investigate if it is Fresnel reflection, the infinitely wide TE beam is launched at an offset angle where it is not phase matched and not expected to couple to the TM waveguide mode. The wavelength dependence of this TE-TM-TE coupling is also investigated and its influence on the coupling interaction.

4.2.1 Infinitely wide TE beam incident on a thin-ridge waveguide

It has been shown that when a TM mode is launched into a thin-ridge waveguide it couples to a TE slab mode propagating at a specific angle [14, 15] Consider the case where this process is reversed and an infinitely wide TE beam is launched towards a thin ridge waveguide, shown in Figure 4.1 (a), at the same angle where it is phase matched to the TM guided mode of the waveguide.

Such a scenario is depicted in Figure 4.1 (b) and (c). It is expected that when the TE slab wave (TE_i) is incident on the waveguide walls, it would be coupled to the guided TM wave provided they are phase matched. This conversion process can occur at the first and second waveguide walls (labelled (w_1) and (w_2) respectively in Figure 4.1 (b) and (c)). Conversely, the TM wave excited in the waveguide should couple back to TE slab waves propagating from both waveguide walls. The TE fields transmitted through the waveguide are labelled as TE_t and

those reflected as TE_r.

Therefore, if a TE slab wave, is incident on a thin-ridge waveguide at an angle where it is phase matched to the guided TM wave, then it is expected that a significant portion of the incident TE slab wave would be reflected as a result of this TE-TM-TE coupling interaction. If the incident TE slab wave is not propagating at a phase-matched angle, then it would be expected that no significant reflected fields would be generated since the TM mode does not build up coherently and thus doesn't couple strongly back into the TE polarization. However, some Fresnel reflection could still occur due to the effective index difference between the slab and core regions of the waveguide.

Since this waveguide is assumed to have no longitudinal variations as depicted in Figure 4.1, it is thus possible to use a TE plane wave excitation which is also longitudinally invariant. This was done using the eigenmode expansion method. A description and justification of using the eigenmode expansion method for modeling TE to TM coupling structures has been covered in Section 2.4.2. Two simulations were performed in this investigation. One simulation for an incident infinitely wide TE beam that is phase matched to the guided TM mode of the waveguide and another when it is not phase matched. The phase matching angle between the incident TE beam and the guided TM mode can be calculated as

$$\theta = \arccos(\frac{N_{TM}}{N_{TE}}) \tag{4.1}$$

where N_{TM} is the the effective index of the guided TM mode and N_{TE} is the effective index of the TE slab mode. For a waveguide with the geometries of width w=420μm, etch depth h=20nm and slab thickness t=200nm, the mode matching technique as discussed in Section 1.1.4 was used to evaluate N_{TM} and N_{TE} as 1.76 and 2.76 respectively. The incident angle θ was hence evaluated as 50.32°. For the control simulation, where the infinitely wide TE beam is not phase matched to the waveguide TM mode, the launch angle for the TE beam was set to 41°.

Figure 4.2 shows a crosssectional representation of the field which is invariant along the length of the waveguide since the waveguide is longitudinally invari-

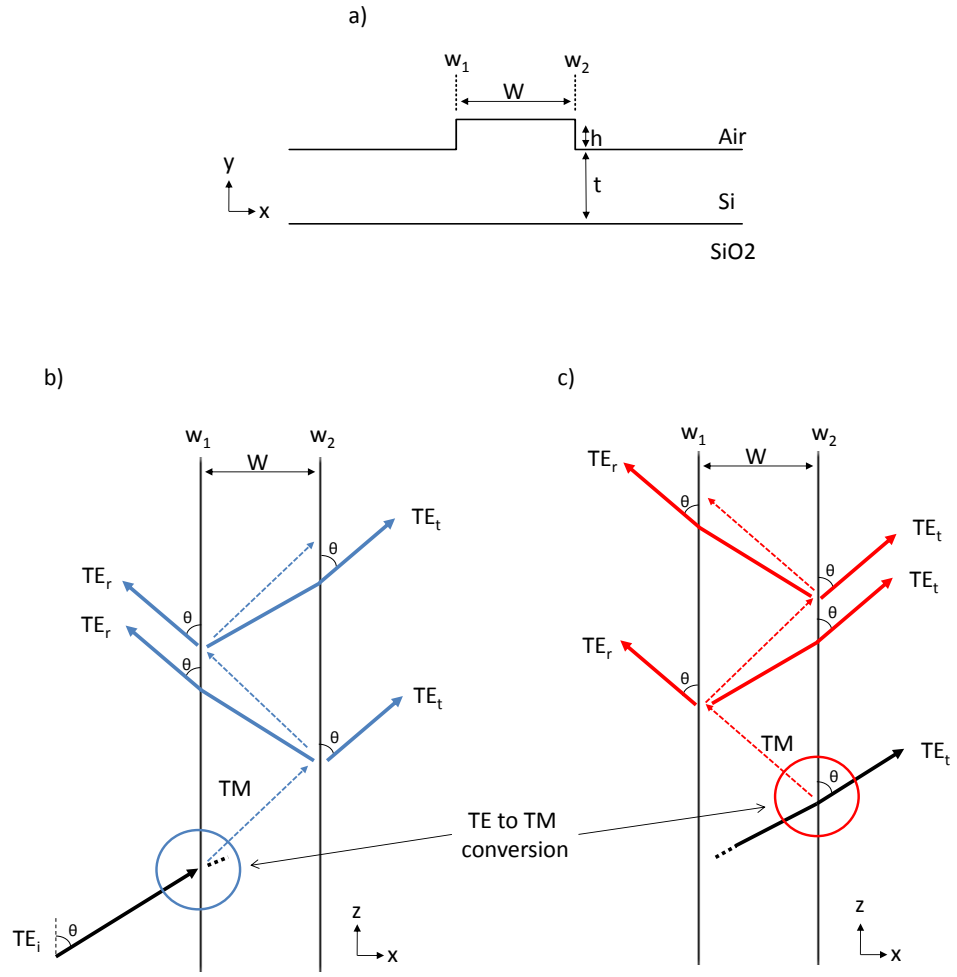

Figure 4.1: (a) Cross sectional profile of a thin-ridge waveguide of width w, etch depth h and slab thickness t. Plan view of the thin-ridge waveguide showing a simple ray-diagram depiction of an infinitely wide TE beam incident on (b) the first and (c) the second waveguide walls, where cascaded TE to TM conversion can occur resulting in reflected TE_r and transmitted TE_t TE fields.

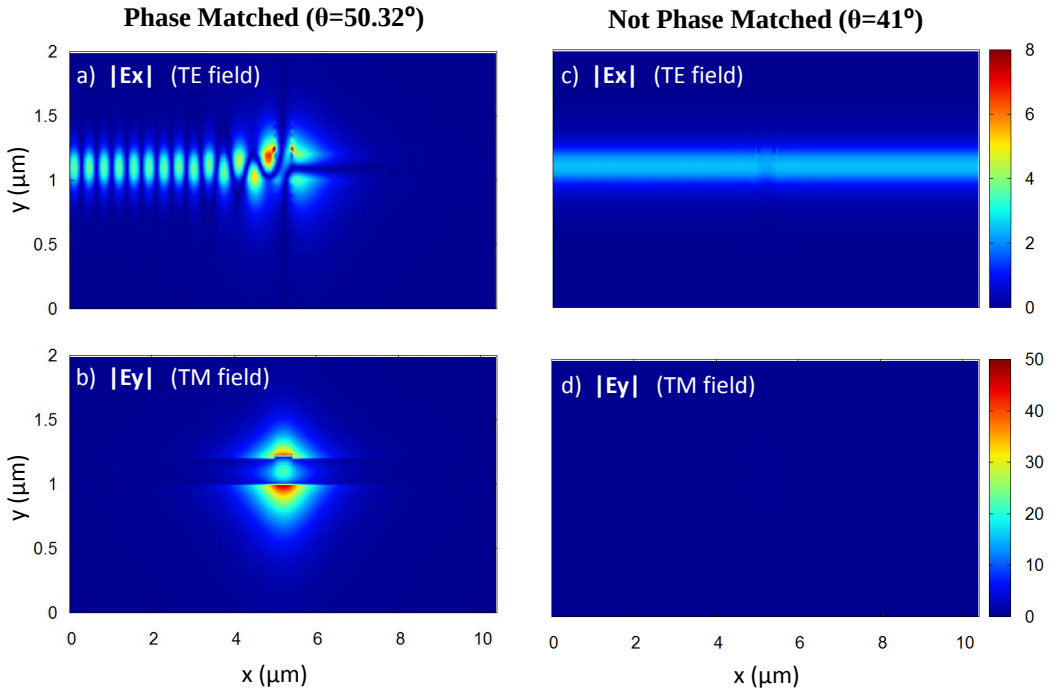

Figure 4.2: Shows the magnitude of the x-component (TE) of the electric field for (a) the phase-matched and (b) not phase-matched cases respectively. Shows the magnitude of the y-component (TM) of the electric field for the (c) phase-matched and (d) not phase-matched cases respectively.

ant and the excitation is a TE plane wave. The infinitely wide TE beam was launched from z=0, at the left-hand side of the simulation window, towards the waveguide. Figure 4.2 (a) shows the x-directed electric field corresponding to the TE polarisation in the case where the infinitely wide TE beam was launched at a phase-matching angle (θ=50.32°). An interference fringe pattern is observed in the slab region on the left of the waveguide which is where the incident TE beam was launched from. On the right hand side of the waveguide it is observed that no TE fields are transmitted beyond the waveguide. For the non-phase-matched waveguide scenario (θ=41°), the x-directed (TE) electric field is shown in Figure 4.2 (c). It is observed that the launched TE field is slightly perturbed at the waveguide in the center of the simulation window but is mostly transmitted through the waveguide.

Figure 4.2 (b) shows the y-component of the electric field corresponding to the TM polarisation when the incident TE beam is phase-matched (θ=50.32°). It can be seen that a TM field is excited in the waveguide by the incident TE beam which resembles the fundamental TM mode of the waveguide. Figure 4.2 (d) shows the y-component of the electric field corresponding to the TM polarisation when the incident TE beam is not phase-matched (θ=41°). No TM fields are seen to be excited in Figure 4.2 (d) for the non-phase-matched waveguide scenario.

From these results it is evident that at the wavelength of 1.55μm there is a very strong reflection of the incident TE field when it is launched at a phase matching angle to the waveguide TM mode. This is evidenced by the interference fringe pattern observed in Figure 4.2 (a) which is caused by the superposition of the launched infinitely wide TE beam and a reflected TE beam. The dark null fringes of the interference pattern also indicate that the forward and backward propagating fields are of relatively equal amplitude meaning that the reflection observed was strong. This is similar to what was observed in the TE field reflection from the grating in Section 3.6

In the example where the infinitely wide TE beam is not phase matched to the waveguide TM mode, as shown in Figure 4.2 (c) and (d), no interference fringes were observed and thus it can be concluded that no significant reflected fields were generated. This means that any Fresnel reflected fields generated due to the TE beam traversing the waveguide refractive index perturbation were negligible. It is believed that this reflectivity, when the TE and TM modes are phase-matched, must therefore be due to the coupling between the infinitely wide TE beam and TM guided mode. Given that the coupling process is bi-directional, the TM guided mode would then couple all of its energy back into the TE beam.

Nevertheless, it was predicted that the TM guided mode in the waveguide would couple to TE radiation on both sides of the waveguide as observed in other investigations on lateral leakage [15]. However, Figure 4.2 (a) shows that the TE field only exists on one side of the waveguide which raises the question of why we do not see TE radiation on both sides of the waveguide. This appears similar to a ring resonator waveguide when coupled to two bus waveguides [151] in an add-drop waveguide topology. At resonance, the field coupled to the ring resonator from the input bus waveguide is observed to exit at the drop port of

the other bus waveguide. This is due to destructive field interference occurring at the through port of the input waveguide at resonance, whereas at all other wavelengths the field exits from the through port [151]. Therefore, one possible interpretation is that when the infinitely wide TE beam is coupled to the waveguide TM mode, there is destructive interference occurring on the transmission side of the waveguide.

These results clearly show that a TE slab beam undergoes strong reflection when incident on a thin-ridge waveguide at an angle where it is phase matched and can therefore couple to the resonant or trapped TM mode of the waveguide. The strength of this reflection is similar to that observed in Chapter 3 when a TE beam was incident on a grating structure in Section 3.6. This supports the hypothesis that this strong reflection is due to resonant coupling from the incident TE beam, to the guided TM mode and back.

4.2.2 Wavelength response of a TE beam reflection from a thin-ridge waveguide

It was shown in Section 4.2.1 that an infinitely wide TE beam can be completely reflected when incident on a thin-ridge waveguide if it is phase-matched to the TM mode of the waveguide. This behaviour seems typical of a conventional resonator if the infinitely wide TE beam is considered as the input field and the waveguide TM mode is the resonant mode which it can couple to. As discussed in Section 4.1.2, resonators are particularly useful because of their wavelength selectivity for applications such as filtering. It would therefore be interesting to explore the wavelength dependence of this resonance-like behaviour observed in thin-ridge waveguides.

As discussed in Section 4.2.1, for there to be resonant coupling between the incident TE beam and the waveguide TM mode, the incident angle needs to be such that phase matching is achieved. In Section 2.4.5, the wavelength dependence of this phase matching angle was explored and it was found that while there is indeed a wavelength dependence, it is not very strong, having a 3dB bandwidth of as much as 12nm. Therefore, if we launch an incident infinitely wide TE beam toward a thin-ridge waveguide, at an angle that gives resonant

interaction, as seen in Figure 4.2 (a) and (b), one might then expect the coupling strength to change with wavelength. However, would this wavelength dependent reflection be similar or different to that observed in Section 2.4.5?

The same 2D eigenmode expansion technique that was used in Section 4.2.1 was utilised to evaluate the reflection and transmission coefficients when an infinitely wide TE beam is incident on a thin-ridge waveguide. The reflection and transmission coefficients were evaluated as a function of wavelength. The same waveguide was used as in Section 4.2.1 and the infinitely wide TE beam was launched at the same angle of 50.32°. As illustrated in Figure 4.3 (a), the reflection and transmission coefficients were evaluated as

$$Reflection : \Gamma = \frac{TE_r}{TE_i} \tag{4.2}$$

$$Transmission : T = \frac{TE_t}{TE_i} \tag{4.3}$$

where Γ is the reflection coefficient and T is the transmission coefficient. TE_i is the incident TE beam amplitude, TE_r is the reflected TE beam amplitude and TE_t is the transmitted TE beam amplitude.

Figure 4.3 (b) shows the amplitude of the reflection and transmission coefficients as a function of wavelength from 1.48μm to 1.62μm. The reflection coefficient response shows that at the central wavelength of 1.55μm there is 100% reflection of the TE beam. As the wavelength increases or decreases away from this central wavelength the reflection coefficient decays exponentially. The transmission coefficient curve shows the opposite trend. At the central wavelength of 1.55μm there is almost zero transmission of the TE field. Away from the central wavelength the transmission coefficient asymptotes to unity, meaning 100% transmission.

Similar to the wavelength response in Section 2.4.5, the decay in this reflection coefficient occurs because the further away one shifts from the center wavelength, the phase-matching between the incident TE beam and the TM mode of the waveguide also changes. The reflection and transmission of the thin-ridge waveguide illuminated by an infinitely wide TE beam indeed appears to have a

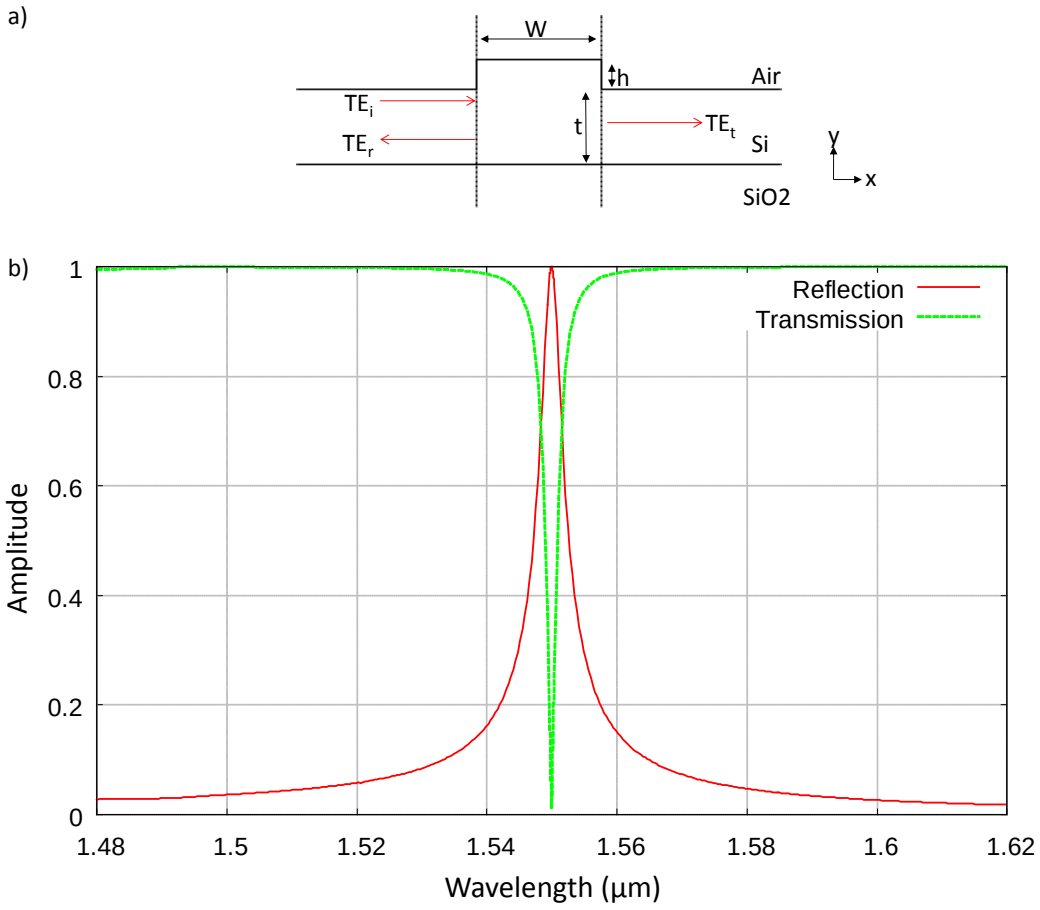

Figure 4.3: (a) 2D thin-ridge waveguide schematic illustrating the TE incident (TE_i), reflected (TE_r) and transmitted (TE_t) beams. (b) Amplitude of the reflection and transmission coefficients as a function of wavelength

wavelength dependent response. This response is far sharper, with a bandwidth of 3nm, than the broad wavelength response observed in Section 2.4.5 which had a bandwidth of about 12nm. This response instead looks rather like the sharp wavelength response of the ring resonators [152] discussed in Section 4.1.2.2.

This result has therefore shown that a thin-ridge waveguide, when illuminated by an infinitely wide TE beam, has a wavelength dependent reflectivity. At the resonant wavelength, strong coupling between the incident TE field and the resonant TM waveguide mode results in complete reflection. A shift in wavelength away from resonance results in a decay of the observed reflectivity resulting in a sharp resonance peak in the reflection spectrum similar to that of a ring resonator.

4.2.2.1 Lorentzian wavelength response of the thin-ridge waveguide resonator

As reviewed in Section 4.1.2.2, resonators such as optical microring resonators are know to have a canonical Lorentzian frequency response when observed for example from the drop port [60]. If a thin ridge waveguide, which has been shown to have a wavelength dependent reflectivity, has a typical resonance response, then it should be Lorentzian.

Near resonance, a Lorentzian function can be approximated as [41]

$$L(f) \approx \frac{(\Delta f/2)^2}{(f_0 - f)^2 + (\Delta f/2)^2} \tag{4.4}$$

where the function has been normalized to have a maximum value of one when $f = f_0$. Δf is the full width at half maximum (FWHM) bandwidth and f_0 is the center frequency. The reflected amplitude of Figure 4.3 was squared to obtain the reflected intensity. This reflected intensity is presented in Figure 4.4. Equation (4.4) was then plotted as a function of wavelength instead of frequency over this simulated reflected intensity. The parameters of bandwidth and center wavelength were then adjusted to provide the best fit.

It is evident that the intensity of the reflection coefficient of the thin-ridge waveguide has a similar form to a Lorentzian function. This result therefore affirms that a thin-ridge waveguide behaves as a typical resonator when illuminated

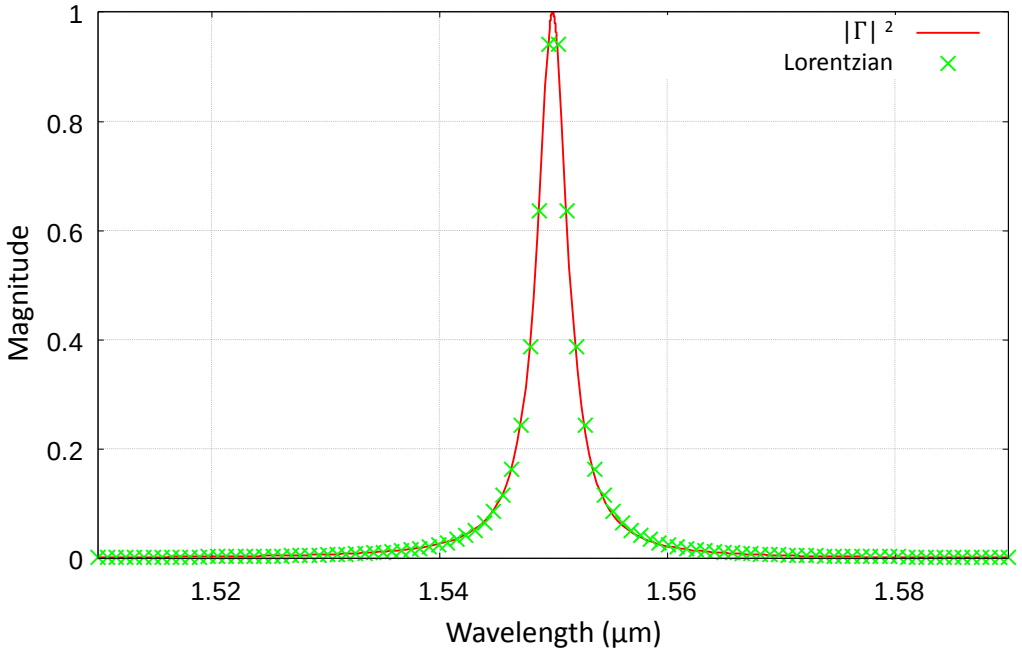

Figure 4.4: Thin-ridge waveguide reflection coefficient squared ($|\Gamma|^2$) as a function of wavelength compared to a Lorentzian function of equal bandwidth.

by a TE slab beam. It is thus possible to conclude that the thin-ridge behaves as a resonator of some sort. However it is still perhaps surprising that the line-width of the resonator is so much narrower than the frequency response observed for the lateral leakage analysed in Section 4.2.1.

4.2.3 Comparison of a thin-ridge waveguide resonator to a conventional lumped element resonator

In Section 4.2.2 it was shown that a thin-ridge waveguide resonator has a wavelength dependent reflectivity and that that this response is Lorentzian in shape. Only the amplitude response of the reflectivity was considered. However, is the spectral response of a thin-ridge waveguide identical to that of conventional resonators? A lumped element (LC) resonator is an ideal canonical resonator composed of ideal loss-less capacitors and inductors whose spectral response can be mathematically evaluated [177]. In fact, the lumped element resonator represents

the basic resonator prototype used in the synthesis of higher order filters in microwave [177] and optical frequencies [173]. Therefore, is the resonance response of a thin-ridge waveguide similar to a canonical LC resonator in both amplitude and phase?

The spectral response of a thin-ridge waveguide resonator observed in Section 4.2 indicates that it behaves as a bandstop filter since at resonance, the incoming field is completely reflected and thus no power is transmitted past the waveguide. If the thin-ridge waveguide indeed behaves as a canonical resonator and has a Lorentzian bandstop filter response, then it should be possible to find prototype parameters for a lumped element filter that will provide exactly the same response.

To show this, the reflection (Γ) and transmission (T) response of the 550nm thin-ridge waveguide resonator was considered. A waveguide of 550nm width was chosen for this investigation but any waveguide dimension would be suitable for this analysis. As in Section 4.2.2, the TM mode and TE slab mode effective index of the 550nm wide waveguide was first evaluated. This was then used to evaluate the TE phase-matching angle from Equation (4.1). An infinitely wide TE beam was launched at this angle towards the waveguide and the reflectivity evaluated over a range of wavelengths. From this spectral response, the FWHM could be evaluated.

For the lumped element resonator, there are two ways to achieve a bandstop filter response using LC components. There is the series inductor and capacitor which is placed in parallel with the load as shown in Figure 4.5 (b). Another topology is an inductor and capacitor in parallel which is placed in series with the load as shown in Figure 4.5 (c). Both these circuits are derived from the first steps of filter synthesis as shown in [177]. For the series LC resonator placed in parallel with the load, the element values were calculated from [177] as

$$L = \frac{R_L}{2\pi f_0 g(B/f_0)} \tag{4.5}$$

$$C = \frac{g(B/f_0)}{2\pi f_0 R_L} \tag{4.6}$$

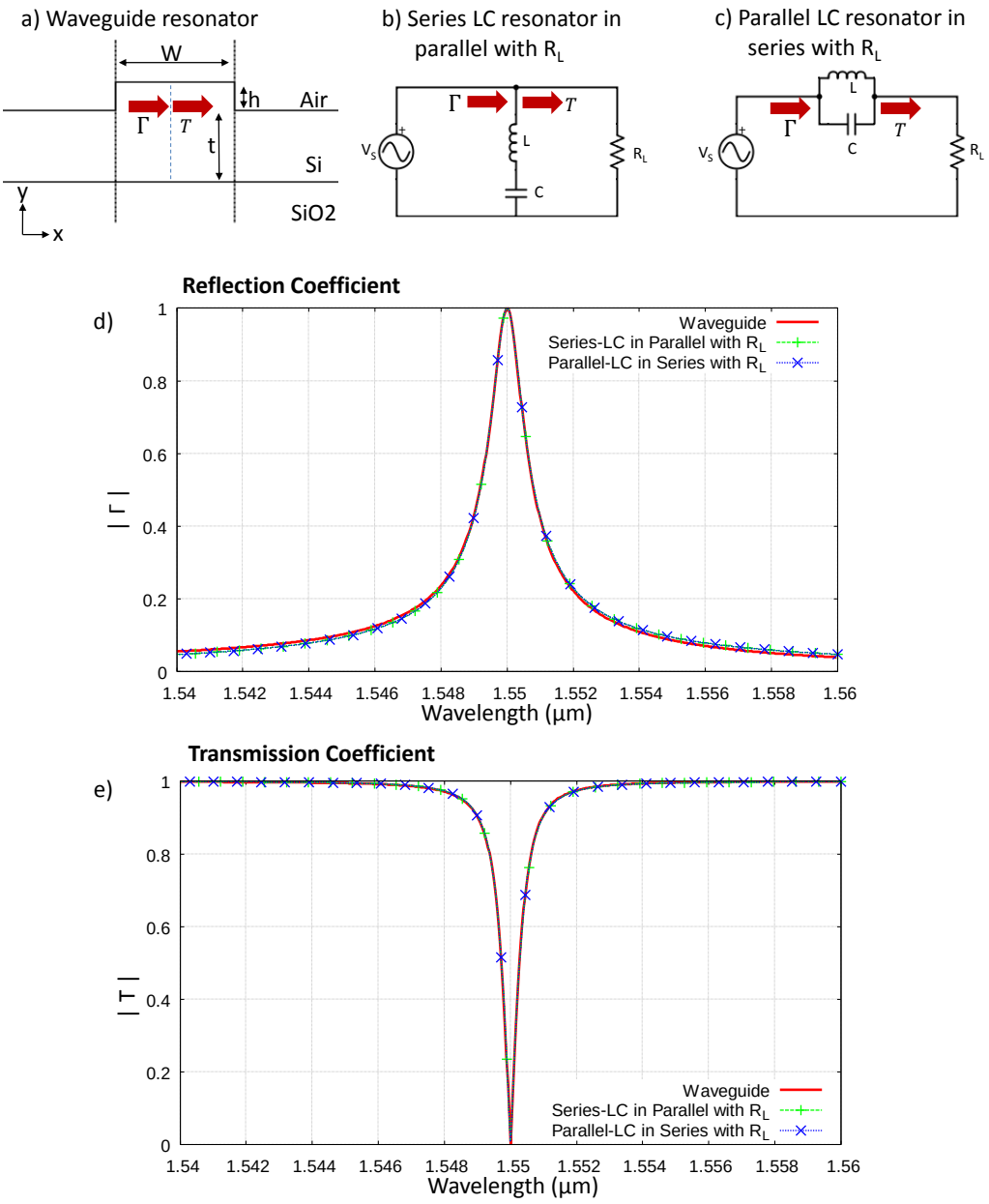

Figure 4.5: (a)Thin ridge waveguide resonator with W=550nm, h=20nm and t=200nm. (b) The and series LC resonator circuit in parallel with the load. (c) The parallel LC resonator circuit in series with the load. (d) The evaluated magnitude of the reflection coefficient and (e) the evaluated magnitude of the transmission coefficients for the three resonators shown in a,b and c.

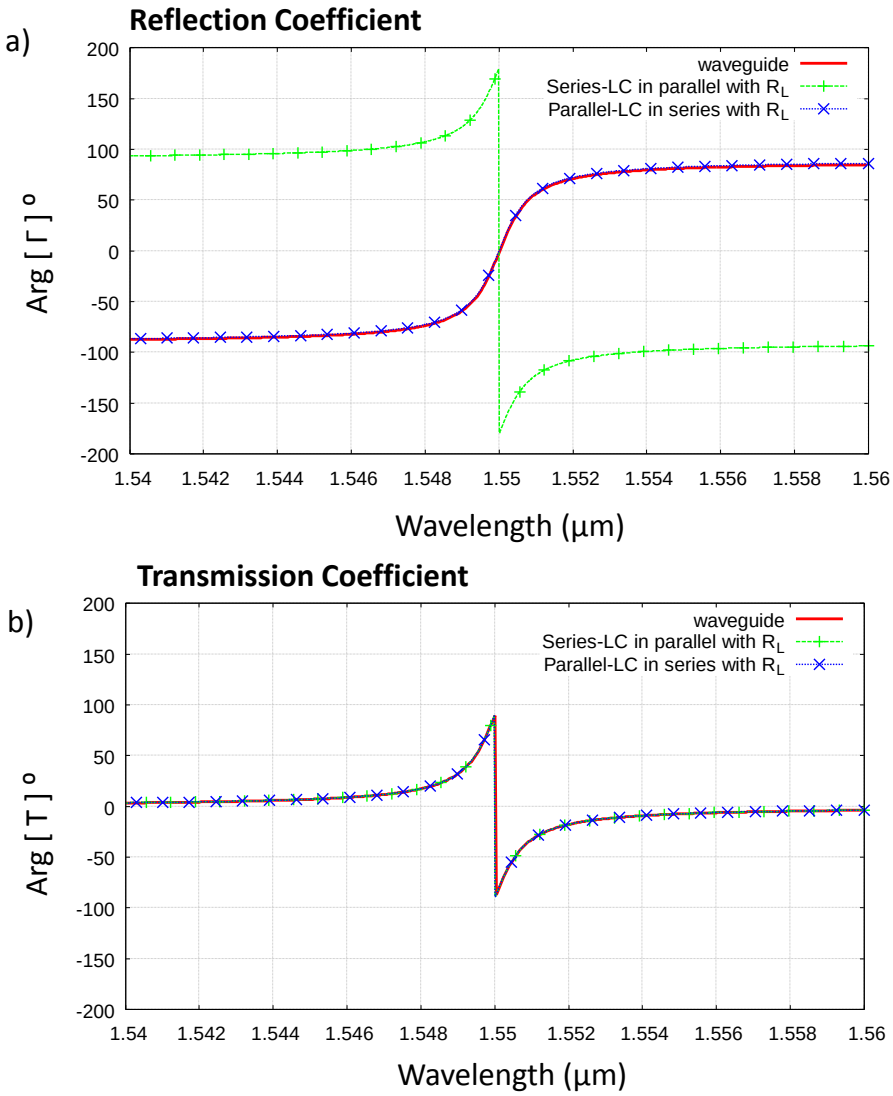

Figure 4.6: Shows the phase response of (a) the reflection and (b) the transmission coefficients respectively for the three resonators shown in Figure 4.5 (a), (b) and (c).

where the load resistor is R_L, f_0 represents the center frequency, B is the frequency bandwidth and g is the single element low pass prototype filter value. For a single resonator, the filter prototype parameter value from [177] is g=2. One can assume that the load impedance is normalised so R_L=1. From Figure 4.5, it is seen that the centre wavelength is $\lambda_0 = 1.55\mu$m, and this corresponds to a frequency of f_0=193.55THz. The line width of the resonant response of Figure 4.5 is approximately 0.94nm and this corresponds to a frequency of 0.117THz.

For the series LC resonator placed in parallel with the load shown in Figure 4.5 (b), the evaluated inductor value was therefore 6.75×10^{-13}H and the capacitor value was 1×10^{-18}F. For the parallel LC resonator in series with the load, shown in Figure 4.5 (c), the Equations (4.5) and (4.6) simply change over to now represent the capacitor and inductor respectively. Therefore, for the parallel LC resonator in series with the load, the inductor value was evaluated from Equation (4.6) as 1×10^{-18}H while the capacitor value was evaluated from Equation (4.5) as 6.75×10^{-13}F.

On the basis that the source impedance also has a normalized value of 1 as did the load impedance R_L, the reflection response of the LC resonator circuit was evaluated by first calculating the circuit's input impedance Z_{in}, which is evaluated from the R_L, L and C values [177]. From the circuit's input impedance, the reflection and transmission coefficient response could then be calculated as

$$\Gamma = \frac{Z_{in} - 1}{Z_{in} + 1} \quad and \quad T = 1 + \Gamma \tag{4.7}$$

Figure 4.5 (d) shows the magnitude of the reflection coefficient as a function of wavelength for the waveguide resonator and the LC resonators. The waveguide resonator and the two LC resonators are observed to have nearly identical reflection amplitude responses. Figure 4.5 (e) shows the transmission coefficient magnitude as a function of wavelength. Similar to the reflection coefficient, it is observed that the transmission response of the waveguide is nearly identical to that of the two LC bandstop resonators.

Figure 4.6 (a) shows the reflection coefficient phase response of the waveguide and the two LC resonator circuits. From this figure it is evident that the reflection phase response of the thin-ridge waveguide is only similar to that of the parallel-

LC resonator but not the series-LC resonator. Shown in Figure 4.6 (b) is the phase of the transmission coefficient for the waveguide resonator and the LC resonator circuits. It is seen here that the transmission phase response of these three resonators are nearly identical. From these results it is evident that only the parallel-LC resonator illustrated in Figure 4.5 (c) is similar in amplitude and phase, for both the reflection and transmission response, to the waveguide resonator.

Consequently, one can conclude that the reflection and transmission response of the thin-ridge waveguide resonator, both in terms of amplitude and phase, can be modeled using a lumped element filter prototype formed as parallel LC circuit that is in series with the load as illustrated in Figure 4.5 (c). Therefore, it may be possible to consider the fact that if higher order filter responses can be synthesized from the canonical LC resonators, then given the equivalency shown above, it may be possible to also synthesize higher order filter responses using thin-ridge waveguide resonators. However, it would be valuable to first analyse the factors that impact the Q-factor of the observed thin-ridge waveguide resonance.

4.2.4 Factors determining the Q-factor of the thin-ridge resonator

It was observed in Section 4.2.3 that a thin-ridge waveguide behaves just like a canonical Lorentzian resonator. At the resonant wavelength, an incident TE beam is completely reflected due to resonant coupling to the TM mode of the waveguide. Away from resonance, the magnitude of this reflection was shown to decay following the Lorentzian function of Equation (4.4). This rate of decay represents the resonators bandwidth or quality factor (Q-factor). The Q-factor can be defined as a ratio between the frequency at which the resonance occurs divided by the 3dB width (FWHM) of the resonance [151]. This is a measure of how much energy is stored within the resonator. In order to achieve a high Q-factor, it is necessary to minimize cavity losses, including the loss associated with coupling into and out of the resonant cavity, and also maximise the length of the cavity [151]. For a thin-ridge waveguide, it has been shown that the waveguide lateral leakage loss is dependent on the waveguide dimensions, particularly the

width [15]. The waveguide height can also be changed to increase or decrease the lateral leakage rate [14]. It was also shown in Section 4.2.1 that through the lateral leakage effect resonant coupling can occur between an incident TE beam and the resonant TM mode. The lateral leakage loss could therefore be interpreted to be the loss associated with coupling in and out of the resonant TM mode. It is expected that if the waveguide dimensions influence the degree of lateral leakage and that this in turn determines the cavity losses of the resonant TM mode in the waveguide, then the waveguide dimensions should also influence the thin-ridge waveguides Q-factor. This section, looks at whether the waveguide dimensions, both width and height, do influence the thin-ridge waveguides Q-factor.

4.2.4.1 Dependence of Q-factor on waveguide width

If the Q-factor of the thin-ridge waveguide resonator is determined by the degree of lateral leakage, then adjusting the width of the waveguide should significantly alter this lateral leakage and hence should have a significant impact on the Q-factor of the thin-ridge waveguide resonator.

To test this hypothesis, two simulations were done. Firstly, the reflection coefficient response of three thin-ridge waveguides with different widths was simulated when an infinitely wide TE beam was incident on the waveguides as shown in Figure 4.7 (a). The second part was to vary the waveguide width over a wide range of values and to plot the Q-factor as well as the waveguide lateral leakage loss as a function of the waveguide width. The same eigen mode expansion simulation technique was used as was described in Section 4.2.1. For the first simulation the three waveguides have identical core thickness of 200nm and etch depth of 20nm. The waveguide width w was chosen for the three waveguides to be 400nm, 550nm and 720nm. These were selected from [15] such that the 400nm waveguide had the strongest coupling between the infinitely wide TE beam and TM guided mode; the 720nm waveguide had the weakest TE-TM coupling; and the 550nm waveguide was selected to be around the middle point of these two extremes.

It should be noted that as the waveguide width increases from 400nm to 720nm, the effective index of the TM mode also increases as the waveguide size

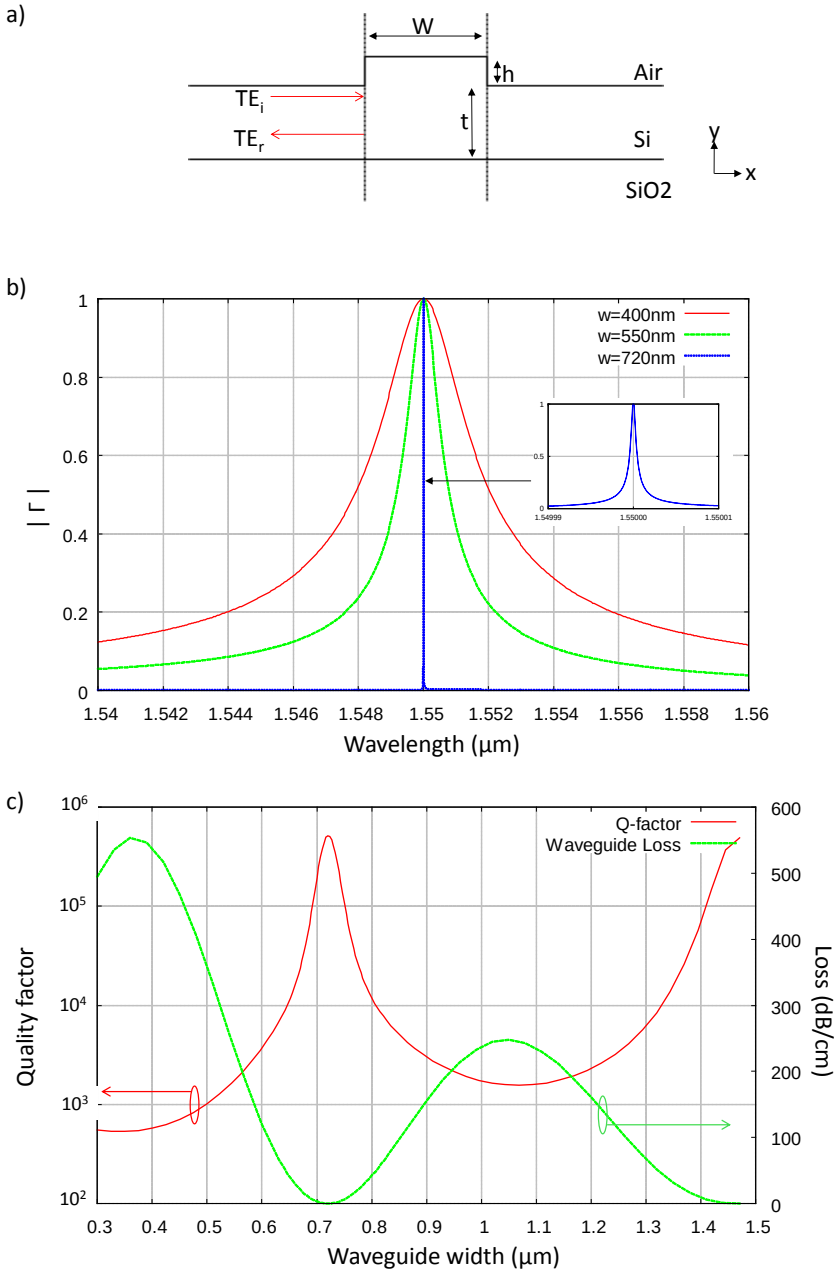

Figure 4.7: (a) 2D Simulation window of the SOI thin-ridge waveguide with a slab thickness t=200nm and etch depth h=20nm. (b) The amplitude of the reflection coefficient as a function of wavelength for three values of the waveguide width w = 400nm, 550nm and 720nm. (c) Waveguide resonator Q-factor and loss as a function of waveguide width.

increases [10]. Therefore, the angle of the infinitely wide TE beam required to phase-match to the TM mode at a wavelength of 1550nm would be different for each width. It therefore became necessary to re-evaluate the phase-matching angle of the infinitely wide TE beam for each of the three waveguides when centered at 1550nm. Based on the aforementioned waveguide dimensions the effective index of the guided TM mode and the infinitely wide TE beam was evaluated using the mode matching technique discussed in Section 1.1.4. From the mode effective indices, the phase-matching angle could be evaluated from Equation (4.1) for each waveguide. The infinitely wide TE beam phase-matching angle was found to be 50.42°, 49.82° and 49.2° for the 400nm, 550nm and 720nm waveguides respectively. These were the angles at which the TE beam was launched for each of the three waveguide simulations to evaluate the reflection wavelength response.

The 3dB bandwidth of the resonator can be evaluated from the reflection coefficient response and the Q-factor could then be calculated from the bandwidth [151] as

$$Q = \frac{\lambda_0}{B} \tag{4.8}$$

where Q is the Q-factor of the resonator, λ_0 is the resonance wavelength and B is the full width half maximum bandwidth. For a wide range of waveguide widths, the Q-factor of each resonator was evaluated and plotted as a continuous function of the waveguide width together with the waveguide lateral leakage loss. The lateral leakage loss was evaluated from the imaginary part of the TM mode effective index obtained from the mode matching technique described in Section 1.1.4.

Figure 4.7 (b) shows the amplitude of the reflection coefficient for the three waveguides with widths 400nm, 550nm and 720nm. By design, the resonance of the three waveguides are centered at 1.55μm. It is observed that the wavelength response of the 400nm waveguide has the widest bandwidth and consequently the lowest Q-factor. The 720nm waveguide has the narrowest bandwidth and hence the highest Q-factor while the bandwidth and Q-factor of the 550nm waveguide resides in the middle.

Figure 4.7 (c) shows the Q-factor and the lateral leakage loss as a function

of the waveguide width. It is observed that the highest Q-factor corresponds to the lowest lateral leakage loss and the lowest Q-factor corresponds to the highest lateral leakage loss.

It is therefore clear from Figure 4.7 (b) that by changing the waveguide width it is possible to change the resonance bandwidth which is related to the Q-factor. However, a consequence of changing the waveguide width is that the TM mode effective index also changes, which means the coupling angle needs to be re-evaluated if the resonance wavelength is to stay the same. Figure 4.7 (c) highlights the relationship between the Q-factor and the waveguide width showing that it can change over a wide range from less than 1000 to over 100,000 theoretically. Figure 4.7 (c) also highlights that the waveguide lateral leakage loss has an inverse relationship to the Q-factor. A high lateral leakage loss indicates a low-Q and low lateral leakage loss indicates a high-Q. This supports the proposal that the lateral leakage loss could be considered to be the loss associated with coupling in and out of the resonant TM mode.

In summary, these results support the hypothesis that the Q-factor observed in the reflection response of the thin-ridge waveguide can be significantly altered by adjusting the waveguide width.

4.2.4.2 Dependence of Q-factor on waveguide height

The second waveguide dimension that has an effect on the lateral leakage rate or loss is the waveguide height [14]. If the ridge height can alter the lateral leakage rate then it should also alter the resonator Q-factor based on the relationship observed between loss and Q-factor in Section 4.2.4.1

To test this, the waveguide Q-factor and lateral leakage loss was investigated as a function of the waveguide's ridge height. Using the same simulation method as highlighted in Section 4.2.4.1, both the Q-factor and the waveguide loss were evaluated for waveguides of varying ridge-height. A fixed waveguide width of 550nm was chosen and the ridge height was varied from 5nm to 105nm. The maximum value was set to 105nm which is about half the waveguide core thickness. This maximum height was chosen to minimise Fresnel reflections. It is not unreasonable to assume that in silicon, an incident TE field on an abrupt transi-

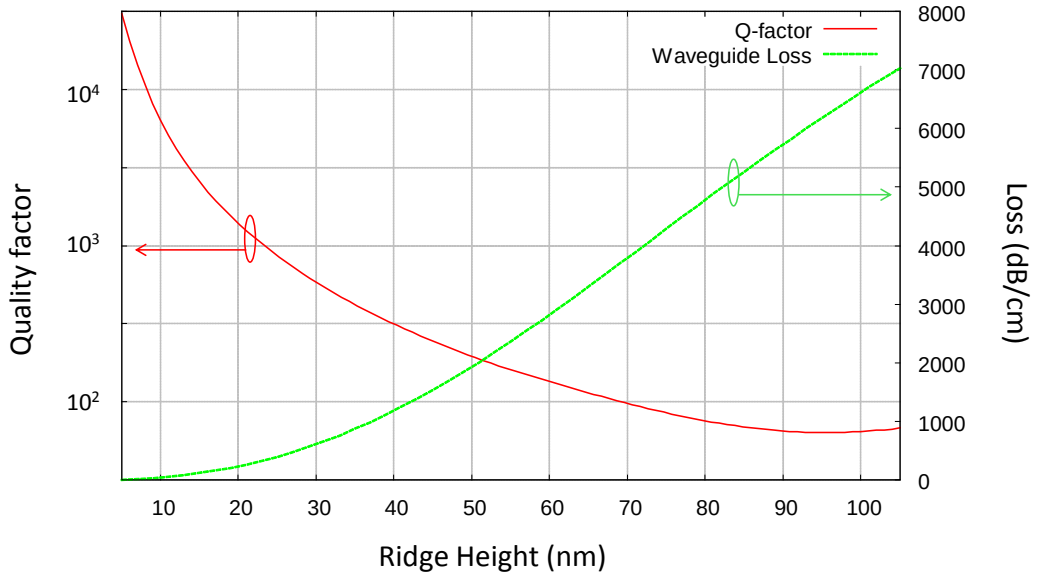

Figure 4.8: Waveguide resonator Q-factor and loss as a function of the waveguide's ridge height.

tion of half the waveguide thickness may cause significant Fresnel reflections. In fact, strong reflective mirrors for Echelle gratings [141] are fabricated in silicon by simply etching through the silicon layer. It is desirable that Fresnel reflections are minimized when studying the resonance effects in thin-ridge waveguides since they both cause reflection of an incident field. A 15nm etch depth on a silicon waveguide would exhibit a fresnel reflection coefficient of less than 1% which is negligible

Figure 4.8 shows the Q-factor and waveguide loss as a function of the ridge height. What is notable is that the gradient of the Q-factor curve is decreasing with increase in ridge height. The highest rate of change of the Q-factor is observed at the smaller ridge heights. There is also a significant change in the lateral leakage loss as the waveguide height increases.

One can observe the same trend in these results which indicated that the Q-factor is inversely related to the lateral leakage loss similar to what was observed in Section 4.2.4.1. The conclusion is that the ridge height also has a significant effect on the thin-ridge waveguide's Q-factor.

4.2.5 Resonators of varying Q-factor but resonant at the same wavelength and angle of incidence

In Section 4.2.1 it was shown that the infinitely wide TE beam must propagate at a specific angle that allows it to couple to the TM guided mode of the thin-ridge waveguide as was expressed in Equation (4.1). However, in Section 4.2.4 it was discovered that the Q-factor of the resonator is related to the waveguide loss which is dependent on the geometry of the waveguide. If the width is varied in order to adjust the Q-factor of a waveguide resonator, then it was seen in Section 4.2.4 that the TM mode effective index would also change. Consequently, for the resonance wavelength to remain the same, it was found that the infinitely wide TE beam angle of excitation had to be changed as well.

If one were to try to use the thin ridge structure as a resonator with a particular TE beam, then it would be advantageous to be able to adjust the resonator Q-factor without changing the resonant frequency or angle of incidence. This leads to the question: is it possible to change a thin-ridge waveguide's Q-factor by altering the waveguide dimensions while the resonance wavelength remains fixed and the angle of excitation also remains fixed? Such flexibility would enable even more control of a thin-ridge waveguide's resonance characteristics. Given the very different forms of the relationship between resonator Q and the waveguide width and height found in Section 4.2.4, it is proposed that this could be possible on the basis that not only the waveguide width changes but also the waveguide height. It is believed that if both of these dimensions of freedom are used, width and height, it could be possible to maintain the same TM mode effective index, which determines the TE phase-matching angle, while the Q-factor is altered.

To test this hypothesis, waveguides of varying Q-factor but a constant TM mode effective index needed to be found and their wavelength response simulated. The same simulation method described in Section 4.2.4.1 was used to evaluate the waveguide Q-factor as a function of the waveguide dimensions. The waveguide width was varied from 0.3μm to 1.5μm while the ridge height was varied over a small range of 5nm to 30nm. The maximum ridge height value was decreased from 105nm to 30nm since the maximum rate of change in Q-factor occurred at the lower ridge heights as seen in Figure 4.8. Fresnel reflections would also be

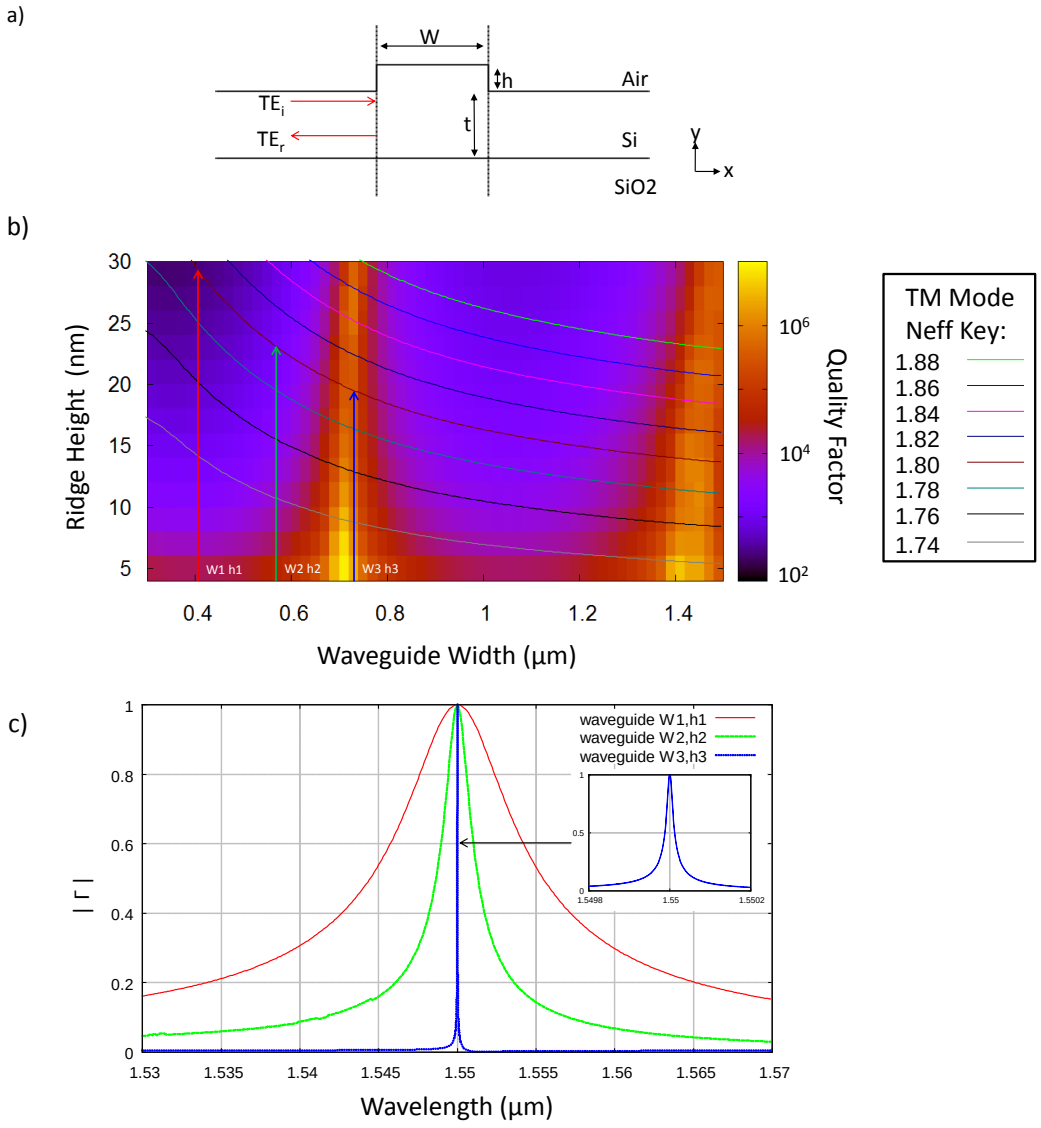

Figure 4.9: (a)Thin ridge waveguide resonator with dimensions t=200nm, width w and height h. (b) 2D plot of the waveguide Q-factor as a function of the waveguide dimensions of width and height. The contour lines show points of constant guided TM effective index. (c) shows the amplitude of the reflection coefficient as a function of wavelength for three waveguides with different Q-factor but equal TM effective index (1.8).

minimal at smaller ridge heights. The slab waveguide thickness remained fixed at 200nm.

In the simulation of Section 4.2.4.1, the imaginary part of the TM mode effective index was used to find the lateral leakage loss. Therefore, the data of the real part of the TM mode effective index was at hand. The TM mode effective index data was therefore plotted as contour lines ontop of the 2D waveguide Q-factor plot to highlight waveguide dimensions having a constant TM mode effective index. The result of this process is shown in Figure 4.9 (b). It shows that the contour lines of constant TM effective index traverse regions of varying Q-factor.

For the second step three waveguides were selected from Figure 4.9 (b) having the same TM effective index (N_{TM}=1.8) but different Q-factors. The first waveguide, selected from the lowest Q-factor region, had a width w1=400nm and height h1 = 29.6nm. The second waveguide, selected from the median Q-factor region had dimensions w2=550nm and h2=23.5nm. The third waveguide,selected from the high Q-factor region, had dimensions w3=700nm and h3= 19.9nm. To simulate the wavelength response of these waveguides, the same eigen mode expansion method was used as done before in Section 4.2.2. The phase-matching angle was evaluated from Equation (4.1) since the TM mode and TE beam effective indices had been obtained from the mode matching simulations. An infinitely wide TE beam was therefore launched towards the three waveguides at the same angle of 49.29°.

Figure 4.9 (c) shows the reflection coefficient amplitude as a function of wavelength for the waveguides selected from Figure 4.9 (b). It shows that the three waveguides are resonant at the same wavelength of 1.55μm when excited by the infinitely wide TE beam propagating at 49.29°. However, the three waveguide resonators have different Q-factors. The waveguide $w1h1$ has the widest bandwidth of the three waveguides at 11nm and therefore the lowest Q-factor (Q=140). Waveguide $w3h3$ has the narrowest bandwidth of 0.024nm and therefore the highest Q-factor (Q=64583). Waveguide $w2h2$ has a bandwidth in the middle of 2.7nm and whose Q-factor is also in the middle (Q=574). It should be noted that Figure 4.9 (c) looks very similar to Figure 4.7 (b). The significant difference is that in Figure 4.7 (b), the angle at which the infinitely wide TE beam was

launched towards the waveguide was different for each of the three waveguides having different Q-factors. In Figure 4.7 (b), by changing the angle of excitation, the resonance wavelength could then remain fixed. On the other hand, in Figure 4.9 (c), all three waveguides of varying Q-factor were excited at the same angle of incidence and the resonance wavelength remained fixed.

This shows that by selecting waveguides of varying width and height and therefore loss, yet still having a fixed TM effective index, the waveguide bandwidth or Q-factor can be varied while the TE coupling angle and the resonance wavelength remain fixed.

4.2.6 Summary

In Section 4.2.3 it was shown that the thin-ridge resonators were effectively similar to classical Lorenzian resonators, which could be modelled as LC circuits. In Section 4.2.4.1 it was shown that the resonant properties of these thin-ridges could be achieved by adjusting the waveguide width, but it was also necessary to adjust the incident angle in order to keep the incident TE beam and TM mode phase matched. In Section 4.2.5 it was shown that by introducing two independent variables to the waveguide geometry - the waveguide width and height, it was possible to adjust the waveguide Q-factor while keeping both the resonant wavelength and the incident angle constant. These findings are very significant. It is now possible to conceive a system with a single infinitely wide TE beam that interacts with a sequence of parallel thin-ridge resonators that are all designed to resonate at the same frequency but with Q-factors that can be engineered by adjusting the waveguide width and height. In this situation, all of the resonators would be coupled to each other via similar TE beams propagating in the forward and backwards directions. This is a very similar arrangement to a coupled resonator optical waveguide (CROW) or more generally a classical elliptical filter prototype. The opportunity to design such a filter will be explored in the next section.

4.3 Optical filter design using thin-ridge waveguide resonators

It has been shown in Section 4.2 that a thin-ridge waveguide behaves as a resonator when illuminated by an infinitely wide TE beam. It was also shown that the Q-factor of a thin-ridge waveguide resonator is dependent on the waveguide width and height dimensions. The possibility of being able to adjust the Q-factor or bandwidth of a resonator opens up opportunities that can exploit the adjustable spectral filtering properties of a single resonator. A common application of resonators is in the synthesis of filters as discussed in Section 4.1.2.2; especially higher order filter responses. An individual thin-ridge waveguide resonator behaves as a filter of the first order. By cascading several resonators in a prescribed topology it is possible to realize more complex higher order filter responses such as Butterworth, chebyshev or elliptic filter functions [173, 177]. These filter functions have desirable spectral features such as extremely sharp transitions from the pass-band to the stop-band as well as minimal attenuation in the pass-band.

The synthesis of higher-order filters has been well established in microwave electronics and can be done abstractly independent of the implementation of the resonator [177]. The resonator can take any form such as a capacitor-inductor lumped element resonator, a quarter-wavelength microstrip line, a dielectric cavity resonator or an optical ring resonator. Provided the fundamental individual resonator response is present, then conventional synthesis methods [177] can be used to design a higher order filter response using any type of resonator. Some of the optical filter synthesis methods that have been used [173] are indeed based on the conventional microwave filter synthesis techniques. It was shown in Section 4.2.3 that a thin-ridge waveguide has a fundamental resonator response similar to that of canonical lumped element resonators.

The proximity of the resonators in a filter is also an important factor and determines the type of filters that can be synthesized since the spacing between the resonators strongly influences the out-of-band characteristics of the filter [177]. Optical ring resonators are large structures relative to the wavelength of operation. Cascading ring resonators together requires that the minimum center to center separation has to be twice the ring radius without even taking into ac-

count the evanescent coupling between the rings, which increases this separation requirement further. For example, a ring resonator of 10μm radius requires a minimum separation of more than 20μm between cascaded resonators. This has been identified as a limiting factor in the synthesis of filters using ring resonators [173].

It was shown in Section 4.2.3 that it is possible to design an individual thin-ridge resonator to have equivalent properties to an LC resonator. Given that it is possible to independently adjust the resonant properties of each of an array of thin-ridge resonators while still having them coupled via the same infinitely wide TE beam, the question arises: can the process used to design microwave filters, and which has been used to design higher order optical filters [173], be used to also design higher order thin-ridge waveguide based filters?

To synthesize a filter requires the selection of a specific number of resonators, each having a specific Q-factor [173]. The filter order N specifies the number of resonators required. The Q-factor of each resonator in the filter is obtained from the low-pass prototype filter element values, also called g-values. These g-values represent the relative Q-factors between the individual resonators in the filter. The g-values are readily available from filter tables for either Butterworth or chebyshev filters in most microwave filter synthesis books [177, 178]. As shown in [173] the g-value directly corresponds to the Q-factor of each resonator by the relationship;

$$Q_q = \frac{FSR}{g_q.B} \tag{4.9}$$

where Q_q is the Q-factor of the resonator q, in which $q = 1...N$. The FSR is the free-spectral range. The g-value g_q is the low-pass prototype element g-value for each resonator and B is the filter bandwidth. The Q-factor Q_q of each resonator is evaluated at the same wavelength of resonance. It was found that the bandwidth of each resonator q could hence be evaluated as

$$B_q = \frac{1}{2} g_q.B \tag{4.10}$$

If the separation between the resonators is set to an odd multiple of quarter wavelengths [173] when cascaded, the response of the cascaded resonators to a

specified input will result in a specific predetermined filter response. It was shown shown in Section 4.2.5 that by using waveguides of varying width and height it is possible to have thin-ridge waveguide resonators with varying Q-factors that are coupled to an infinitely wide TE beam at the same angle. This also means that they are resonant at the same wavelength. On this basis, it is proposed that it should be possible to design complex higher order filters using thin-ridge waveguide resonators.

4.3.1 Third-order Chebyshev filter

In this section it is investigated whether it is possible to design a very simple higher order filter from thin-ridge waveguide resonators. The simplest filter to synthesize after a single resonator filter is a third order filter because a second order is actually more complex to design [177]. If the correct thin-ridge waveguide resonators for a third-order filter can be obtained and cascaded in a parallel filter topology, it is expected that the response should be similar to that of an ideal third-order filter.

The filter synthesis method used in this section is the same method presented in [173], which is an adaptation of the conventional microwave filter synthesis approach. As an example, a third-order Chebyshev filter with a bandwidth of 1nm and a ripple size of 0.5dB in the pass-band was chosen. The 0.5dB ripple was selected since the filter prototype values are readily available in a filter synthesis book [177]. The 1nm bandwidth was selected because it is in a range similar to those found for the thin-ridge waveguide resonators simulated in Section 4.2.5 and should therefore be attainable. For the third order Chebyshev filter with 0.5dB ripple and 1nm bandwidth the g_q values obtained were $g_1 = 1.5963$, $g_2 = 1.0967$ and $g_3 = 1.5963$. The corresponding resonator bandwidths were calculated from Equation (4.10) and were found to be $B_1 = 0.798nm$, $B_2 = 0.548nm$ and $B_3 = 0.798nm$.

The next step was to find the three waveguide dimensions that have the same TM mode effective index, meaning same resonance wavelength and angle, but each with their own bandwidths B_1, B_2 or B_3. To do this a search algorithm, presented in Appendix A, was written which takes a given TM mode effective

index and bandwidth. It then searches the 2D plot of Figure 4.9 (b) to find waveguide dimensions on the contour line having the specified TM mode effective index evaluated using the mode matching technique. In this case, the TM mode index of the waveguides in the third order filter was chosen to have a value N_{TM}=1.8. This effective index contour was seen in Figure 4.9 (b) to traverse a range of widely varying waveguide Q-factors. Once the contour line of constant TM mode effective index is found the algorithm then searches for the waveguide height and width dimensions along this contour line that gives a resonance response with the specified bandwidth. The response is evaluated using the eigen mode expansion method and the bandwidth of this response is evaluated by fitting the filter response to a Lorentzian function. A more detailed step-by-step description of this algorithm is given in Appendix A. The width and height dimensions that were found for the third order Chebyshev filter resonators are shown alongside Figure 4.10 (a).

In the cascaded filter topology, the center to center separation between the resonators must be equal to an odd multiple of quarter wavelengths [173]. Therefore, the wall to wall separation (S) between two resonators was evaluated using the technique outlined in Appendix A. Evanescent coupling can affect the resonance response of the individual resonator by altering the individual resonators TM mode effective index [13] and thus the wall to wall separation was made larger than 5μm to minimize evanescent coupling.

The TE beam angle was evaluated as 49.29° as described in Section 4.2.5 and using the eigen mode expansion method the TE beam was launched at an angle of 49.29° towards the three cascaded waveguide resonators illustrated in Figure 4.10 (a).

As a comparison, the response of an ideal lumped element third-order Chebyshev filter, composed of parallel LC resonators as shown in Figure 4.10 (b), was also simulated. The synthesis process that was used for designing this ideal LC filter is the conventionl microwave filter synthesis method [177]. The LC resonators were separated by an ideal impedance inverter which is essentially a 90° phase shifter. The response of this filter was evaluated by finding the input impedance of the filter and evaluating the reflection and transmission coefficients [177]. A comparison was then made between the transmission coefficients of the lumped

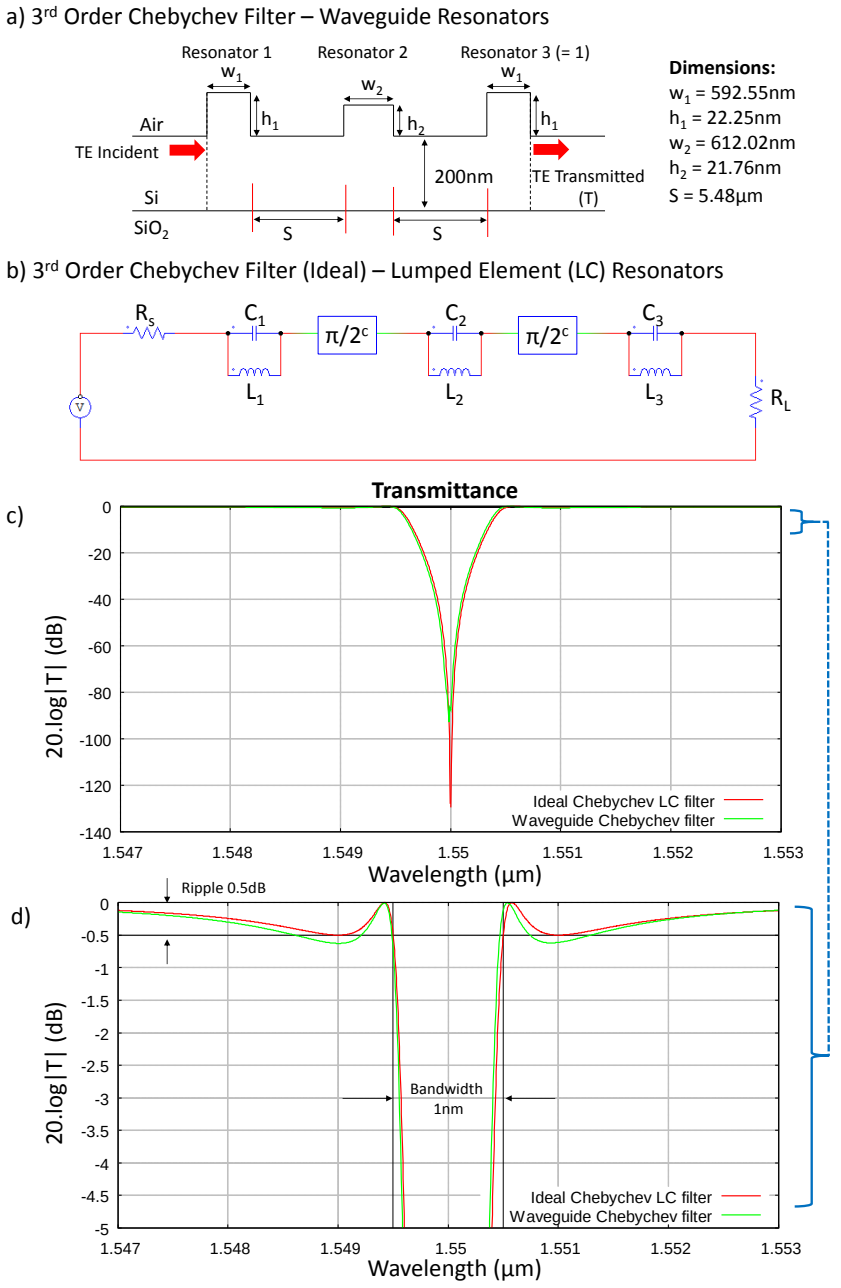

Figure 4.10: (a) Waveguide topology of 3^{rd} order Chebyshev filter composed of three waveguides. (b) Schematic of a 3^{rd} order lumped element (LC) Chebyshev filter. (c) Shows the evaluated transmittance of the waveguide and LC filter topologies and (d) highlights the ripple in the range between 0dB to -5dB.

element Chebyshev filter and the thin-ridge waveguide Chebyshev filter.

Figure 4.10 (c) shows the transmission coefficient for the waveguide Chebyshev filter and the ideal LC Chebyshev filter. Figure 4.10 (d) highlights the region from 0dB to -5dB. The ideal LC filter response has an exact ripple size of 0.5dB and 1nm bandwidth as was the design criteria for the filter. There appears to be a very good agreement between the ideal LC filter response and the response of the waveguide based Chebyshev filter.

There are some minimal differences observed in the two filter responses in the ripple region and these could be numerical or phase errors. Nonetheless, these results show that indeed it is possible to synthesize, with a high degree of accuracy, a simple third-order Chebyshev filter utilizing thin-ridge waveguides. It would be useful to investigate the minimal errors observed in the filter ripple, whether they are phase related and increase with the filter order.

4.3.2 Fifth-order Chebyshev filters

The synthesis of a simple third-order Chebyshev filter using thin-ridge waveguide resonators was shown to be possible in Section 4.3.1. The agreement between the third-order response of the ideal Chebyshev filter response and the thin-ridge waveguide filter was very good. However minor discrepancies were observable in the waveguide filter response. It is important to investigate whether these minor errors are constant and not dependent on the filter order or whether they scale up with the increase in filter order.

A fifth order Chebyshev filter was synthesized using thin-ridge waveguide resonators. The target filter had a 1nm bandwidth and a ripple size of 0.5dB similar to Section 4.3.1. The same method as described in Section 4.3.1 was used to find the corresponding resonators for the filter and also to determine waveguide separations in the filter topology shown in Figure 4.11 (a). For the fifth order Chebyshev filter with 0.5dB ripple and 1nm bandwidth, the g_q values obtained were $g_1 = 1.7058$, $g_2 = 1.2296$, $g_3 = 2.5408$, $g_4 = 1.2296$ and $g_5 = 1.7058$. The corresponding resonator bandwidths were therefore evaluated from Equation (4.10) as$B_1 = 0.853nm$, $B_2 = 0.615nm$, $B_3 = 1.27nm$, $B_4 = 0.615nm$ and $B_5 = 0.853nm$. The waveguide dimensions obtained for the resonators are shown

alongside Figure 4.11 (a). As a comparison, an ideal fifth-order Chebyshev filter was synthesized using lumped element resonators as was done in Section 4.3.1 and whose configuration is shown in Figure 4.11 (b).

Figure 4.11 (c) shows a comparison of the transmission coefficient for the ideal fifth-order lumped element Chebyshev filter and the fifth-order thin-ridge waveguide filter. From this perspective there is quite a good similarity between the two responses. However, Figure 4.11 (d) highlights the 0dB to -5dB range showing the ripples near the band edge of the two filter responses. The Chebyshev filter was designed to have a 0.5dB ripple which is true for the ideal lumped element filter but not for the thin-ridge waveguide filter. The ripple for the thin-ridge waveguide filter reaches about 0.8dB in size which is an error of about 0.3dB. This accounts for about a 60% error in the ripple size which is much greater than what was observed in the third-order Chebyshev filter in Figure 4.10 (d). It should also be noted that this error is observed in the second set of ripples rather than in the first set which are closer to the band edge.

Since the algorithm used was the same for the third and fifth order filters, the increase in error must be due to the increase in the number of resonators. The main difference to consider between the third and fifth order filters is the separation distance between the first and last resonators. As mentioned in Section 4.3.1, the individual resonators are well separated by a distance greater that 5μm so as to minimize evanescent coupling between the waveguides which may otherwise affect their individual resonance response.

Therefore, as the filter order increases the separation from the first to last resonator also increases. The separation between resonators is supposed to have an optical length equal to an odd multiple of a quater wavelength (90°) at resonance. However, the optical length of the slab waveguide separating the resonators is a function of wavelength. Therefore, the separation would acquire a slightly different optical length when the wavelength changes, which is essentially a phase error. The larger the wavelength shift the larger this phase error would become. This may explain why the error is bigger in the outer ripple of the filter response rather than in the inner ripple nearer to the band edge.

This phase error is not observed in the LC filter response because the ideal separation between the resonators is set to a 90° phase shift at all wavelengths,

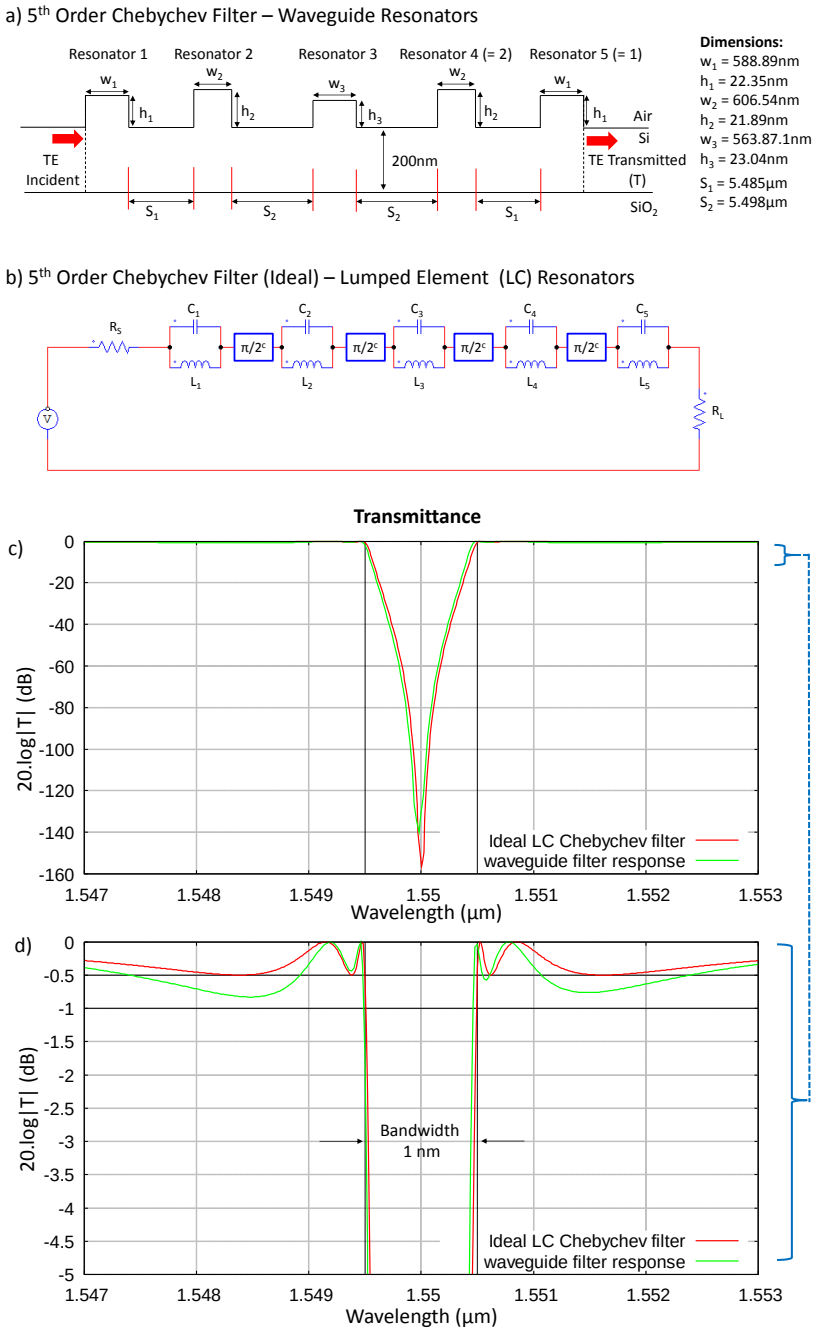

Figure 4.11: (a) Waveguide topology of 5^{th} order chebyshev filter composed of five waveguides. (b) Schematic of a 5^{th} order lumped element (LC) Chebyshev filter. (c) Shows the evaluated transmittance of the waveguide and LC filter topologies and (d) highlights the ripple in the range between 0dB to -5dB.

referred to as an ideal impedance inverter [177]. In fact wavelength dependent phase error due to the separation between the resonators is a common problem in microwave filter implementations when utilizing transmission line separations between resonators in a filter [177]. In microwave engineering, there are advanced circuit design alternatives to using transmission line separations between resonators [177]. For now, the thin-ridge waveguide filter is designed to use these waveguide separations between the resonators. However, this provides room for future work on how to ingeniously implement optical filters to overcome this phase error problem.

In summary, this thin-ridge waveguide fifth-order Chebyshev filter response can be considered to be realizable. However, there were errors in the pass-band ripple which resulted in the 1nm bandwidth filter having a 60% error in the ripple. It is believed that this error may be due to the use of separations between the resonators which results in a phase error that is wavelength dependent. It would be interesting to investigate if there are other alternatives to using wide separations between the resonators as has been done in microwave electronics.

4.3.3 Effect of the separation between resonators on filter response

It was shown in Section 4.3.2 that for a waveguide based fifth order Chebyshev filter, an error exists in the ripple of the filter response. It was proposed that this may due to a phase error caused by the wavelength dependent nature of the optical length between the resonators. Since the separation is set to have an optical length equivalent to a 90° phase shift at resonance, the phase error becomes larger as the wavelength shifts further away from resonance. If this is indeed the case, then an equivalent lumped element Chebyshev filter which has similar transmission line separations between the resonators should have the same response as the thin-ridge waveguide filter observed in Section 4.3.2.

To test this, the filter response of the fifth-order thin-ridge waveguide filter observed in Figure 4.11 (c) and (d) was compared to an LC filter where the separation between the LC resonators had been replaced with transmission lines. The transmission lines had a fixed propagation constant over the entire wavelength

range. The transmission line separations between the LC resonators were made to be of equal length, and therefore phase delay, to those of the thin-ridge waveguide filter. This topology is shown in Figure 4.12 (a). The separation values are labeled as S_1 and S_2 which are equal to the center-center waveguide separation in the filter topology of Figure 4.11 (a).

Figure 4.12 (b) shows the transmission coefficient of the thin-ridge waveguide Chebyshev filter as well as that of the LC filter with transmission line separations between the resonators. Similar to what was observed in Figure 4.11 (b), there is very good agreement across the overall filter spectral response. Figure 4.12 (c) highlights the 0dB to -5dB range, which shows more closely the ripple of the Chebyshev filter response which was designed to be 0.5dB. There is a very good similarity in the ripple of the thin-ridge waveguide filter and the LC filter which has transmission line separations between the resonators. There are still some minor differences similar to what was also observed for the third-order Chebyshev filter of Section 4.3.1.

This small difference may be due to the dispersion of the waveguide mode effective indices. This means that the mode effective index of both the incident TE beam and the waveguide mode is not constant but varies slightly with wavelength. The LC filter on the other hand was simulated with a transmission line having a constant propagation constant at all wavelengths. This dispersion in the waveguide is not in emulated in the LC filter and may be causing the slight discrepancies between the two filters in Figure 4.12 (c).

From the results of Figure 4.12 (c), it is clearly evident that the error in the ripple size that was observed for the fifth-order waveguide Chebyshev filter in Figure 4.11 (d) is similar to that observed for the ideal LC filter with transmission line separations. This affirms that this phase error is due to the transmission line separations present between the resonators. Also, the phase error affecting the ripple only has significant consequence farther away from the resonant frequency. Limiting or reducing the bandwidth of the filter may be one way of decreasing the effect of the transmission line phase error on the ripple.

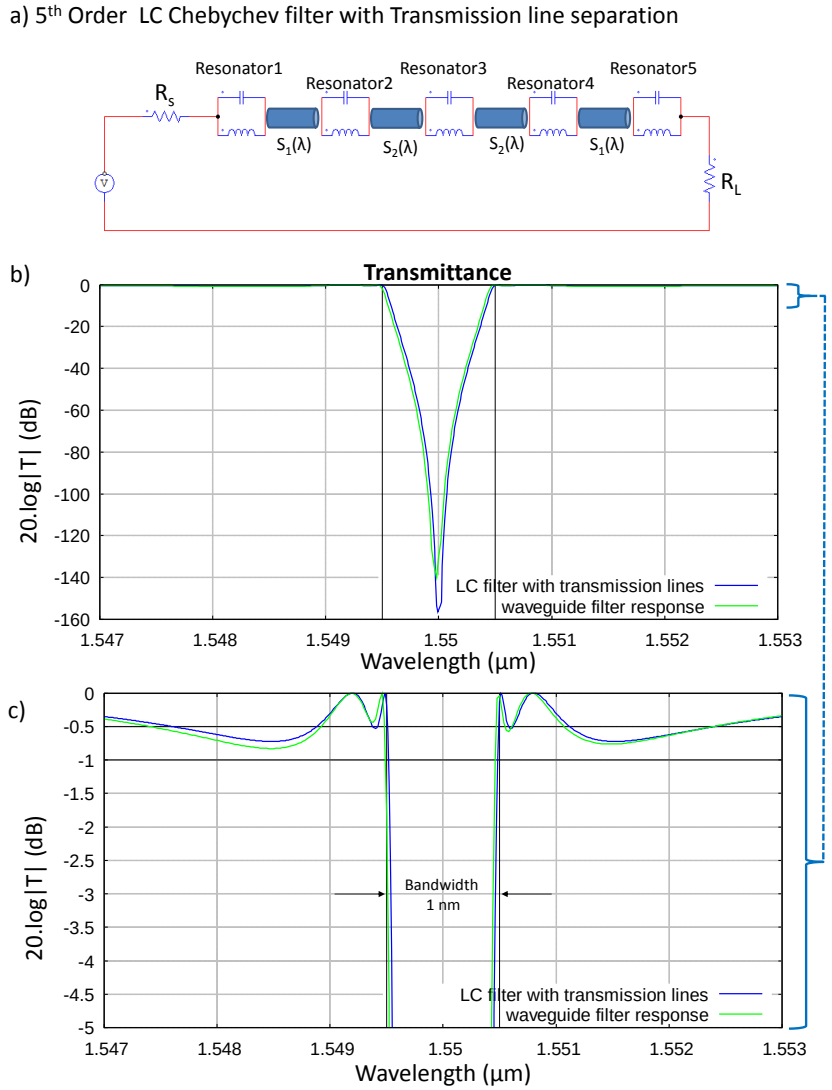

Figure 4.12: (a) Schematic of a 5^{th} order lumped element (LC) Chebyshev filter with transmission line separations between resonators (b) Shows the transmittance of the LC filter with transmission lines in comparison to the waveguide filter response. (c) Highlights the filter response in the range between 0dB to -5dB.

4.3.4 Narrowband Fifth-order Chebyshev filters

It was shown in Section 4.3.3 that the separation between the thin-ridge waveguide resonators in a fifth order Chebyshev filter caused the errors seen in the ripple of the filter response in Figure 4.11 (d). This phase error was shown to be due to the wavelength dependence of the optical length in the separation between the resonators. Farther away from resonance this phase error becomes larger since there is a greater shift from the resonance wavelength. It would stand to reason that reducing the bandwidth of the filter should therefore reduce this phase error and therefore improve the accuracy of the filter response.

To investigate this hypothesis the bandwidth of the fifth-order 0.5dB-ripple Chebyshev filter was decreased from 1nm to 0.3nm. The same simulation method as in Section 4.3.1 was used to synthesize the filter. Exploiting Equation (4.9), the bandwidths of the 0.3nm fifth-order Chebyshev filter resonators were simply evaluated by multiplying the 1nm fifth-order Chebyshev filter resonator bandwidths of Section 4.3.2 by a factor of 0.3. Therefore, The individual resonator bandwidths changed to $B_1 = 0.256nm$, $B_2 = 0.185nm$, $B_3 = 0.381nm$, $B_4 = 0.185nm$ and $B_5 = 0.256nm$.

From the resonator bandwidths, the waveguide dimensions of the thin-ridge waveguide resonators were evaluated as in Section 4.3.1. The first and fifth waveguide resonators had dimensions of w_1=651.5nm and h_1=20.8nm. The second and fourth waveguide resonators had dimensions of w_2=661nm and h_2=20.6nm. The third waveguide resonator had dimensions of w_3=638nm and h_3=21.1nm. The waveguide separations S_1 and S_2 as depicted in Figure 4.10 were evaluated as 5.426μm and 5.433μm respectively. The filter wavelength response was then simulated when a TE beam was launched at an angle of 49.29° using the eigen mode expansion technique. A comparison was made to the wavelength response of the equivalent LC filter with ideal and transmission line separations between the individual resonators.

Figure 4.13 (a) shows the overall transmission coefficient response for the thin-ridge waveguide filter, the ideal LC filter and the LC filter with transmission line separations between the resonators. Figure 4.13 (b) highlights these filter responses in the 0db to -5dB range. The maximum difference between the

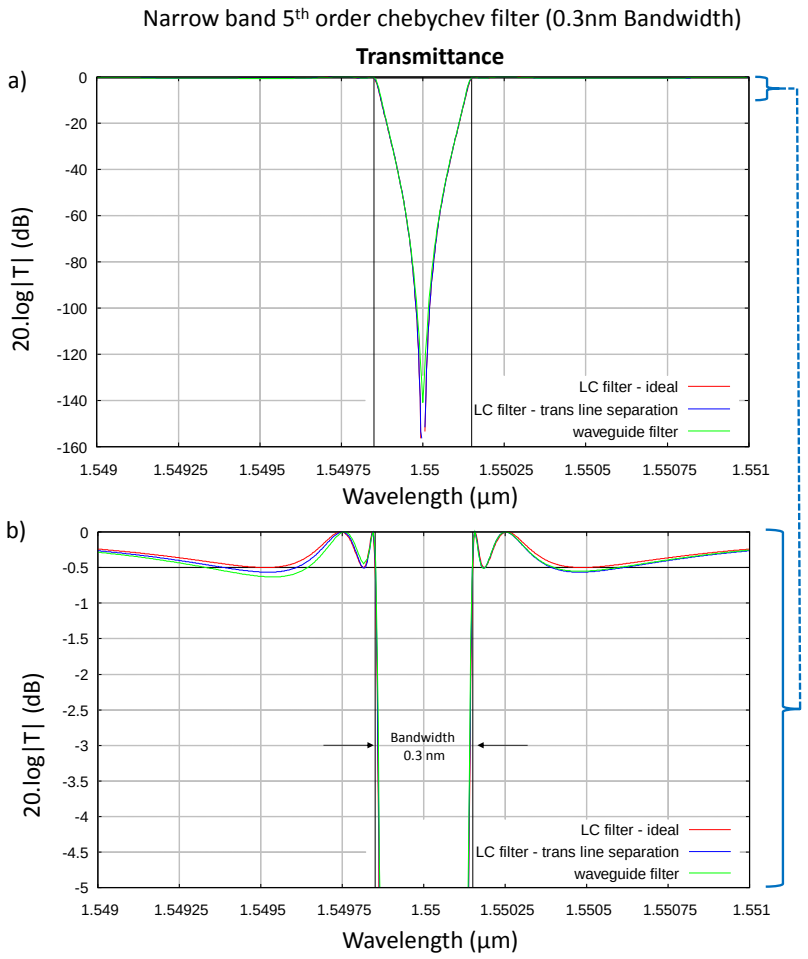

Figure 4.13: (a) Shows the transmittance of the 0.3nm waveguide filter as well as that of the LC filter with ideal and transmission line separations. (c) Highlights the filter response in the range between 0dB to -5dB.

waveguide and ideal LC filter response in the ripple is approximately 0.1dB. In comparison to the 0.3dB error seen in the 1nm Chebyshev waveguide filter in Figure 4.11 (d), there is about a 60% reduction in the phase error. This is approximately equal to the 60% reduction in the bandwidth from 1nm to 0.3nm, which means the improvement in phase error is almost proportional to the decrease in bandwidth. It is also noted that there is a slight difference between the waveguide filter response and that of the LC filter with transmission line separations.

As discussed in Section 4.3.3, the difference between the waveguide filter and the LC filter with transmission lines is likely due to waveguide dispersion. However, the LC filter with transmission lines has a fixed propagation constant at all wavelengths.

These results show that decreasing the filter bandwidth has reduced the phase error observed in the ripple. This reduction in phase error in the filters ripple is due to the fact that within the reduced bandwidth of the filter the transmission line separations between the resonators have an optical length very close to 90°. Therefore the transmission line separations behave as almost ideal (90°) separations between the resonators within this narrow filter bandwidth.

However, there is clearly a trade-off that must be made when designing higher order filters from thin-ridge waveguide resonators when using waveguide separations. Increased bandwidth comes at a cost of increased phase errors. Smaller bandwidths on the other hand result in a more accurate filter response.

4.4 Discussion

It should be emphasized again that the investigations of Chapter 4 on the thin-ridge waveguide resonators and filters all used the approximation that the excitation took the form of a slab mode. This slab mode is essentially a slab beam of infinite width such that in the longitudinal direction of propagation, the TE excitation that is incident on the waveguide structure is invariant. This approximation is useful when analysing the resonance effect but is not realistic. In practice, the excitation would take the form of a beam of finite width. It is expected that the frequency response characteristics such as the line width of the

thin-ridge waveguide resonators and filters would be dependent on the shape of the excitation beam used. Investigating the response of the proposed resonator and filter structures of Chapter 4 using realistic finite width beam profiles would be a recommended next research step before trying to experimentally demonstrate the thin-ridge resonance effect.

Further, to improve the filter synthesis techniques used for designing thin-ridge waveguide based filters, one important hurdle needs to be overcome. In Section 4.3, a filter was synthesized by finding it's constituent resonators having specific Q-factors through a numerical approach described in Appendix 1. Summarily, this numerical approach manually scans through a range thin-ridge waveguide dimensions and evaluates their Q-factors to find the specific resonator dimensions that give the desired resonator Q-factors of the filter. While this process has been shown to work, it is not an analytic method and is not easily scalable. A more desirable analytic approach would be to design the filter from its fundamental basis, possibly describing it in poles and zeros form, and then finding the necessary resonator coupling coefficients that would give the desired filter response. An additional step would then be to relate the resonator coupling coefficients to the physical thin-ridge waveguide dimensions. Such an analytical synthesis approach would not only be elegant but also be easily scalable and flexible.

The thin-ridge resonator has highlighted some advantageous characteristics due to its topology that can be highlighted by comparing the proposed thin-ridge waveguide resonator to the state of the art.

Free Spectral Range (FSR)

Interpretation: The spectral separation between resonance peaks. This is inversely proportional to the cavity length.

- *Thin-ridge waveguide resonator:* Is determined by the cross sectional width of the waveguide since the resonant cavity is defined by the waveguide walls.
- *State of the art waveguide resonators:* In ring and disk resonators, the free spectral range is dependent on the radius of the microcavity.

The small cross section of the waveguide means that the resonant TM mode

of the waveguide has a very short optical path length or round trip within the resonator resulting in a wide free spectral range. Unlike a ring resonator, a thin-ridge waveguide resonator can have sub-micron dimensions per round trip, which could potentially yield a much wider FSR than is possible for example with ring resonators whose minimum radius is limited by bending loss.

Q-factor / Bandwidth

Interpretation: The Q-factor refers to the lifetime of a trapped photon within the resonant cavity. The bandwidth is inversely proportional to the Q-factor.

- *Thin-ridge waveguide resonator:* The Q-factor of a thin-ridge resonator depends on the TE-TM coupling coefficient of the waveguide. The coupling coefficient is determined by the waveguide width as well as the etch depth or height of the waveguide walls. Scattering loss from any random inhomogeneity such as sidewall roughness can also limit the resonator Q-factor.
- *State of the art waveguide resonators:* The Q-factor is dependent on the coupling coefficient between the bus waveguide and the ring/disk resonator which is controlled by their physical separation. Cavity losses such as scattering loss and bending loss are factors that also limit Q-factor.

Q-factors in excess of 1,000,000 have been demonstrated for rings these have very small coupling cooficients between the bus waveguide and the ring and the Q-factor is limited by scattering loss. Conversely, the scattering loss in a ridge resonator will be very low due to the very shallow ridge and the primary interaction of the TM mode with the polished top and bottom surfaces of the silicon slab. The Q of the ridge resonator is rather limited by the length of the ridge waveguide and thus it would be hard to imagine achieving Q-factors in excess of about 1000 for a ridge with length in the millimeter regime.

Non-linearity

Interpretation: Refers to the ability of a resonator to enhance, inhibit or influence non-linear phenomena within the resonant cavity which is dependent on field intensity within the resonator.

- *Thin-ridge waveguide resonator:* Is dependent on the length of the waveguide resonator since the optical intensity is distributed along the waveguides length.

- *State of the art waveguide resonators:* In ring and disk resonators, the optical intensity is dependent not only on the size/radius but also on the Q-factor due to the recirculation of light within the cavity.

The relatively low Q-factor that could be expected for ridges will ensure optical intensity can be kept moderately low along the length of the thin-ridge waveguide resonator thus minimizing non-linear effects. In rings, the much higher Q-factor in the closed loop of ring/disk resonators can lead to intensity build up which can enhance susceptibility to non-linear effects. In the case where nonlinearity is desired a higher optical power could be used. In the case of a ridge resonator, the optical power is delivered by a distributed TE beam only becoming concentrated into a mode when interacting with the ridge resonator. This will ensure that nonlinearity only occurs in the ridge itself. In the case of a relatively low Q-factor ring, the nonlinear response of the nanowire waveguide interfacing the ring might be significant.

Sensitivity to fabrication tolerance and environmental parameters
Interpretation: Refers to changes in resonator characteristics under the influence of physical changes from fabrication or environmental effects.

- *Thin-ridge waveguide resonator:* Waveguide height and width, waveguide separation and waveguide evanescent coupling are all dimensional properties that can affect the resonance characteristics of single or coupled resonators. Temperature fluctuations are also expected to alter the TE-TM phase matching conditions in the resonator thus shifting the resonance wavelength. However, the resonant TM mode guided in the cladding would not be expected to experience a significant thermal change due to the silicons high thermal coefficient.

- *State of the art waveguide resonators:* A similar set of three properties in a ring/disk resonator can also affect resonance characteristics. These are bus-

ring waveguide separation, length of the bus waveguide between adjacent resonators and the proximity of adjacent resonator waveguides such that the two resonators are evanescently coupled. Temperature has a significant effect in ring resonators by altering the rings optical length resulting in a shift of the resonance wavelength. The coupling coefficient can also be varied by temperature. There is a greter susceptibility in ring resonators to thermal fluctuations since a TE mode is utilized which is strongly confined in the silicon waveguide.

The generally lower Q-factor of ridges will lead to less sensitivity to environment and dimensional variations than high Q-factor rings. However, even for similar Q-factor rings, it is anticipated that ridge resonators would offer improved robustness when compared to rings. Firstly, the susceptibility of the thin-ridge resonator to temperature fluctuations may not be as significant as in ring resonators since the resonant TM mode in the thin-ridge waveguide has a significant portion of its power in the evanescent field in the cladding (air) as opposed to the resonant TE mode often used in ring resonators that is confined mostly in the silicon. Secondly, the coupling between the TE beam and the TM resonance for a ridge resonator is distributed over the length of the ridge, hence any geometric or environmental variations will be averaged over this entire length. Conversely, the coupler in the ring resonator is highly localized and thus small variations can make a significant difference to the resonant properties of the ring. The coupler for a ring also often relies on very precise and fine features in the gap which can be subject to fabrication errors. Hence, rings often require active and independent tuning of both the ring effective index and the directional coupler. This active control may not be required for the ridge resonator.

Control of coupled resonator filter characteristics

Interpretation: This refers to the geometric parameters of a coupled resonator system that can be exploited for engineering filter characteristics such as bandwidth, FSR and extinction ratio.

- *Thin-ridge waveguide resonator:* Waveguide dimensions, which alter the lateral leakage coupling strength, vary the amplitude of coupling in a cou-

pled resonator system as well as the FSR. Independently of the waveguide dimensions, the separation between resonators alters the phase of coupling in a coupled resonator system.

- *State of the art waveguide resonators:* In ring coupled resonator systems, the dimensions of the resonators determines the filter characteristics such as the FSR, but also impacts the separation or phase of coupling that can be obtained between adjacent resonators.

In coupled thin-ridge resonators, the resonator dimensions and separations can be independently tuned to engineer the filter response which offers significant flexibility when synthesizing coupled resonator filter systems especially when compared to coupled ring resonators whose ring dimensions and separations cannot be independently adjusted for filter synthesis due to their interdependence.

4.5 Conclusions and Future Work

This chapter was motivated by an observation made in Chapter 3 where a TE beam incident on a thin-ridge waveguide grating structure appeared to be strongly reflected in spite of a weak index perturbation at the interface of the grating structure. In this chapter this reflection effect was analysed in a simple scenario where the waveguides are well separated and not evanescently coupled unlike the grating of Chapter 3. This effect was directly linked to a resonant TE-TM coupling effect in the thin-ridge waveguide that results in a strong and sometimes complete reflection of an Incident TE beam. An analysis of this periodic bandgap structure ranging from closely-spaced evanescent coupling to long range coupling via TE lateral leakage would constitute an entire investigation in its own right and is proposed for future work. This section summarizes the findings and potential applications of this resonant reflection effect.

In this chapter it has been shown that when an infinitely wide TE beam is incident on a thin-ridge waveguide at an angle where it is phase matched to the TM mode of the waveguide, it can be resonantly coupled to the TM mode of the waveguide resulting in a strong reflection of the incident TE beam. It was shown that this resonant reflection is wavelength dependent and that the

spectral response in Lorentzian in shape. The Lorentzian resonance response of the thin-ridge waveguide was also shown to be identical to that of an ideal LC resonator in both amplitude and phase. It was also shown that the Q-factor of the resonance response is dependent on the waveguide dimensions of width and height. However, as a consequence of changing either the waveguide width or height dimensions, there was an observable shift in the resonance wavelength of the waveguide resonator. It was shown that in order to vary the thin-ridge waveguide's Q-factor without altering the resonance wavelength, it is necessary for both the waveguide width and height dimensions to be adjusted such that the TM mode effective index remains constant and consequently the angle and wavelength of resonance also remains constant.

A significant benefit of being able to adjust the resonators Q-factor while maintaining a fixed wavelength of resonance and angle of incidence is that it is possible to consider the synthesis of higher order filters that require multiple resonators to be cascaded or coupled together. It was shown that it is possible to cascade thin-ridge waveguide resonators to synthesize higher order filter responses such as third and fifth order Chebyshev responses. The cascaded resonators were sub-wavelength in cross section and had a very small separation of about 5μm between resonators resulting in a small filter cross section. As such it is believed that it is possible to cascade a large number of thin-ridge waveguide resonators into a small area on a chip.

A drawback that was identified is the fact that the bandwidth is also limited for high order filters due to phase-errors that exist further away from the resonance wavelength. It is believed that these phase errors can be further mitigated if a technique is devised for cascading resonators with even smaller separations between adjacent waveguides. Such a technique would have to contend with strong evanescent coupling between resonators which could alter the TM effective index of the waveguide resonator.

It is also evident that the proposed approach of varying the waveguide height and width to maintain constant TM effective indices in all the waveguide resonators makes fabrication of such devices more difficult due to the multiple waveguide etch depths required. A proposed future investigation is to devise a different approach for maintaining a constant TM effective index in the waveguides while

still being able to adjust the Q-factor of the resonator. This new approach should rely on using waveguide structures of a uniform height and can consequently be fabricated in a single etch step.

Chapter 5

Thesis conclusions and future work

Summarizing the key points you can find in Sections 2.5 3.10 and 4.4, the main motivation for this research was to investigate possibilities of exploiting the lateral leakage radiation phenomenon, which is a TM-TE coupling effect present in SOI thin-ridge waveguides. One primary goal was to investigate if the TM-TE coupling could be used as a biosensor. This is due to the difference in the evanescent field strengths between the TE and TM polarizations, which could be used to sense refractive index changes on the waveguide surface. It was found that the proposed taper sensor that utilises the lateral leakage effect was characteristically very similar to Mach-Zehnder Interferometric sensors. The main difference was the fact that in the taper sensor, while the sensing arm is the TM mode of a thin-ridge waveguide, the reference arm is coherent TE radiation that can be collected and measured.

Another goal was to show that this inherent TM-TE coupling phenomenon could be utilized for polarization conversion between the TE and TM polarizations. The proposed grating polarization rotator was shown to be effective for polarization conversion and that potentially its bandwidth and efficiency, like in a conventional grating, could be controlled via the gratings parameters such as number of periods, duty-cycle and even apodization. It was also identified that there is a potential in the proposed grating for both polarization rotation and splitting.

A consequence of the investigation on polarization conversion was that strong

reflections were observed when a TE beam was incident on a thin-ridge waveguide grating structure. It was believed that this behaviour was due to a resonance effect. It was proposed that the thin-ridge waveguide, when illuminated by a TE beam, fundamentally behaves as an optical resonator and that several of these resonators could be cascaded to form higher order filters. Although long, one benefit of thin-ridge waveguide resonator is its small lateral dimension which can be sub-wavelength in width allowing realization of laterally compact coupled resonator topologies. This also means that the confined optical intensity, which is distributed over the entire length of the waveguide can be kept moderately low potentially minimizing non-linear effects. In addition to this, the small lateral dimension of the waveguide means that the resonant TM mode of the waveguide has a short optical path length which could potentially yield a much wider free spectral range than is possible with other resonator types such as ring resonators. Another significant benefit of thin-ridge waveguide resonators would be the small height of the ridge sidewall which minimizes side-wall scattering loss and consequently could enable higher Q-factor resonators to be realized. In addition the susceptibility of the thin-ridge resonator to temperature fluctuations may not be as significant as in ring resonators since the resonant TM mode in the thin-ridge waveguide has a significant portion of its power in the evanescent field in the cladding (air) as opposed to the resonant TE mode often used in ring resonators that is confined mostly in the silicon.

5.1 Specific Outcomes

In Chapter 2 the biosensing capability of the lateral leakage phenomenon in thin ridge waveguides was explored through simulation. The main finding was that simulated biomolecules deposited on the surface of a TM propagating thin-ridge waveguide had the effect of altering the angle of the TE radiation generated by the waveguide. This was due to the fact that the TM mode, which is much more evanescent than the TE slab mode, was more strongly perturbed leading to a greater change in its phase velocity. The result was that the angle at which the TM guided mode was phase matched to the TE slab mode, which is the angle

that the TE radiation is launched at, also changed. The greatest rate of change in the TE radiation angle was observed to occur for biomolecular deposition near the surface. This rate of change decayed as the thickness of the simulated biomolecules increased. This is not surprising since the evanescent field also decays further away from the waveguide surface. However, this means that the sensitivity of the TM-TE coupling effect is highest nearer to the waveguide surface. A thin-ridge waveguide taper together with a lens structure was proposed as a possible sensor topology for observing refractive index changes caused by biomolecular deposition. It was shown through simulation that the TE radiation from a radiating thin-ridge waveguide taper could be collected via the integrated lens structure which focuses the TE radiation to an output waveguide positioned at its focal plane. The main observation here was that a varying TE radiation angle, caused by biomolecular deposition on the taper, shifted the focal point location where the TE beam was focused to. This consequently altered the amount of power coupled to the output waveguide. This provided a practical means for observing refractive index changes caused by biomolecules at the waveguide surface which altered the amount of power measured at the output waveguide. However, measurement of absolute power can be unreliable due to its potential susceptibility to fluctuations. It was proposed instead that the wavelength response of the waveguide taper should be observed instead. It was shown that the power coupled into the output waveguide was wavelength dependent. Maximum output power was observed at a specific wavelength and decayed as the wavelength shifted away from this central position. It was shown that this peak power wavelength position would shift when biomolecules were deposited on the taper surface. Consequently, it was possible to measure the wavelength shift associated with the maximum power coupled to the output waveguide. This would provide a more robust measurement technique for such a sensor topology.

Chapter 3 focused on the polarization conversion capabilities inherent in the TM-TE coupling relationship of a thin-ridge waveguide. The primary objective in this chapter was to devise a structure that could couple an incident TE beam into the TM polarization. It was proposed that by using a holographic approach it would be possible to design a polarization converting structure by overlapping the incident TE beam to the TM beam which it should couple to. It was shown that

if a TE and TM slab beam are superimposed, the resultant sinusoidal interference pattern resembles a grating. This interference pattern had a Gaussian envelope both along and across its profile. It was therefore expected that if such a structure could be designed on a silicon slab waveguide, then illuminating this structure with the original TE beam should generate the desired TM beam. To simplify such a grating structure, a binary approximation was used where the period was equal to that of the interference pattern but the grating height was uniform rather than Gaussian-shaped. Such a binary grating profile would be more practical to implement. The simulation of this structure using the eigenmode expansion technique showed that an incident Gaussian TE beam was successfully converted into the TM polarization. However, this conversion process occurred only within the first few periods of the grating indicating that the conversion process was occurring rapidly. Consequently, the TM beam launched from the grating had a narrow aperture and was therefore highly divergent. It was proposed that to generate a collimated Gaussian-like TM beam, similar to the incident TE beam, the binary grating structure would need to be apodized. Apodization was achieved by varying the duty cycle of the grating periods linearly. It was shown that when a TE beam was launched towards this apodized grating, it was efficiently converted into an equally collimated TM beam.

In Chapter 4, a subtle observation from Chapter 3 was investigated in which strong reflection occurred when a TE beam was incident on the thin-ridge grating structure. This reflection was greater than would be expected from conventional Fresnel reflection. It was believed that this behaviour was caused by resonant coupling between the incident TE field and the TM mode of the thin-ridge waveguide structure. It was hypothesized that a similar reflection phenomenon would occur even when a single thin-ridge waveguide was illuminated by a TE slab mode propagating at the correct angle to couple to the guided TM mode. A significant finding of this investigation was that not only was strong reflection observed when a thin-ridge waveguide was illuminated by a TE slab mode, but also varying the excitation wavelength resulted in a Lorentzian reflection response. This spectral response was observed to be identical in amplitude and phase to that of a conventional resonator of equal bandwidth. Another significant finding was that the resonance quality-factor (Q-factor), which also corresponds to the resonance

bandwidth, could be tuned by varying the waveguide width or height. However, as a consequence of changing either the waveguide width or height dimensions, it was necessary to adjust the incident angle to ensure that the TE beam remained phase matched to the TM mode with different effective index due to the change in either width or height. It was shown that in order to vary the thin-ridge waveguide's Q-factor without altering the required incident angle, it was necessary for both the waveguide width and height dimensions to be adjusted simultaneously, such that the TM mode effective index remains constant and consequently the required incident angle and wavelength of resonance also remains constant. Given the tunability of an individual thin-ridge waveguide resonator, it was believed that it would be possible to design cascaded coupled resonators to synthesize higher order filters with significantly sharper spectral responses than is possible with individual resonators. Using traditional microwave-based filter synthesis techniques, it was hypothesized that if resonators with the correct Q-factors were cascaded and then illuminated with a TE field propagating at a specific angle, it would be possible to obtain a higher order filter response such as a Chebyshev response. A third-order and fifth-order Chebyshev filter were synthesized by cascading thin-ridge waveguide resonators together. It was shown through simulation that the third and fifth order Chebyshev filter responses of cascaded thin-ridge waveguides were similar to that of an ideal filter. However, another finding was that increasing the filter order from three to five had the effect of distorting the observed filter response. It was shown that the distortion in the fifth order filter response was due to phase errors away from the resonance wavelength due to the wide filter bandwidth. It was shown that by keeping the filter bandwidth narrow, the thin-ridge waveguide fifth order filter response kept in good agreement with the ideal filter response.

5.2 Opportunities and future work

In all three chapters of this thesis, integrated optical structures were proposed that exploit the lateral leakage effect in thin-ridge waveguides. Of immediate relevance would be the fabrication and verification of these results through practical

experiment.

While the biosensor topology investigated in chapter 2 could work in principle, the research work in Chapter 3 and Chapter 4 availed the opportunity to develop much more sensitive and more compact potential biosensor topologies. One example could be to investigate the utilization of the thin-ridge waveguide filters in Chapter 4 as evanescent field biosensors due to their much sharper and narrower wavelength response than those observed for the waveguide taper in Chapter 2.

The polarization converting grating structure of Chapter 3 would be an interesting structure to fabricate and test. However, it is a three-levelled waveguide structure which would require multiple etch steps to fabricate. To make it easier to fabricate, it is proposed that investigations should be first directed at simplifying the grating structure into a two levelled structure that can be fabricated in a single etch-step. It is also believed that this grating could be investigated as both a polarization splitter and a rotator simultaneously. This is because if a TE beam and TM beam are simultaneously incident on the grating structure at an angle, it is expected that the TM beam should not interact with the grating at all and should be transmitted with minimal perturbation. The TE beam, as shown in Chapter 3, would be converted into the TM polarization and would be ejected parallel to the grating which is in a different direction to the incidence angle.

The work in Chapter 4 also opens up a significant opportunity for future research due to the fundamental resonance behaviour observed in the thin-ridge waveguide and the inherent advantages of such a resonator topology. Although long, one benefit of thin-ridge waveguide resonator is its small lateral dimension which can be sub-wavelength in width allowing realization of laterally compact coupled resonator topologies. This also means that the confined optical intensity, which is distributed over the entire length of the waveguide can be kept moderately low potentially minimizing non-linear effects. In addition to this, the small lateral dimension of the waveguide means that the resonant TM mode of the waveguide has a short optical path length which could potentially yield a much wider free spectral range than is possible with other resonator types such as ring resonators. Another significant benefit of thin-ridge waveguide resonators would

be the small height of the ridge sidewall which minimizes side-wall scattering loss and consequently could enable higher Q-factor resonators to be realized. Thin-ridge waveguide resonators also have several mechanisms for controlling coupling in a coupled waveguide structure such as the physical dimensions of width and height as well as the separations between resonator. This highlights the several degrees of freedom that can be utilized when engineering coupled thin-ridge waveguide resonator structures.

In regards to further investigations into this topic of resonance, it would be important to verify the resonance behaviour of thin-ridge waveguides through experiment. Another shortcoming identified is that varying the resonator Q-factor by altering the waveguide width and height makes the fabrication of these devices challenging. It would be more practical to develop a technique that varies the Q-factor of thin-ridge waveguide resonators while keeping the waveguide etch-depth constant. If a technique can be devised to vary a thin-ridge waveguide resonator's Q-factor while maintaining a constant waveguide etch depth, it would be beneficial to investigate through experiment the proposed optical filters in Chapter 4 using these uniform etch-depth resonators.

The ability to cascade several resonators together opens up several opportunities outside the scope of optical filtering for wavelength division multiplexing. As was found in the literature survey of Section 4.1.1, optical resonators have been exploited for various applications including optical sensing, lasers, non-linear devices, delay lines, optical modulation and optical switching. It should be possible to examine the thin-ridge waveguide resonator in these contexts.

In conclusion, the goal of this thesis was to investigate ways in which the lateral leakage phenomenon in thin-ridge waveguides could be exploited for applications in photonics. Through simulation, it was found that the lateral leakage phenomenon could be used for evanescent field sensing, polarization rotation and for resonant optical filtering. Several opportunities have been identified for future research but the most paramount would be the experimental verification of the applications of lateral leakage radiation presented in this thesis. In light of this, it is believed that the discoveries made within this thesis and the proposed future directions should provide fertile ground for several future PhD studies.

Appendix A

Filter synthesis using thin-ridge waveguide resonators

In this appendix the filter synthesis methods used to design the chebyshev filters in Chapter 4 are presented in more detail. The process of filter synthesis has been well developed in the field of electronics and microwave engineering [177]. In optical engineering the filter synthesis methods from microwave engineering have been exploited to design optical filters [173]. The common implementation of optical filters has been with the use of ring resonator structures [179]. The same synthesis approach from [173] was used to design higher order chebyshev filters in Chapter 4 using thin-ride waveguide resonators.

The first step taken in the filter synthesis process was to select the desired filter bandwidth and spectral shape. The filter shape is defined mathematically by the commonly known butterworth, chebyshev or elliptic filter functions [177]. These filter functions differ from each other in terms of the steepness of the roll-off from pass-band to stop-band as well as the ripple in these bands. The next step was to select the required filter order N. The order of the filter N is equivalent to the number of resonator elements that need to be included in the filter so as to obtain the desired filter response. Generally, the higher the filter order the steeper the spectral slope between the pass-band and stop-band. This enhanced

steepness may come at a cost of more ripples in the passband or stopband [177]. A detailed analysis of the filter functions and the filter orders is given in [177, 178].

Once the filter bandwidth, the filter function and the filter order had been selected then the individual resonator parameters of bandwidth or Q-factor could be determined. Obtaining the bandwidths of the N individual resonators that comprise the N-order filter will be covered in the first section of this appendix. The next subsection deals with the determination of the physical separation between the individual resonators in the overall filter topology.

A.1 Resonator selection

In Chapter 4, a third order $N = 3$ and a fifth order $N = 5$ filter were synthesized. From the desired filter of order N, one obtains from traditional filter synthesis the so called low-pass prototype filter element values commonly denoted as g values. Each element q in the low-pass prototype filter has an ascribed g_q value where $q = 1, 2..., N$. These values were readily obtained from a corresponding filter table for butterworth or chebyshev filters [177, 178]. As shown in [173] the $'g'_q$ value directly corresponds to the Q-factor of each resonator. The bandwidth of each resonator was evaluated as

$$B_q = \frac{1}{2} g_q . B \tag{A.1}$$

where B_q is the resonator half power bandwidth, g_q is the low-pass prototype element value and B is the half power bandwidth of the filter response.

Using the low-pass prototype filter tables in [177], the third order chebyshev filter with 0.5dB ripple in Section 4.3.1 was found to have g_q values of $g_1 = 1.5963$, $g_2 = 1.0967$ and $g_3 = 1.5963$. Therefore, for the filter of 1nm bandwidth in Section 4.3.1, the corresponding resonator bandwidths were evaluated using Equation (A.1) as $B_1 = 0.798nm$, $B_2 = 0.548nm$ and $B_3 = 0.798nm$.

Similarly, for the fifth order chebyshev filter with 0.5dB ripple and 1nm bandwidth in Section 4.3.2, the g_q values obtained were $g_1 = 1.7058$, $g_2 = 1.2296$, $g_3 = 2.5408$, $g_4 = 1.2296$ and $g_5 = 1.7058$. The corresponding resonator bandwidths

were therefore $B_1 = 0.853nm$, $B_2 = 0.615nm$, $B_3 = 1.27nm$, $B_4 = 0.615nm$ and $B_5 = 0.853nm$.

For the fifth order chebyshev filter with 0.5dB ripple and 0.3nm bandwidth in Section 4.3.4, the g_q values remained unchanged as $g_1 = 1.7058$, $g_2 = 1.2296$, $g_3 = 2.5408$, $g_4 = 1.2296$ and $g_5 = 1.7058$ because only the filter bandwidth had been changed. Based on Equation (A.1), because the filter bandwidth B changed, the individual resonator bandwidths also changed to $B_1 = 0.256nm$, $B_2 = 0.185nm$, $B_3 = 0.381nm$, $B_4 = 0.185nm$ and $B_5 = 0.256nm$.

As discussed in Section 4.3, it is necessary for all the resonators of a filter to be resonant at the same wavelength for a given input excitation. For thin-ridge waveguide resonators this meant that all the waveguides needed to be coupled to the TE slab mode at the same angle of incidence. It was shown in Section 4.2.5 that in order to alter the waveguide Q-factor, while still resonant at the same TE slab mode angle of incidence, it is necessary to adjust both the waveguide width and height. This approach was shown to be successful because it maintains a constant value for the waveguide TM mode index and therefore a constant coupling angle to the TE slab mode while the resonator bandwidth can be varied. By working backwards, the known resonator bandwidth values could be used to determine the required thin-ridge waveguide dimensions of height and width that correspond to that specific Q-factor or bandwidth. To do this, an algorithm was written to search and find the waveguide dimensions that yield a given Q-factor or bandwdith for a fixed waveguide TM mode effective index.

Figure A.1 shows a plot of the waveguide TM mode Q-factor as a function of the dimensions of height and width that was presented in Section 4.2.5. The plot of Figure A.1 shows that there is a wide range of waveguide Q-factors and therefore waveguide bandwidths that can be obtained with small changes in the waveguide dimensions.

The green contour line on Figure A.1 shows the constant TM mode effective index line $TM_{Neff} = 1.8$, which contains a wide range of waveguide dimensions of varying Q-factor and bandwidth. Therefore, waveguides having width and height dimensions on this constant TM index line would not only have a range of bandwidths but would also be resonant at the same TE slab mode angle of incidence. From Equation 4.1, the resonant coupling angle was evaluated as

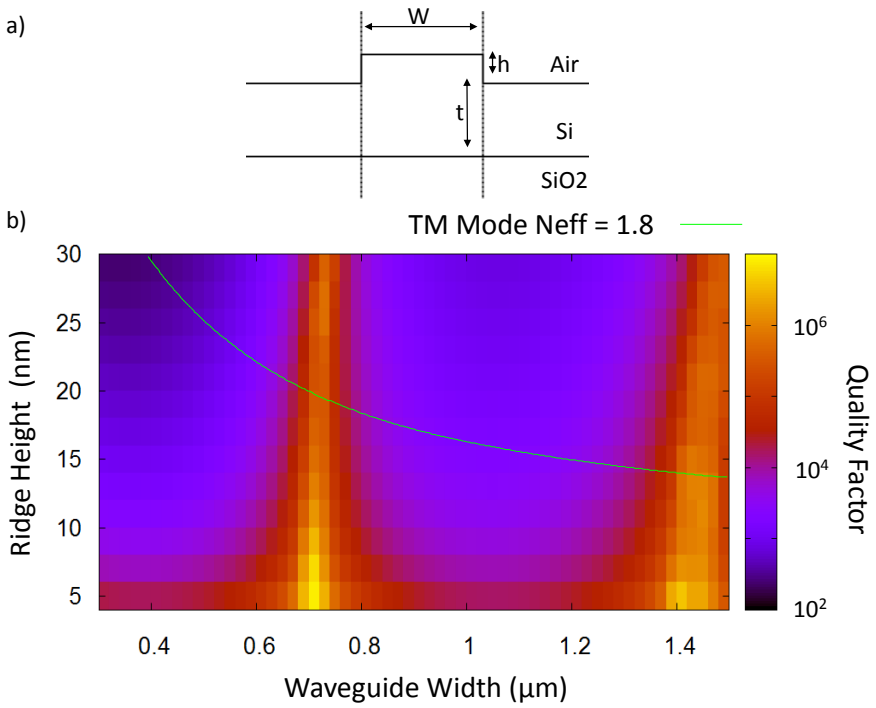

Figure A.1: (a) Thin ridge waveguide resonator of width w, etch depth h and a waveguide slab thickness t of 200nm. (b) 2D plot of the waveguide Q-factor as a function of the waveguide dimensions of width and height. The green contour line shows the waveguide dimensions corresponding to a constant TM mode effective index.

49.29° for $TM_{Neff} = 1.8$. An algorithm was written to automatically search this constant TM_{Neff} line for any of the required resonator bandwidths (or Q-factor) to be used in the filters.

The logic used for the algorithm was based on the bisection method, which is essentially a root-finding method. The method is described as follows. The first step in the algorithm was to select a starting waveguide width W_1 from the x-axis of Figure A.1. Then two ridge heights (h_1 and h_2) were selected which reside on either side of the $TM_{Neff} = 1.8$ contour line. For these two waveguides of similar width W_1 but different heights h_1 and h_2, the magnitude of the reflection coefficient was evaluated for each waveguide when an infinitely wide TE beam was launched towards the waveguide at the angle of 49.29°. The reflection coefficient

was evaluated using the eigen mode expansion method described in Section 4.2.2. Because the chosen waveguide dimensions would not necessarily have a TM mode effective index of $TM_{Neff} = 1.8$, the evaluated reflection coefficient should be less than 100%. This is because only for the waveguide height where the TM mode effective index is equal to $TM_{Neff} = 1.8$ would the the reflection coefficient of a TE slab mode launched at 49.29° equal 100%.

From these two starting points of W_1,h_1 and W_1,h_2, the gradient of the reflection coefficient magnitude was evaluated. This was done by changing the waveguide height h by a very small offset. For example from W_1,h_1 to W_1,h_1', where the difference between h_1 and h_1' is an order of magnitude less than h_1. The reflection coefficient was then evaluated at this second point W_1,h_1'. From the original point W_1,h_1 and the slightly offset point W_1,h_1', the reflection coefficient gradient can be evaluated by taking the difference between the two reflection coefficients. It was either a a positive or negative value depending on which side of the contour line the two points resided. Since both the points W_1,h_1 and W_1,h_2 were chosen to lie on either side of the $TM_{Neff} = 1.8$ contour line, the reflection coefficient gradients at these points were opposite to each other; this means that one was negative and the other positive.

At this stage, the bisection method was used to find the midpoint between W_1,h_1 and W_1,h_2. This was done by dividing the W_1,h_1 and W_1,h_2 interval into two equal sub-intervals at a specific mid-point W_1,h_3. The reflection coefficient and gradient was then evaluated at the mid-point W_1,h_3. From this result, one of the two sub-intervals was selected as the new interval to be bisected again. The interval selected, either W_1,h_1 to W_1,h_3 or W_1,h_2 to W_1,h_3, was determined based on which one of the two points W_1,h_1 and W_1,h_2 had an opposite gradient to W_1,h_3. Provided the two points defining the interval had opposite gradients, the target waveguide height h_x where $TM_{Neff} = 1.8$ and the reflection coefficient is 100% would be expected to lie within this new interval.

This process of bisection was repeated several times until the maximum reflection coefficient point was obtained with a high level of accuracy. This point represented the waveguide dimensions W_1,h_x where TM_{Neff} is approximately equal to 1.8 and the reflection coefficient was close to 100%.

After having obtained the waveguide dimensions W_1,h_x, the next step was to

determine its resonance bandwidth. This evaluated bandwidth could be used to gauge the approximate range from the target bandwidth of the resonator being sought. To evaluate the bandwidth of the resonator W_1,h_x, the assumption was taken that the resonator's reflection coefficient response was a Lorentzian function as was investigated in Section 4.2.3. The Lorentzian function used was shown in Equation 4.4. The reflection coefficient at two different wavelengths points was evaluated, which was then used to simultaneously evaluate the bandwidth of the Lorentzian function which represents the resonators bandwidth.

Now that the resonator bandwidth had been obtained at W_1,h_x where $TM_{Neff} = 1.8$, this process was repeated for a new waveguide of width W_2. Once the bandwidth at W_2 had been evaluated using the same aforementioned method, then it could be determined whether the target bandwidth of the resonator g_q resided between W_1 and W_2. If not, a different width was chosen so that the target bandwidth would reside between W_1 and W_2. At this stage one would now have the bandwidths at two points on the $TM_{Neff} = 1.8$ line and the desired target bandwidth of the resonator would lie in between these two positions. The next step was to again use the bisection method to subdivide this interval between W_1 and W_2 and find the resonator bandwidth at the midpoint W_3. After this, one could determine in which sub-interval the target bandwidth resides, either between W_1 and W_2 or between W_2 and W_3. This way, the bisection algorithm was used to converge on the target bandwidth within a few repetitions with a fairly high level of accuracy.

This was how the waveguide resonator dimensions were obtained having the specific bandwidths needed for the third and fifth order chebyshev filters synthesized in Chapter 4.

A.2 Evaluating resonator separation

In the synthesis of coupled resonator filters the separation between the resonators has to be equal to an odd multiple of a quarter wavelength across the entire frequency range of the filter [173].

This can be expressed as

$$S_c = \frac{\pi}{4}(2m+1) \;\; radians \tag{A.2}$$

where m is a positive integer.

In actual filter synthesis, this separation needs to be kept as close as possible to an odd multiple of a quarter of the resonance wavelength λ_0 over the entire filter bandwidth. This minimizes phase error due to the wavelength dependent nature of the phase delay for a specific separation distance. Therefore the common practice is to minimize the separation distance to minimize this phase error. In the thin-ridge waveguide filters of Chapter 4, the minimum acceptable distance between the resonators was found to be around 5μm in order to minimize evanescent coupling between the TM modes of the waveguide resonators [13].

The evaluated separation S_c between the thin-ridge waveguide resonators specifies the center to center separation between two adjacent resonators. The center to center separation between resonators needs to be an odd multiple of a quarter wavelength at resonance. Therefore, the wall to wall separation which is smaller than the center to center separation between two adjacent waveguides needs to be evaluated to be around 5μm to minimize evanescent coupling.

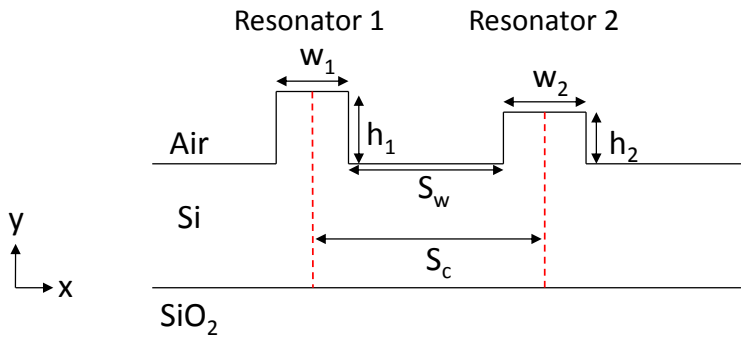

Figure A.2: Schematic of two cascaded waveguide resonators in a thin-ridge waveguide filter topology highlighting the separation distance between the waveguides.

As shown in Figure A.2 the wall to wall separation between adjacent waveguides S_w is therefore less than the center to center separation by half the waveguide width of both adjacent waveguides. However, the TE phase velocity in the core region of the waveguides is different from the TE phase velocity in the slab. Hence, the phase contributions of the TE propagation within the core and the slab regions need to be accounted for. Once this was done the wall to wall phase separation was evaluated and then converted to a physical slab waveguide separation. This is expressed in the equation below.

$$S_c = (k_{xTE1}\frac{w_1}{2}) + (k_{xTE2}\frac{w_2}{2}) + (k_{xTEslab}S_w) \quad radians \tag{A.3}$$

where k_{xTE1} is the x-axis wave-number of the TE slab mode in waveguide 1. k_{xTE2} is the x-axis wave-number of the TE slab mode in waveguide 2. $k_{xTEslab}$ is the x-axis wave-number of the TE slab mode in the slab region between the waveguides. From Equation (A.3) the wall to wall separation between adjacent waveguides S_w was evaluated. This separation was adjusted by varying S_c through the parameter m in equation A.2 so that S_w would be about 5μm wide to minimize evanescent coupling between the resonators.

Appendix B

Polarization converter manuscript

This appendix shows the manuscript for some of the research work in this thesis that is in waiting for submission. This work is specifically related to the polarization converter research that was the subject of Chapter 3.

A TE-TM Beam Polarization Converter for Silicon-on-Insulator Slab Waveguides

Kiplimo Yego, Thach G. Nguyen, and Arnan Mitchell

***Abstract*— We propose and numerically validate a new concept for conversion between TE to TM polarized beams using an array of thin shallow ridges on a SOI slab. Uniform and apodized arrays are analyzed and it is found that a linearly increasing array can effectively convert between collimated TE and TM beams. A small residual TE field was observed after conversion. It is expected that suppression of this residual field could be achieved with more sophisticated apodization.**

***Index Terms*—silicon-on-Insulator (SOI) waveguides, apodized grating couplers, optical polarization conversion, lateral leakage.**

I. Introduction

Thin shallow ridge silicon-on-insulator (SOI) waveguides support strongly evanescent transverse magnetic (TM) polarized modes. These can be desirable for a number of sensing and hybrid photonic applications. However, these TM modes exhibit strong lateral leakage loss unless the waveguide widths are at one of the so-called 'magic' widths [1]. The lateral leakage is due to mode coupling between the guided TM mode and laterally radiating TE slab modes at the ridge boundaries [2]. It should be noted that lateral leakage radiation is not random radiation but is rather highly coherent. It has been proposed previously that this lateral leakage behavior could be utilized to achieve new photonic devices [3-5].

Practical integrated optic circuits require external interfaces. Grating couplers are gaining popularity; however, efficient TM grating couplers are generally complex and require deep etching [6]. Further, waveguide tapers are normally required to interface the large grating couplers to compact waveguides, but simple linear tapers exhibit strong lateral leakage [5].

The lateral leakage loss due to mode coupling at the waveguide boundaries can be avoided if TM-polarized light is transmitted in the form of an unguided collimated beam and is only coupled into 'magic' TM waveguides when necessary. If the collimated TM beam can be generated from a collimated TE beam, then it is possible to efficiently couple light in and out using a TE grating coupler together with lens structure [7].

In this letter, we propose and numerically test thin shallow ridge SOI structures that exploit lateral leakage to convert between TE and TM collimated beams within the silicon slab and show that a linearly apodized grating can be effective.

The authors are with the Centre for Ultrahigh Bandwidth Devices for Optical Systems (CUDOS), School of Electrical and Computer Engineering, RMIT University, Melbourne, Australia. This work was supported in part by the Australian Research Council (ARC) under grant DP1096153 and in part by the ARC Centre of Excellence.

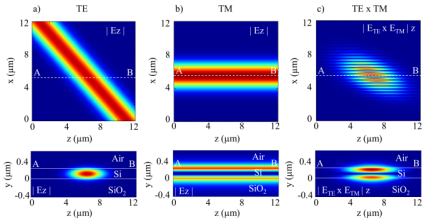

Fig. 1. (a) The E_z field component of a TE gaussian beam propagating at an angle. (b) The E_z field component of a TM gaussian beam propagating in the z-axis direction in a SOI slab waveguide. (c) The E_z field component of the overlap between the TM and TE gaussian beams.

II. Principle of Operation

If the interference pattern formed between an image/object beam and a reference beam is preserved in some persistent medium, then illumination of this preserved interference pattern with the reference beam alone has the effect of regenerating the image/object beam including both its amplitude and phase in all three dimensions. This process is called holography. Holographic principles have been used for the design of planar integrated optic structures previously [8]. It is proposed that these principles may be used to design a TE to TM converter based on lateral leakage [1-2].

Consider two Gaussian beams confined to a silicon slab as depicted in Fig. 1. One beam is confined vertically in the fundamental TE mode of the silicon slab, but is an unbounded Gaussian beam laterally, as shown in the lower and upper images of Fig. 1(a) respectively. The other beam is confined vertically in the fundamental TM mode of the slab but is an unbounded Gaussian beam laterally, as shown in the lower and upper images of Fig. 1(b) respectively. If the propagation axes of the two beams are oriented such that they remain in phase along the axis of the TM beam (the z-axis), the z-directed E field components of each beam will have a non-zero overlap where the two beams intersect and the product of the two fields should appear as shown in Fig. 1(c). Vertically, the pattern is strongest at the top and bottom silicon surfaces with a null near the center of the silicon slab. Laterally, the pattern has constant amplitude along the z-axis (due to phase matching) but exhibits sinusoidal fringes along the x-axis and has the Gaussian envelope of the two original beams.

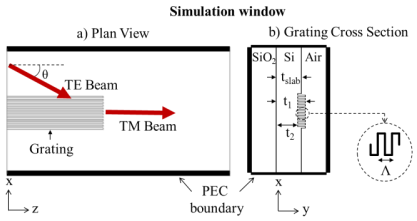

Fig. 2. (a) Plan view and (b) cross section view of the 3D simulation window. Here t_1=220nm, t_2=205nm and t_{slab}=212.5nm. The perturbation structure was designed to resemble the interference pattern of Fig. 1(c). The TE beam within the silicon slab had a Gaussian form with a width of 32μm and was launched towards the grating at an angle θ.

Drawing on holographic concepts, we predict that if a perturbation were implemented resembling Fig. 1(c), then illumination of this perturbation with a TE Gaussian beam with the same properties and angle of incidence as shown in Fig. 1(a) should generate a TM beam similar to Fig. 1(b).

We wish to test this hypothesis via rigorous numerical simulation, however, numerical simulation of a perturbation with the exact structure of the pattern of Fig. 1(c) would be challenging. Thus, a number of approximations were made to simplify the structure of the perturbation with the result presented in Fig. 2. Firstly, we limited the location of the perturbation to the top silicon surface. We then approximated the sinusoidal interference fringes using two levels as shown in Fig. 2(b). It should be noted that these two levels are equally above and below the thickness of the open Si slab in order to ensure that the average refractive index in the structure and the open slab are equal in order to minimize the effects of reflection and refraction. The envelope of the interference pattern was approximated as a simple rectangular step function as shown in Fig. 2(a).

The structure of Fig. 2 appears to have the form of a grating. However, the grating is not periodic along the direction of propagation of the desired TM beam, but is rather periodic across the beam's width. This is as expected since the TE and TM beams are phase matched along the z-axis, however, the two beams are not phase matched along the x-axis. For efficient coupling to occur, the two beams should be completely phase matched across the entire interaction area and the grating oriented along the x-axis provides this additional phase matching. In order to be phase matched along the z-axis, the angle between the two beams should be

$$\theta = \cos^{-1}\left(N_{TM}/N_{TE}\right) \tag{1}$$

where N_{TE} and N_{TM} are the effective indexes of the TE and TM slab modes respectively. At this angle, phase matching along the x-axis would require a grating of period

$$\Lambda = \frac{\lambda}{\sqrt{N_{TE}^2 - N_{TM}^2}} \tag{2}$$

III. Uniform Grating Coupler

Having predicted that a grating similar to that of Fig. 2 should convert a TE beam into a TM beam, this Section uses rigorous numerical modeling to investigate the actual effect that such a grating will have on an incident TE beam.

Fig. 3(a) illustrates the cross-section of the grating. With N_{TE}=2.8058 and N_{TM}=1.8223 [1], the angle of incidence of the TE beam on the grating was calculated from (1) as θ=49.5°. The grating period was calculated from (2) as Λ=726.5nm with λ=1.55μm. The width was set to 80um to accommodate 32um wide beams and thus the grating had 110 periods.

The electromagnetic response of the grating structure was simulated using an in-house implementation of the fully vectorial eigenmode expansion (EME) method [9]. This simulation method has been previously used to model the TM to TE coupling behavior in thin-ridge silicon waveguide tapers [5]. The simulation window as shown in Fig. 2 was bounded in the x-y plane by perfect electrically conducting (PEC) walls. In EME, the field within a waveguide structure is discretized into a finite set of eigenmodes that exist within the boundaries of the structure. Any field propagating within the waveguide structure can be decomposed into this set of eigenmodes provided a sufficient number of eigenmodes are used. A full-vector mode matching method [2] was used to calculate the eigenmodes of each waveguide segment. To launch the TE beam into the simulation window, a canonical Gaussian TE beam profile rotated at an angle was expanded into the eigenmodes of the input slab waveguide structure.

Fig. 3(b) shows the x-directed component of the electric field, which corresponds to the TE polarization. Before interacting with the grating, the Gaussian TE beam remains unperturbed and well collimated. After entering the grating region the amplitude of this TE beam decays rapidly over the first few ridges and a pair of narrow reflected and transmitted TE beams appear to be generated when the grating terminates.

Fig. 3(c) shows the y-directed component of the electric field, which corresponds to the TM polarization. There is no evidence of the TM beam until the TE beam strikes the grating. However the TM field is excited once the TE beam does interact with the grating. This is clear evidence of the conversion from TE-polarized field to TM-polarized field due to the grating. This TM beam is strong at the point where the TE beam strikes the grating, but rapidly decays within the grating region. The generated TM beam within the grating region continues to propagate once the grating terminates, but is very narrow and has an asymmetric profile causing it to diverge strongly when propagating over a long distance as shown in the inset of Fig. 3(c).

The narrow aperture of the TM beam is a direct result of the strong, uniform grating used. When the TE beam is incident onto the grating, there is a sudden coupling of the TE field to the TM field. The amplitude of the TM field continues to increase due to continuous coupling from TE to TM. However, after a few periods, the TE field amplitude has reduced dramatically causing the drop of TM field amplitude.

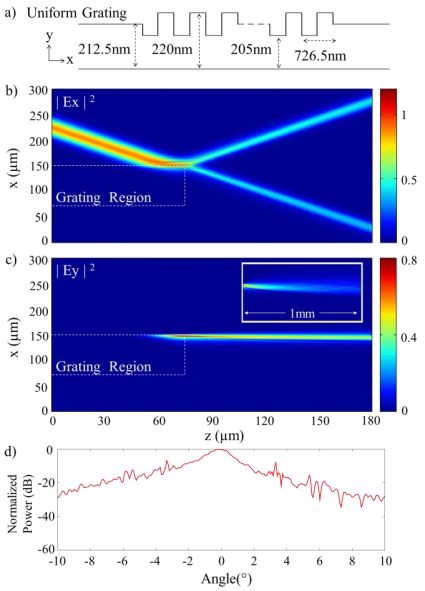

Fig. 3. (a) Uniform grating profile; (b) x-directed E field, corresponding to TE beam launched at 49.5°; (c) y-directed E field, corresponding to TM beam, Inset: TM beam propagating 1mm; (d) Angular spectrum of TM beam.

The apparent reflection of the TE beam in Fig. 3(b) is surprising as care was taken to keep the effective index of the grating equal to the slab. To test whether this reflection could be conventional Fresnel reflection, an equivalent multilayer model was implemented. This showed that conventional Fresnel reflection from an infinitely long, equivalent index contrast grating would be negligible. Alternately, the observed reflected TE beam could be due to cascaded conversion of the TE beam to a TM beam and then back again. The fact that the reflected TE beam is narrower than the incident TE beam and is more like the generated TM beam supports this hypothesis.

The collimation of the generated TM beam can be analyzed by examining its angular spectral properties. The total TM field propagating through the uniform slab region can be expressed as a weighted superposition of the eigenmodes of the slab. The effective index of each eigenmode can be interpreted as propagation angle [5]. The eigenmode with effective index equal to the effective index of the silicon slab corresponds to a zero propagation angle. Fig. 3(d) shows the normalized TM field amplitude as a function of the angle of propagation exhibiting a broad peak centered at 0°. Like the field profile itself, the spectrum is also slightly asymmetric. The 3dB beam width was measured to be $\Delta\theta = 1.3°$. Some noisy spectral components are also observed at the wider angles and these are only 6dB below the central peak.

The results of Fig. 3 show that, in principle, the grating of Fig. 2 could convert a Gaussian TE beam into TM radiation, however, the TM beam produced was narrow and asymmetric leading to high divergence when propagating over a long distance. These qualities of the generated beam were attributed to the rapid conversion of the TE beam into TM within the space of only a few periods of the grating. It is proposed that if the conversion can be achieved more gradually across the grating then the TM beam should be generated over a broader aperture and should hence have lower divergence.

IV. Apodized Grating Coupler

In Section III it was shown numerically that a TE beam can be converted into a TM beam using a uniform grating structure, but that the generated beam was highly divergent due to the conversion occurring in a very confined region in the grating. It was proposed that the beam quality could be improved by apodizing the grating strength such that conversion was distributed across all of the periods of the grating creating a broad, canonical aperture for excitation of the TM beam. Such apodization techniques have been used previously on many optical coupling structures including tapers, gratings and dispersion compensators [5,10-11].

It should be possible to vary the coupling strength of the grating by changing the duty cycle. The ideal profile to achieve a collimated beam would be a Gaussian window, however it would not be effective to simply set the grating strength to match a Gaussian since the excitation of the TM beam will be the product of both the grating strength and the amplitude of the TE driving beam which is reducing throughout the conversion process. As shown in [5], taking this effect into account an approximately Gaussian aperture can be achieved using a simple linear increase in coupling strength. It is proposed that simply linearly increasing the grating strength in the current case will also produce an effective Gaussian apodization for the TM beam.

To test whether a linear apodization would improve the collimation of the generated TM beam, the uniform grating of Fig. 3(a) was replaced with a grating with linearly increasing coupling strength as illustrated in Fig. 4(a). The grating period and width of the grating were kept as 726.5nm and 80um, respectively. The duty cycle of the each grating period was linearly increased from zero to a maximum value, chosen so that at the end of the grating structure, all power in the TE beam has converted to TM beam. It was found that this condition can be met if the duty cycle of the last grating period is larger than 30%, and thus this was the duty cycle used on the last grating period. Using the method of Section III, we simulated the effect of illuminating the apodized grating when a TE beam is incident upon it at an angle of 49.5°.

Fig. 4(b) shows the x-directed component of the electric field. Unlike Fig. 3(b), the amplitude of the TE beam does not drop abruptly when the TE beam strikes the grating. Instead, it slowly decays as it propagates through the grating. At the end of the grating, very little power is left in the TE beam.

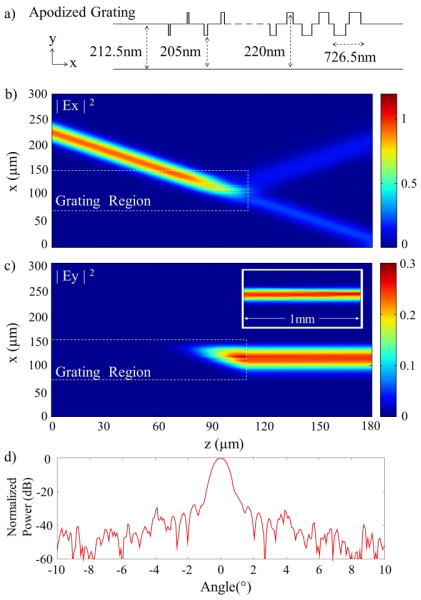

Fig. 4. (a) Apodized grating profile; (b) x-directed E field, corresponding to TE beam launched at 49.5°; (c) y-directed E field, corresponding to TM beam, Inset: TM beam propagating 1mm; (d) Angular spectrum of TM beam.

Fig. 4(c) shows the y-directed component of the electric field, which corresponds to the generated TM field. Similar to the case of the uniform grating of Fig. 3(c), inside the grating structure, most of the power from the TE beam is converted into a TM beam. However, unlike Fig. 3(c), the TM field slowly increases in amplitude to a peak at approximately the middle of the grating then slowly decreases. At the aperture of the grating, the generated TM beam using the linear grating is much broader than that generated from the uniform grating. The generated beam also appears to be relatively symmetric and approximately Gaussian. The resulting TM beam can propagate over a long distance in a silicon slab with low divergence as shown in the inset of Fig. 4(c).

The angular spectrum of the TM beam was evaluated using the same method as described in section III. Fig. 4(d) shows the y-directed (TM) electric field amplitude as a function of the angle of propagation. Compared to Fig. 3(d), a far narrower angular spectrum of the TM beam is launched from the apodized grating. The TM beam mainly propagates along the z-axis. The sidelobes are 27dB below the main lobe. The 3dB beam width was found to be $\Delta\theta = 0.74°$. Both the sidelobe level and the beam width are much lower than those of the TM beam generated from the uniform grating as shown in Fig. 3(d). This significantly improved TM beam proves the effectiveness of this simple apodization strategy.

Fig. 4(b) shows that while most of the input TE beam has been converted, there is still some small residual TE polarized light appearing as both transmitted and reflected TE beams. These beams are far broader and weaker than those observed in Fig. 3(a) which could be attributed to the improved apodization. The beams appear to originate from the center of the grating, where the TM beam is strongest supporting the hypothesis that this is due to cascaded conversion of the TM beam back to TE. It may be possible to suppress this back conversion if the full form of the holographic apodization window of Fig. 1(c) were implemented. Testing this hypothesis would be difficult with eigenmode expansion and may be better suited to finite difference time domain. This simulation is proposed as future work.

V. Conclusion

We have proposed and numerically verified that a periodic array of thin shallow ridges can convert optical beams within a SOI slab between TE and TM polarizations. In order to achieve a highly collimated output TM beam, it is necessary to apodize the array of ridges. A linear increase in coupling across the grating proves quite effective. We have observed unusual reflection of the input TE beam that we attribute to cascaded conversion of TE to TM and then back again. Further investigation of this effect is proposed as future work.

References

[1] M.A. Webster, R.M. Pafchek, A. Mitchell, and T.L. Koch, "Width dependence of inherent TM-mode lateral leakage loss in silicon-on-insulator ridge waveguides," *IEEE Photon. Technol. Lett.*, vol. 19, no. 6, pp. 429–431, Mar. 2007.

[2] T.G. Nguyen, R.S. Tummidi, T.L. Koch, and A. Mitchell, "Rigorous modeling of lateral leakage loss in SOI thin-ridge waveguides and couplers," *IEEE Photon. Technol. Lett.*, vol. 21, no. 7, pp. 486–488, Apr. 2009.

[3] D. Dai, Z. Wang, N. Julian, and J.E. Bowers, "Compact broadband polarizer based on shallowly-etched silicon-on-insulator ridge optical waveguides," *Opt. Express*, vol. 18, no. 26, pp. 27404–27415, Dec. 2010.

[4] N. Dalvand, T.G. Nguyen, R.S. Tummidi, T.L. Koch, and A. Mitchell, "Thin-ridge Silicon-on-Insulator waveguides with directional control of lateral leakage radiation," *Opt. Express*, vol. 19, no. 6, pp. 5635–5643, Mar. 2011.

[5] N. Dalvand, T.G. Nguyen, T.L. Koch, and A. Mitchell, "Thin shallow-ridge silicon-on-insulator waveguide transitions and tapers," *IEEE Photon. Technol. Lett.*, vol. 25, no. 2, pp. 163–166, Jan. 2013.

[6] R. Halir, P. Cheben, S. Janz, D.-X. Xu, I. Molina-Fernandez, and J.G. Wanguemert-Perez, "Waveguide grating coupler with subwavelength microstructures," *Opt. Lett.*, vol. 34, no. 9, pp. 1408–1410, May 2009.

[7] R. Guanghui, T.G. Nguyen and A. Mitchell, "On-chip collimated planar 'free-space' gaussian beams utilising optical lenses on a silicon on insulator chip," in *CLEO/Europe: International Quantum Electronics Conference 2013*, paper CK-10.4, May 12-16, 2013.

[8] M. Verbist, D. Van Thourhout, and W. Bogaerts, "Weak gratings in silicon-on-insulator for spectral filters based on volume holography," *Opt. Lett.* vol. 38, no. 3, pp. 386-388, Jan. 2013.

[9] P. Bienstman, and R. Baets, "Optical modelling of photonic crystals and VCSELs using eigenmode expansion and perfectly matched layers," *Opt. Quant. Electron.*, vol. 33, no. 4-5, pp. 327–341, Apr. 2001.

[10] D. Taillaert, P. Bienstman, and R. Baets, "Compact efficient broadband grating coupler for silicon-on-insulator waveguides," *Opt. Lett.*, vol. 29, no. 23, pp. 2749–2751, Dec. 2004.

[11] I. Giuntoni, D. Stolarek, J. Bruns, L. Zimmermann, B. Tillack, and K. Petermann, "Integrated dispersion compensator based on apodized SOI Bragg gratings," *IEEE Photon. Technol. Lett.*, vol. 25, no. 14, pp. 1313–1316, Jul. 2013.

References

[1] B. Koch, A. Alduino, Ling Liao, R. Jones, M. Morse, B. Kim, Wei-Zen Lo, J. Basak, Hai-Feng Liu, Haisheng Rong, M. Sysak, C. Krause, R. Saba, D. Lazar, L. Horwitz, R. Bar, S. Litski, Ansheng Liu, K. Sullivan, O. Dosunmu, N. Na, Tao Yin, F. Haubensack, I wei Hsieh, J. Heck, R. Beatty, J. Bovington, and M. Paniccia. A 4x12.5 gb/s cwdm si photonics link using integrated hybrid silicon lasers. In *Lasers and Electro-Optics (CLEO), 2011 Conference on*, pages 1–2, May 2011. 1, 54

[2] W. Bogaerts, R. Baets, P. Dumon, V. Wiaux, S. Beckx, D. Taillaert, B. Luyssaert, J. Van Campenhout, P. Bienstman, and D. Van Thourhout. Nanophotonic waveguides in silicon-on-insulator fabricated with cmos technology. *Lightwave Technology, Journal of*, 23(1):401–412, Jan 2005. 1, 53

[3] A. Densmore, D.-X. Xu, P. Waldron, S. Janz, P. Cheben, J. Lapointe, A. Delge, B. Lamontagne, J.H. Schmid, and E. Post. A silicon-on-insulator photonic wire based evanescent field sensor. *IEEE Photonics Technology Letters*, 18(23):2520–2522, 2006. 1, 18, 19, 20

[4] M. Jamal Deen and P. K. Basu. *Silicon Photonics Fundamentals and Devices*. John Wiley and Sons Ltd, The Atrium, Southern Gate, Chichester, West Sussex, PO19 8SQ, United Kingdom, 2012. ISBN 978-0-470-51750-5. 2

[5] P. Sanchis, J. Blasco, A. Martnez, and J. Mart. Design of silicon-based slot waveguide configurations for optimum nonlinear performance. *Journal of Lightwave Technology*, 25(5):1298–1305, 2007. 2

[6] T. Claes, J.G. Molera, K. De Vos, E. Schacht, R. Baets, and P. Bienstman. Label-free biosensing with a slot-waveguide-based ring resonator in silicon on insulator. *IEEE Photonics Journal*, 1(3):197–204, 2009. 2, 22, 23

[7] Y. Takahashi, T. Asano, D. Yamashita, and S. Noda. Ultra-compact 32-channel drop filter with 100 ghz spacing. *Optics Express*, 22(4):4692–4698, 2014. 2

[8] R.M. De La Rue and C. Seassal. Photonic crystal devices: Some basics and selected topics. *Laser and Photonics Reviews*, 6(4):564–597, 2012. 2

[9] F. Morichetti, C. Ferrari, A. Canciamilla, and A. Melloni. The first decade of coupled resonator optical waveguides: Bringing slow light to applications. *Laser and Photonics Reviews*, 6(1):74–96, 2012. 2

[10] M. A. Webster, R.M. Pafchek, A. Mitchell, and T. L. Koch. Width dependence of inherent tm-mode lateral leakage loss in silicon-on-insulator ridge waveguides. *IEEE Photonics Technology Letters*, 19(6):429–431, 2007. 2, 3, 4, 5, 7, 8, 10, 29, 69, 71, 123

[11] X. Guan, H. Wu, Y. Shi, and D. Dai. Extremely small polarization beam splitter based on a multimode interference coupler with a silicon hybrid plasmonic waveguide. *Optics Letters*, 39(2):259–262, 2014. 2

[12] R. Pafchek, R. Tummidi, J. Li, M.A. Webster, E. Chen, and T.L. Koch. Low-loss silicon-on-insulator shallow-ridge te and tm waveguides formed using thermal oxidation. *Applied Optics*, 48(5):958–963, 2009. 3, 24

[13] N. Dalvand, T. G. Nguyen, R. S. Tummidi, T. L. Koch, and A. Mitchell. Thin-ridge silicon-on-insulator waveguides with directional control of lateral leakage radiation. *Optics Express*, 19(6):5635–5643, 2011. 3, 49, 65, 133, 164

[14] N. Dalvand, T. G. Nguyen, T. L. Koch, and A. Mitchell. Thin shallow-ridge silicon-on-insulator waveguide transitions and tapers. *IEEE Photonics Technology Letters*, 25(2):163–166, 2013. 3, 30, 33, 34, 37, 48, 64, 68, 74, 75, 106, 121, 124

[15] T. G. Nguyen, R. S. Tummidi, T. L. Koch, and A. Mitchell. Rigorous modeling of lateral leakage loss in soi thin-ridge waveguides and couplers. *IEEE Photonics Technology Letters*, 21(7):486–488, 2009. 8, 9, 27, 106, 110, 121

[16] K. Yego, T. Nguyen, and A. Mitchell. Evanescent wave sensors utilizing laterally radiating thin-ridge silicon-on-insulator waveguide tapers. In *2014 OptoElectronics and Communication Conference, OECC 2014 and Australian Conference on Optical Fibre Technology, ACOFT 2014*, pages 577–579, 2014. 15

[17] Kiplimo Yego, Thach G. Nguyen, and Arnan Mitchell. Utilization of coherent lateral leakage radiation from thin-ridge soi waveguides for integrated optical evanescent biosensing. In *JSAP-OSA Joint Symposia 2012, The 73rd Japan Society of Applied Physics Autumn Meeting 2012*, pages 11p–G2–13, 2012. 15

[18] X. Fan, I.M. White, S.I. Shopova, H. Zhu, J.D. Suter, and Y. Sun. Sensitive optical biosensors for unlabeled targets: A review. *Analytica Chimica Acta*, 620(1-2):8–26, 2008. 17, 18, 93

[19] N.A. Yebo, P. Lommens, Z. Hens, and R. Baets. An integrated optic ethanol vapor sensor based on a silicon-on-insulator microring resonator coated with a porous zno film. *Optics Express*, 18(11):11859–11866, 2010. 17, 18

[20] Zhixuan Xia, Ali Asghar Eftekhar, Mohammad Soltani, Babak Momeni, Qing Li, Maysamreza Chamanzar, Siva Yegnanarayanan, and Ali Adibi. High resolution on-chip spectroscopy based on miniaturized microdonut resonators. *OPTICS EXPRESS*, 19(13):12356–12364, JUN 20 2011. 17

[21] Xiao Ma, Mingyu Li, and Jian-Jun He. CMOS-Compatible Integrated Spectrometer Based on Echelle Diffraction Grating and MSM Photodetector Array. *IEEE PHOTONICS JOURNAL*, 5(2), APR 2013. 17

[22] K. De Vos, I. Bartolozzi, E. Schacht, P. Bienstman, and R. Baets. Silicon-on-insulator microring resonator for sensitive and label-free biosensing. *Optics Express*, 15(12):7610–7615, 2007. 18, 20, 93

[23] A. Densmore, D.-X. Xu, S. Janz, P. Waldron, T. Mischki, G. Lopinski, A. Delge, J. Lapointe, P. Cheben, B. Lamontagne, and J.H. Schmid. Spiral-path high-sensitivity silicon photonic wire molecular sensor with temperature-independent response. *Optics Letters*, 33(6):596–598, 2008. 20

[24] L.J. Kauppinen, H.J.W.M. Hoekstra, and R.M. de Ridder. A compact refractometric sensor based on grated silicon photonic wires. *Sensors and Actuators, B: Chemical*, 139(1):194–198, 2009. 20

[25] D.-X. Xu, A. Densmore, A. Delge, P. Waldron, R. McKinnon, S. Janz, J. Lapointe, G. Lopinski, T. Mischki, E. Post, P. Cheben, and J.H. Schmid. Folded cavity soi microring sensors for high sensitivity and real time measurement of biomolecular binding. *Optics Express*, 16(19):15137–15148, 2008. 20, 21

[26] K. De Vos, J. Girones, T. Claes, Y. De Koninck, S. Popelka, E. Schacht, R. Baets, and P. Bienstman. Multiplexed antibody detection with an array of silicon-on-insulator microring resonators. *IEEE Photonics Journal*, 1(4): 225–235, 2009. 21

[27] A.L. Washburn, L.C. Gunn, and R.C. Bailey. Label-free quantitation of a cancer biomarker in complex media using silicon photonic microring resonators. *Analytical Chemistry*, 81(22):9499–9506, 2009. 21, 92

[28] D.-X. Xu, M. Vachon, A. Densmore, R. Ma, A. Delge, S. Janz, J. Lapointe, Y. Li, G. Lopinski, D. Zhang, Q.Y. Liu, P. Cheben, and J.H. Schmid. Label-free biosensor array based on silicon-on-insulator ring resonators addressed using a wdm approach. *Optics Letters*, 35(16):2771–2773, 2010. 20, 21, 93

[29] S. Werquin, S. Verstuyft, and P. Bienstman. Integrated interferometric approach to solve microring resonance splitting in biosensor applications. *Optics Express*, 21(14):16955–16963, 2013. 21

[30] R.W. Boyd and J.E. Heebner. Sensitive disk resonator photonic biosensor. *Applied Optics*, 40(31):5742–5747, 2001. 22

[31] S.M. Grist, S.A. Schmidt, J. Flueckiger, V. Donzella, W. Shi, S.T. Fard, J.T. Kirk, D.M. Ratner, K.C. Cheung, and L. Chrostowski. Silicon photonic micro-disk resonators for labelfree biosensing. *Optics Express*, 21(7):7994–8006, 2013. 22

[32] F. Dell'Olio and V.M.N. Passaro. Optical sensing by optimized silicon slot waveguides. *Optics Express*, 15(8):4977–4993, 2007. 22

[33] M.R. Lee and P.M. Fauchet. Nanoscale microcavity sensor for single particle detection. *Optics Letters*, 32(22):3284–3286, 2007. 23

[34] J. Garca-Ruprez, V. Toccafondo, M.J. Banuls, J.G. Castell, A. Griol, S. Peransi-Llopis, and A. Maquieira. Label-free antibody detection using band edge fringes in soi planar photonic crystal waveguides in the slow-light regime. *Optics Express*, 18(23):24276–24286, 2010. 23

[35] HemantSankar Dutta and Suchandan Pal. Design of a highly sensitive photonic crystal waveguide platform for refractive index based biosensing. *Optical and Quantum Electronics*, 45(9):907–917, 2013. 23, 24

[36] Kangbaek Kim, R.M. Pafchek, and T.L. Koch. Athermal silicon waveguides for aqueous evanescent biosensor applications. In *Photonics Conference (PHO), 2011 IEEE*, pages 419–420, Oct 2011. 24, 49

[37] Kangbaek Kim, R.M. Pafchek, and T.L. Koch. Label-free biosensors based on athermal silicon-on-insulator waveguides and a harmonic dithering technique. In *Lasers and Electro-Optics (CLEO), 2012 Conference on*, pages 1–2, May 2012. 24

[38] T.G. Nguyen, R.S. Tummidi, T.L. Koch, and A. Mitchell. Lateral leakage of tm-like mode in thin-ridge silicon-on-insulator bent waveguides and ring resonators. *Optics Express*, 18(7):7243–7252, 2010. 25

[39] J. Voros. The density and refractive index of adsorbing protein layers. *Biophysical Journal*, 87(1):553–561, 2004. 27

[40] Naser Dalvand. *Silicon Photonic Devices Utilizing Lateral Leakage Behaviour*. PhD thesis, RMIT University, School of Electrical and Computer Engineering, 2014. 30, 33, 35, 40

[41] Bahaa E. A. Saleh and Malvin Carl Teich. *Fundamentals of Photonics*. John Wiley and Sons, Inc., Hoboken, New Jersey, 2007. ISBN 978-0-471-35832-9. 32, 34, 39, 66, 92, 114

[42] R. Scarmozzino, A. Gopinath, R. Pregla, and S. Helfert. Numerical techniques for modeling guided-wave photonic devices. *IEEE Journal on Selected Topics in Quantum Electronics*, 6(1):150–162, 2000. 33, 68

[43] G. Ren, T. Nguyen, and A. Mitchell. On-chip collimated planar 'free space' gaussian beams utilising optical lenses on a silicon on insulator chip. 2013. 34, 65

[44] M. Koshiba, K. Kakihara, and K. Saitoh. Reduced lateral leakage losses of tm-like modes in silicon-on-insulator ridge waveguides. *Optics Letters*, 33 (17):2008–2010, 2008. 35, 49

[45] C.R. Doerr, L.L. Buhl, Y. Baeyens, R. Aroca, S. Chandrasekhar, X. Liu, L. Chen, and Y.-K. Chen. Packaged monolithic silicon 112-gb/s coherent receiver. *Photonics Technology Letters, IEEE*, 23(12):762–764, June 2011. 52, 53

[46] X. Zhou, L.E. Nelson, P. Magill, R. Isaac, B. Zhu, D.W. Peckham, P.I. Borel, and K. Carlson. Pdm-nyquist-32qam for 450-gb/s per-channel wdm transmission on the 50 ghz itu-t grid. *Journal of Lightwave Technology*, 30 (4):553–559, 2012. 52

[47] D.C. Hutchings, B.M. Holmes, C. Zhang, P. Dulal, A.D. Block, S.-Y. Sung, N.C.A. Seaton, and B.J.H. Stadler. Quasi-phase-matched faraday rotation in semiconductor waveguides with a magnetooptic cladding for monolithically integrated optical isolators. *IEEE Photonics Journal*, 5(6), 2013. 52, 54

[48] Y.-L. Lo and T.-C. Yu. A polarimetric glucose sensor using a liquid-crystal polarization modulator driven by a sinusoidal signal. *Optics Communications*, 259(1):40–48, 2006. 52, 54

[49] Jesús Álvarez, Paolo Bettotti, Isaac Suárez, Neeraj Kumar, Daniel Hill, Vladimir Chirvony, Lorenzo Pavesi, and Juan Martínez-Pastor. Birefringent porous silicon membranes for optical sensing. *Optics Express*, 19(27):26106–26116, Dec 2011. 52

[50] T.K. Noh and Y.W. Lee. Temperature-insensitive polarimetric fiber strain sensor with short polarization-maintaining photonic crystal fiber. *Applied Physics Express*, 5(11), 2012. 52, 54

[51] Q. Rong, X. Qiao, H. Yang, D. Su, F. Liu, R. Wang, Y. Du, D. Feng, M. Hu, and Z. Feng. Orthogonal polarization coupling for transverse strain measurement using a polarimetric mirror. *IEEE Photonics Technology Letters*, 26(7):729–732, 2014. 52

[52] J.J. Peltzer, P.D. Flammer, T.E. Furtak, R.T. Collins, and R.E. Hollingsworth. Ultra-high extinction ratio micropolarizers using plasmonic lenses. *Optics Express*, 19(19):18072–18079, 2011. 52

[53] I. Mandel, J.N. Gollub, I. Bendoym, and D.T. Crouse. Theory and design of a novel integrated polarimetric sensor utilizing a light sorting metamaterial grating. *IEEE Sensors Journal*, 13(2):618–625, 2013. 52

[54] G.A. Atkinson and E.R. Hancock. Recovery of surface orientation from diffuse polarization. *IEEE Transactions on Image Processing*, 15(6):1653–1664, 2006. 52

[55] J.S. Tyo, D.L. Goldstein, D.B. Chenault, and J.A. Shaw. Review of passive imaging polarimetry for remote sensing applications. *Applied Optics*, 45 (22):5453–5469, 2006. 52

[56] J. Kim, R.K. Komanduri, K.F. Lawler, D. Jason Kekas, and M.J. Escuti. Efficient and monolithic polarization conversion system based on a polarization grating. *Applied Optics*, 51(20):4852–4857, 2012. 52

[57] Shamsolah Salemian and Shahram Mohammadnejad. Design and implementation of polarization filter for quantum states discriminator in optical quantum communication. *Optik - International Journal for Light and Electron Optics*, 122(4):349 – 354, 2011. 52, 53

[58] G. Corrielli, A. Crespi, R. Geremia, R. Ramponi, L. Sansoni, A. Santinelli, P. Mataloni, F. Sciarrino, and R. Osellame. Rotated waveplates in integrated waveguide optics. *Nature Communications*, 5, 2014. 52, 53

[59] Po Dong, Chongjin Xie, and Lawrence L. Buhl. Monolithic polarization diversity coherent receiver based on 120-degree optical hybrids on silicon. *Opt. Express*, 22(2):2119–2125, Jan 2014. 53

[60] S. Feng, T. Lei, H. Chen, H. Cai, X. Luo, and A.W. Poon. Silicon photonics: From a microresonator perspective. *Laser and Photonics Reviews*, 6(2):145–177, 2012. 53, 102, 114

[61] D. Dai and S. He. Analysis of the birefringence of a silicon-on-insulator rib waveguide. *Applied Optics*, 43(5):1156–1161, 2004. 53

[62] W. Bogaerts, D. Taillaert, P. Dumon, D. Van Thourhout, R. Baets, and E. Pluk. A polarization-diversity wavelength duplexer circuit in silicon-on-insulator photonic wires. *Optics Express*, 15(4):1567–1578, 2007. 53, 54

[63] D. Dai, L. Liu, S. Gao, D.-X. Xu, and S. He. Polarization management for silicon photonic integrated circuits. *Laser and Photonics Reviews*, 7(3): 303–328, 2013. 53

[64] S.P. Chan, C.E. Png, S.T. Lim, G.T. Reed, and V.M.N. Passaro. Single-mode and polarization-independent silicon-on-insulator waveguides with small cross section. *Journal of Lightwave Technology*, 23(6):2103–2111, 2005. 53

[65] D. Dai, Y. Shi, and S. He. Characteristic analysis of nanosilicon rectangular waveguides for planar light-wave circuits of high integration. *Applied Optics*, 45(20):4941–4946, 2006. 53

[66] D.-X. Xu, W.N. Ye, S. Janz, A. Delge, P. Cheben, B. Lamontagne, E. Post, and P. Waldron. Stress induced effects for advanced polarization control in silicon photonics components. *Advances in Optical Technologies*, 2008. 53

[67] Qing Fang, Lianxi Jia, Junfeng Song, Andy E. J. Lim, Xiaoguang Tu, Xianshu Luo, Mingbin Yu, and Guoqiang Lo. Demonstration of a vertical pin ge-on-si photo-detector on a wet-etched si recess. *OPTICS EXPRESS*, 21(20):23325–23330, 2013. 54

[68] Jonathan Y. Lee, Lianghong Yin, Govind P. Agrawal, and Philippe M. Fauchet. Ultrafast optical switching based on nonlinear polarization rotation in silicon waveguides. *OPTICS EXPRESS*, 18(11):11514–11523, MAY 24 2010. 54

[69] Miaoli Mou, Hongjun Liu, Nan Huang, Qibing Sun, and Zhaolu Wang. Tunable terahertz Kerr switching based on nonlinear polarization rotation in silicon waveguide. *APPLIED OPTICS*, 53(12):2741–2747, 2014. 54

[70] Y. Yue, L. Zhang, M. Song, R.G. Beausoleil, and A.E. Willner. Higher-order-mode assisted silicon-on-insulator 90 degree polarization rotator. *Optics Express*, 17(23):20694–20699, 2009. 55, 56

[71] L. Liu, Y. Ding, K. Yvind, and J.M. Hvam. Polarization diversity circuits. *Optics Express*, 19(13):12646–12651, 2011. 56

[72] Y. Fei, L. Zhang, T. Cao, Y. Cao, and S. Chen. Ultracompact polarization splitter-rotator based on an asymmetric directional coupler. *Applied Optics*, 51(34):8257–8261, 2012. 56

[73] A. Barh, B.M.A. Rahman, R.K. Varshney, and B.P. Pal. Design and performance study of a compact soi polarization rotator at 1.55 μm. *Journal of Lightwave Technology*, 31(23):3687–3693, 2013. 56

[74] J. Wang, B. Niu, Z. Sheng, A. Wu, X. Wang, S. Zou, M. Qi, and F. Gan. Design of a sio2 top-cladding and compact polarization splitter-rotator based on a rib directional coupler. *Optics Express*, 22(4):4137–4143, 2014. 55, 56

[75] Y. Ding, H. Ou, and C. Peucheret. Wideband polarization splitter and rotator with large fabrication tolerance and simple fabrication process. *Optics Letters*, 38(8):1227–1229, 2013. 55, 57

[76] W.D. Sacher, T. Barwicz, B.J.F. Taylor, and J.K.S. Poon. Polarization rotator-splitters in standard active silicon photonics platforms. *Optics Express*, 22(4):3777–3786, 2014. 55, 57

[77] J.Z. Huang, R. Scarmozzino, G. Nagy, M.J. Steel, and R.M. Osgood Jr. Realization of a compact and single-mode optical passive polarization converter. *IEEE Photonics Technology Letters*, 12(3):317–319, 2000. 55, 58

[78] J. Yamauchi, M. Yamanoue, and H. Nakano. A short polarization converter using a triangular waveguide. *Journal of Lightwave Technology*, 26(12): 1708–1714, 2008. 58

[79] L. Jia, T.-Y. Liow, J. Song, X. Luo, N. Duan, S.C. Koh, Q. Fang, M. Yu, and G. Lo. Compact optical polarization rotators based on an asymmetric silicon waveguide. *IEEE Photonics Technology Letters*, 25(22):2229–2232, 2013. 59

[80] Y. Wakabayashi, T. Hashimoto, J. Yamauchi, and H. Nakano. Short waveguide polarization converter operating over a wide wavelength range. *Journal of Lightwave Technology*, 31(10):1544–1550, 2013. 59

[81] A.V. Velasco, M.L. Calvo, P. Cheben, A. Ortega-Moux, J.H. Schmid, C.A. Ramos, I.M. Fernandez, J. Lapointe, M. Vachon, S. Janz, and D.-X. Xu. Ultracompact polarization converter with a dual subwavelength trench built in a silicon-on-insulator waveguide. *Optics Letters*, 37(3):365–367, 2012. 59

[82] H. Fukuda, K. Yamada, T. Tsuchizawa, T. Watanabe, H. Shinojima, and S.-I. Itabashi. Polarization rotator based on silicon wire waveguides. *Optics Express*, 16(4):2628–2635, 2008. 58, 59

[83] M.R. Watts and H.A. Haus. Integrated mode-evolution-based polarization rotators. *Optics Letters*, 30(2):138–140, 2005. 58, 60

[84] L. Chen, C.R. Doerr, and Y.-K. Chen. Compact polarization rotator on silicon for polarization-diversified circuits. *Optics Letters*, 36(4):469–471, 2011. 60

[85] H. Zhang, S. Das, Y. Huang, C. Li, S. Chen, H. Zhou, M. Yu, P. Guo-Qiang Lo, and J.T.L. Thong. Efficient and broadband polarization rotator using horizontal slot waveguide for silicon photonics. *Applied Physics Letters*, 101(2), 2012. 60

[86] G. Chen, L. Chen, W. Ding, F. Sun, and R. Feng. Polarization rotators in add-drop filter systems with double-ring resonators. *IEEE Photonics Technology Letters*, 26(10):976–979, 2014. 58, 61

[87] J.N. Caspers, J.S. Aitchison, and M. Mojahedi. Experimental demonstration of an integrated hybrid plasmonic polarization rotator. *Optics Letters*, 38(20):4054–4057, 2013. 58, 62

[88] Y. Xu, J. Xiao, and X. Sun. A compact hybrid plasmonic polarization rotator for silicon-based slot waveguides. *IEEE Photonics Technology Letters*, 26(16):1609–1612, 2014. 55, 58, 62

[89] C. Peroz, A. Goltsov, S. Dhuey, P. Sasorov, B. Harteneck, I. Ivonin, S. Kopyatev, S. Cabrini, S. Babin, and V. Yankov. High-resolution spectrometer-on-chip based on digital planar holography. *IEEE Photonics Journal*, 3(5):888–896, 2011. 66, 89

[90] P. Bienstman and R. Baets. Optical modelling of photonic crystals and vcsels using eigenmode expansion and perfectly matched layers. *Optical and Quantum Electronics*, 33(4-5):327–341, 2001. 72

[91] D. Taillaert, P. Bienstman, and R. Baets. Compact efficient broadband grating coupler for silicon-on-insulator waveguides. *Optics Letters*, 29(23): 2749–2751, 2004. 75

[92] I. Giuntoni, D. Stolarek, J. Bruns, L. Zimmermann, B. Tillack, and K. Petermann. Integrated dispersion compensator based on apodized soi bragg gratings. *IEEE Photonics Technology Letters*, 25(14):1313–1316, 2013. 75

[93] Kevin Randolph Harper. *Theory, Design, and Fabrication of Diffractive Grating Coupler for Slab Waveguide*. PhD thesis, Brigham Young University, 2003. 81

[94] S.M. Spillane, T.J. Kippenberg, and K.J. Vahala. Ultralow-threshold raman laser using a spherical dielectric microcavity. *Nature*, 415(6872):621–623, 2002. 92

[95] D. Liang and J.E. Bowers. Recent progress in lasers on silicon. *Nature Photonics*, 4(8):511–517, 2010. 92, 93

[96] F. Vollmer and S. Arnold. Whispering-gallery-mode biosensing: Label-free detection down to single molecules. *Nature Methods*, 5(7):591–596, 2008. 92

[97] Lina He, Sahin Kaya Oezdemir, Jiangang Zhu, Woosung Kim, and Lan Yang. Detecting single viruses and nanoparticles using whispering gallery microlasers. *NATURE NANOTECHNOLOGY*, 6(7):428–432, JUL 2011.

[98] S. Soria, S. Berneschi, M. Brenci, F. Cosi, G.N. Conti, S. Pelli, and G.C. Righini. Optical microspherical resonators for biomedical sensing. *Sensors*, 11(1):785–805, 2011. 92

[99] M.D. Baaske, M.R. Foreman, and F. Vollmer. Single-molecule nucleic acid interactions monitored on a label-free microcavity biosensor platform. *Nature Nanotechnology*, 9(11):933–939, 2014. 92

[100] Q. Xu, D. Fattal, and R.G. Beausoleil. Silicon microring resonators with 1.5-m radius. *Optics Express*, 16(6):4309–4315, 2008. 92, 100

[101] J.E. Cunningham, I. Shubin, X. Zheng, T. Pinguet, A. Mekis, Y. Luo, H. Thacker, G. Li, J. Yao, K. Raj, and A.V. Krishnamoorthy. Highly-efficient thermally-tuned resonant optical filters. *Optics Express*, 18(18): 19055–19063, 2010. 101

[102] M. Gad, J. Ackert, D. Yevick, L. Chrostowski, and P. Jessop. Ring resonator wavelength division multiplexing interleaver. *Journal of Lightwave Technology*, 29(14):2102–2108, 2011. 92

[103] Q. Li, A.A. Eftekhar, P. Alipour, A.H. Atabaki, S. Yegnanarayanan, and A. Adibi. Low-loss microdisk-based delay lines for narrowband optical filters. *IEEE Photonics Technology Letters*, 24(15):1276–1278, 2012. 92, 101

[104] T.N. Nguyen, M. Gay, K. Lengle, L. Bramerie, M. Thual, J.C. Simon, S. Malaguti, G. Bellanca, S. Trillo, S. Combrie, G. Lehoucq, and A. De Rossi. 100-gb/s wavelength division demultiplexing using a photonic crystal four-channel drop filter. *IEEE Photonics Technology Letters*, 25(9): 813–816, 2013. 92, 94, 101, 102

[105] T. Carmon and K.J. Vahala. Visible continuous emission from a silica microphotonic device by third-harmonic generation. *Nature Physics*, 3(6): 430–435, 2007. 92

[106] A. Melloni, F. Morichetti, and M. Martinelli. Four-wave mixing and wavelength conversion in coupled-resonator optical waveguides. *Journal of the Optical Society of America B: Optical Physics*, 25(12):C87–C97, 2008. 92

[107] A.C. Turner, M.A. Foster, A.L. Gaeta, and M. Lipson. Ultra-low power parametric frequency conversion in a silicon microring resonator. *Optics Express*, 16(7):4881–4887, 2008. 93

[108] A. Pasquazi, R. Ahmad, M. Rochette, M. Lamont, B.E. Little, S.T. Chu, R. Morandotti, and D.J. Moss. All-optical wavelength conversion in an integrated ring resonator. *Optics Express*, 18(4):3858–3863, 2010. 92, 93

[109] R. Salem, M.A. Foster, A.C. Turner, D.F. Geraghty, M. Lipson, and A.L. Gaeta. Signal regeneration using low-power four-wave mixing on silicon chip. *Nature Photonics*, 2(1):35–38, 2008. 92

[110] F.Y. Gardes, A. Brimont, P. Sanchis, G. Rasigade, D. Marris-Morini, L. O'Faolain, F. Dong, J.M. Fedeli, P. Dumon, L. Vivien, T.F. Krauss, G.T. Reed, and J. Mart. High-speed modulation of a compact silicon ring resonator based on a reverse-biased pn diode. *Optics Express*, 17(24):21986–21991, 2009. 92

[111] L.D. Tzuang, M. Soltani, Y.H.D. Lee, and M. Lipson. High rf carrier frequency modulation in silicon resonators by coupling adjacent free-spectral-range modes. *Optics Letters*, 39(7):1799–1802, 2014. 92

[112] A.W. Poon, X. Luo, F. Xu, and H. Chen. Cascaded microresonator-based matrix switch for silicon on-chip optical interconnection. *Proceedings of the IEEE*, 97(7):1216–1238, 2009. 92

[113] J. Song, X. Luo, X. Tu, L. Jia, Q. Fang, T.-Y. Liow, M. Yu, and G.-Q. Lo. On-chip quasi-digital optical switch using silicon microring resonator-coupled mach-zehnder interferometer. *Optics Express*, 21(10):12767–12775, 2013. 92, 94

[114] M. Lipson. Guiding, modulating, and emitting light on silicon - challenges and opportunities. *Journal of Lightwave Technology*, 23(12):4222–4238, 2005. 93

[115] J. Van Campenhout, L. Liu, P. Rojo Romeo, D. Van Thourhout, C. Seassal, P. Regreny, L. Di Cioccio, J.-M. Fedeli, and R. Baets. A compact soi-integrated multiwavelength laser source based on cascaded inp microdisks. *IEEE Photonics Technology Letters*, 20(16):1345–1347, 2008. 93

[116] Y. Zhang, H. Wang, H. Qu, S. Zhang, and W. Zheng. Slotted hybrid iii-v/silicon single-mode laser. *IEEE Photonics Technology Letters*, 25(7): 655–658, 2013. 93

[117] H. Rong, S. Xu, Y.-H. Kuo, V. Sih, O. Cohen, O. Raday, and M. Paniccia. Low-threshold continuous-wave raman silicon laser. *Nature Photonics*, 1 (4):232–237, 2007. 93

[118] Y. Takahashi, Y. Inui, T. Asano, and S. Noda. Ultralow-threshold continuous-wave raman silicon laser using a photonic crystal high-q nanocavity. page CTh3F.1, 2013. 93

[119] Frank Vollmer and Lan Yang. Label-free detection with high-Q microcavities: a review of biosensing mechanisms for integrated devices. *NANOPHOTONICS*, 1(3-4):267–291, 2012. 93

[120] Heather K. Hunt, Carol Soteropulos, and Andrea M. Armani. Bioconjugation Strategies for Microtoroidal Optical Resonators. *SENSORS*, 10(10): 9317–9336, 2010. 93

[121] AM Armani, DK Armani, B Min, KJ Vahala, and SM Spillane. Ultra-high-Q microcavity operation in H2O and D2O. *APPLIED PHYSICS LETTERS*, 87(15), OCT 10 2005. 93

[122] GM HALE and MR QUERRY. OPTICAL-CONSTANTS OF WATER IN 200-NM TO 200-MUM WAVELENGTH REGION. *APPLIED OPTICS*, 12(3):555–563, 1973. 93

[123] Martin A. Green. Self-consistent optical parameters of intrinsic silicon at 300 K including temperature coefficients. *SOLAR ENERGY MATERIALS AND SOLAR CELLS*, 92(11):1305–1310, 2008. 93

[124] D.J. Moss, R. Morandotti, A.L. Gaeta, and M. Lipson. New cmos-compatible platforms based on silicon nitride and hydex for nonlinear optics. *Nature Photonics*, 7(8):597–607, 2013. 93

[125] G.T. Reed, G. Mashanovich, F.Y. Gardes, and D.J. Thomson. Silicon optical modulators. *Nature Photonics*, 4(8):518–526, 2010. 94

[126] X. Xiao, X. Li, H. Xu, Y. Hu, K. Xiong, Z. Li, T. Chu, J. Yu, and Y. Yu. 44-gb/s silicon microring modulators based on zigzag pn junctions. *IEEE Photonics Technology Letters*, 24(19):1712–1714, 2012. 94

[127] D.J. Thomson, F.Y. Gardes, J.-M. Fedeli, S. Zlatanovic, Y. Hu, B.P.P. Kuo, E. Myslivets, N. Alic, S. Radic, G.Z. Mashanovich, and G.T. Reed. 50-gb/s silicon optical modulator. *IEEE Photonics Technology Letters*, 24 (4):234–236, 2012. 94

[128] B. Milivojevic, S. Wiese, C. Raabe, A. Shastri, M. Webster, P. Metz, B. Chattin, B. Dama, and K. Shastri. Small-size silicon photonic iq modulator and low-power cmos driver for next generation coherent transceivers. In *Network and Optical Communications (NOC), 2013 18th European Conference on and Optical Cabling and Infrastructure (OC i), 2013 8th Conference on*, pages 181–184, July 2013. 94

[129] D. Po, S.F. Preble, and M. Lipson. All-optical compact silicon comb switch. *Optics Express*, 15(15):9600–9605, 2007. 94

[130] Po Dong, Shirong Liao, Hong Liang, Roshanak Shafiiha, Dazeng Feng, Guoliang Li, Xuezhe Zheng, Ashok Krishnamoorthy, and Mehdi Asghari. High-speed and broadband electro-optic silicon switch with submilliwatt switching power. page OWZ4, 2011. 94

[131] K. Okamoto. Wavelength-division-multiplexing devices in thin soi: Advances and prospects. *IEEE Journal on Selected Topics in Quantum Electronics*, 20(4), 2014. 94, 96, 97, 98, 100

[132] Kazumasa Takada, M. Abe, T. Shibata, and Katsunari Okamoto. 1-ghz-spaced 16-channel arrayed-waveguide grating for a wavelength reference standard in dwdm network systems. *J. Lightwave Technol.*, 20(5):822, May 2002. 96

[133] Y Hida, Y Hibino, M Itoh, A Sugita, A Himeno, and Y Ohmori. Fabrication of low-loss and polarisation-insensitive 256 channel arrayed-waveguide grating with 25 GHz spacing using 1.5% Delta waveguides. *ELECTRONICS LETTERS*, 36(9):820–821, APR 27 2000. 96, 97

[134] Y Hibino. Recent advances in high-density and large-scale AWG multi/demultiplexers with higher index-contrast silica-based PLCs. *IEEE JOURNAL OF SELECTED TOPICS IN QUANTUM ELECTRONICS*, 8 (6):1090–1101, NOV-DEC 2002. 97

[135] T Goh, S Suzuki, and A Sugita. Estimation of waveguide phase error in silica-based waveguides. *JOURNAL OF LIGHTWAVE TECHNOLOGY*, 15(11):2107–2113, NOV 1997. 97, 98

[136] Y. Barbarin, X.J.M. Leijtens, E.A.J.M. Bente, C.M. Louzao, J.R. Kooiman, and M.K. Smit. Extremely small awg demultiplexer fabricated on inp by using a double-etch process. *IEEE Photonics Technology Letters*, 16(11): 2478–2480, 2004. 97

[137] S. Pathak, M. Vanslembrouck, P. Dumon, D. Van Thourhout, and W. Bogaerts. Optimized silicon awg with flattened spectral response using an mmi aperture. *Journal of Lightwave Technology*, 31(1):87–93, 2013. 98

[138] D. Dai, X. Fu, Y. Shi, and S. He. Experimental demonstration of an ultracompact si-nanowire-based reflective arrayed-waveguide grating (de)multiplexer with photonic crystal reflectors. *Optics Letters*, 35(15): 2594–2596, 2010. 98

[139] F. Horst, W.M.J. Green, B.J. Offrein, and Y.A. Vlasov. Silicon-on-insulator echelle grating wdm demultiplexers with two stigmatic points. *IEEE Photonics Technology Letters*, 21(23):1743–1745, 2009. 99

[140] R.J. Lycett, D.F.G. Gallagher, and V.J. Brulis. Perfect chirped echelle grating wavelength multiplexor: Design and optimization. *IEEE Photonics Journal*, 5(2), 2013. 99

[141] B.J. Luff, V. Tsatourian, P.A.L. Stopford, S.W. Roberts, J.P. Drake, S.A. Fuller, and M. Asghari. Planar reflection grating wavelength filters in silicon. *Journal of Lightwave Technology*, 21(12):3387–3391, 2003. 99, 125

[142] W. Bogaerts, S.K. Selvaraja, P. Dumon, J. Brouckaert, K. De Vos, D. Van Thourhout, and R. Baets. Silicon-on-insulator spectral filters fabricated with cmos technology. *IEEE Journal on Selected Topics in Quantum Electronics*, 16(1):33–44, 2010. 99

[143] S Kamei, M Oguma, M Kohtoku, T Shibata, and Y Inoue. Low-loss athermal silica-based lattice-form interleave filter with silicone-filled grooves. *IEEE PHOTONICS TECHNOLOGY LETTERS*, 17(4):798–800, 2005. 99

[144] F. Horst, W.M.J. Green, S. Assefa, S.M. Shank, Y.A. Vlasov, and B.J. Offrein. Cascaded mach-zehnder wavelength filters in silicon photonics for low loss and flat pass-band wdm (de-)multiplexing. *Optics Express*, 21(10): 11652–11658, 2013. 99

[145] A. Morand, Y. Zhang, B. Martin, K.P. Huy, D. Amans, P. Benech, J. Verbert, E. Hadji, and J.-M. Fdli. Ultra-compact microdisk resonator filters on soi substrate. *Optics Express*, 14(26):12814–12821, 2006. 100, 101, 102

[146] S. Fan and J.D. Joannopoulos. Analysis of guided resonances in photonic crystal slabs. *Physical Review B - Condensed Matter and Materials Physics*, 65(23):2351121–2351128, 2002. 100, 102

[147] A. D'Orazio, M. De Sario, V. Marrocco, V. Petruzzelli, and F. Prudenzano. Photonic crystal drop filter exploiting resonant cavity configuration. *Nanotechnology, IEEE Transactions on*, 7(1):10–13, Jan 2008. 100, 101, 102

[148] M.A. Popovi, T. Barwicz, M.R. Watts, P.T. Rakich, L. Socci, E.P. Ippen, F.X. Krtner, and H.I. Smith. Multistage high-order microring-resonator add-drop filters. *Optics Letters*, 31(17):2571–2573, 2006. 100, 103

[149] E. A. J. Marcatili. Bends in optical dielectric guides. *The Bell System Technical Journal*, 48:2103–2132, 1969. 100

[150] B.E. Little, J.S. Foresi, G. Steinmeyer, E.R. Thoen, S.T. Chu, H.A. Haus, E.P. Ippen, L.C. Kimerling, and W. Greene. Ultra-compact si-sio2 microring resonator optical channel dropping filters. *IEEE Photonics Technology Letters*, 10(4):549–551, 1998. 100

[151] Dominik G. Rabus. *Integrated Ring Resonators: The Compendium*. Springer, New York, 2007. 100, 110, 111, 120, 123

[152] P. Dumon, W. Bogaerts, V. Wiaux, J. Wouters, S. Beckx, J. Van Campenhout, D. Taillaert, B. Luyssaert, P. Bienstman, D. Van Thourhout, and R. Baets. Low-loss soi photonic wires and ring resonators fabricated with deep uv lithography. *IEEE Photonics Technology Letters*, 16(5):1328–1330, 2004. 100, 114

[153] S.T. Chu, B.E. Little, W. Pan, T. Kaneko, S. Sato, and Y. Kokubun. Eight-channel add-drop filter using vertically coupled microring resonators over a cross grid. *IEEE Photonics Technology Letters*, 11(6):691–693, 1999. 100, 101

[154] M. Soltani, S. Yegnanarayanan, and A. Adibi. Ultra-high q planar silicon microdisk resonators for chip-scale silicon photonics. *Optics Express*, 15(8): 4694–4704, 2007. 101

[155] E. Yablonovitch. Inhibited spontaneous emission in solid-state physics and electronics. *Physical Review Letters*, 58(20):2059–2062, 1987. 101

[156] L.H. Frandsen, A.V. Lavrinenko, J. Fage-Pedersen, and P.I. Borel. Photonic crystal waveguides with semi-slow light and tailored dispersion properties. *Optics Express*, 14(20):9444–9450, 2006. 101

[157] C. Monat, C. Seassal, X. Letartre, P. Viktorovitch, P. Regreny, M. Gendry, P. Rojo-Romeo, G. Hollinger, E. Jalaguier, S. Pocas, and B. Aspar. Inp 2d photonic crystal microlasers on silicon wafer: Room temperature operation at 1.55 m. *Electronics Letters*, 37(12):764–766, 2001. 101

[158] B.-S. Song, S. Noda, T. Asano, and Y. Akahane. Ultra-high-q photonic double-heterostructure nanocavity. *Nature Materials*, 4(3):207–210, 2005. 102

[159] L. Li and G.Q. Liu. Photonic crystal ring resonator channel drop filter. *Optik*, 124(17):2966–2968, 2013. 102

[160] H. Tian, G. Shen, W. Liu, and Y. Ji. Integration of both dense wavelength-division multiplexing and coarse wavelength-division multiplexing demultiplexer on one photonic crystal chip. *Optical Engineering*, 52(7), 2013. 102

[161] M. Kanskar, P. Paddon, V. Pacradouni, R. Morin, A. Busch, J.F. Young, S.R. Johnson, J. MacKenzie, and T. Tiedje. Observation of leaky slab modes in an air-bridged semiconductor waveguide with a two-dimensional photonic lattice. *Applied Physics Letters*, 70(11):1438–1440, 1997. 102

[162] B.E. Little, S.T. Chu, H.A. Haus, J. Foresi, and J.-P. Laine. Microring resonator channel dropping filters. *Lightwave Technology, Journal of*, 15 (6):998–1005, Jun 1997. 102, 103

[163] B.E. Little, S.T. Chu, and H.A. Haus. Micro-ring resonator channel dropping filters. volume 2, pages 233–234, 1995. 103

[164] A. Yariv, Y. Xu, R.K. Lee, and A. Scherer. Coupled-resonator optical waveguide: A proposal and analysis. *Optics Letters*, 24(11):711–713, 1999. 103

[165] D. Park, S. Kim, I. Park, and H. Lim. Higher order optical resonant filters based on coupled defect resonators in photonic crystals. *Journal of Lightwave Technology*, 23(5):1923–1928, 2005. 103

[166] Z. Dai, J. Wang, and Y. Heng. Circuit-based method for synthesizing of coupled-resonators bandpass photonic crystal filters. *Optics Express*, 19(4): 3667–3676, 2011.

[167] H. Ren, J. Zhang, Y. Qin, J. Li, S. Guo, W. Hu, C. Jiang, and Y. Jin. Photonic crystal higher order three-port channel drop filter. *Optik*, 124 (14):1787–1791, 2013.

[168] S. Feng, Y. Wang, and W. Wang. Slow light propagating characteristics through a two-dimensional silicon-based coupled-resonator optical waveguide. *Optik*, 124(4):331–334, 2013. 103

[169] F. Xia, L. Sekaric, M. O'Boyle, and Y. Vlasov. Coupled resonator optical waveguides based on silicon-on-insulator photonic wires. *Applied Physics Letters*, 89(4), 2006. 103

[170] F. Xia, M. Rooks, L. Sekaric, and Y. Vlasov. Ultra-compact high order ring resonator filters using submicron silicon photonic wires for on-chip optical interconnects. *Optics Express*, 15(19):11934–11941, 2007. 103

[171] T. Barwicz, M.A. Popovi, M.R. Watts, P.T. Rakich, E.P. Ippen, and H.I. Smith. Fabrication of add-drop filters based on frequency-matched microring resonators. *Journal of Lightwave Technology*, 24(5):2207–2218, 2006. 103

[172] M.L. Cooper, G. Gupta, M.A. Schneider, W.M.J. Green, S. Assefa, F. Xia, Y.A. Vlasov, and S. Mookherjea. Statistics of light transport in 235-ring silicon coupled-resonator optical waveguides. *Optics Express*, 18(25):26505–26516, 2010. 103

[173] A. Melloni. Synthesis of a parallel-coupled ring-resonator filter. *Optics Letters*, 26(12):917–919, 2001. 103, 116, 130, 131, 132, 133, 158, 159, 163

[174] A. Canciamilla, M. Torregiani, C. Ferrari, F. Morichetti, R.M. De La Rue, A. Samarelli, M. Sorel, and A. Melloni. Silicon coupled-ring resonator structures for slow light applications: Potential, impairments and ultimate limits. *Journal of Optics*, 12(10), 2010. 103

[175] A Melloni, C. Ferrari, A Canciamilla, F. Morichetti, and M. Sorel. Potential and limitations of photonic integrated filters. In *Information Photonics (IP), 2011 ICO International Conference on*, pages 1–2, May 2011. 104

[176] F. Morichetti, A. Canciamilla, M. Martinelli, A. Samarelli, R.M. De La Rue, M. Sorel, and A. Melloni. Coherent backscattering in optical microring resonators. *Applied Physics Letters*, 96(8), 2010. 104

[177] David M. Pozar. *Microwave Engineering, Chapter 8: Microwave Filters*, pages 389–405. John Wiley and Sons, New Jersey, 2005. 115, 116, 119, 130, 131, 132, 133, 138, 158, 159

[178] G. L. Matthaei, L. Young, and E. M. T. Jones. *Microwave Filters, Impedance-Matching Networks, and Couping Structures*. Artech House, Dedham, Massachusetts, 1980. 131, 159

[179] S.-Y. Cho and R. Soref. Apodized scissors for filtering and switching. *Optics Express*, 16(23):19078–19090, 2008. 158